UNIVERSITY OF ZURICH (UZH)

Thin Planar Silicon Pixel Sensors for the CMS Phase-2 Upgrade - Study of the Effects of Irradiation and Annealing

by

Daniel Hernandez Garland

A thesis submitted in partial fulfilment for the
Master of Science (M. Sc.)

in the
Faculty of Science
Physics Institute

Supervising professor: Prof. Dr. Ben Kilminster
Direct supervisor: Dr. Anna Macchiolo

Zurich, April 2022

d.hernandez@pucp.edu.pe
daniel.hernandezgarland@uzh.ch

"Trees grow from air."

-Richard Feynman

UNIVERSITY OF ZURICH (UZH)

Abstract

Faculty of Science
Physics Institute

Master of Science

by Daniel Hernandez Garland

The pursuit of knowledge and understanding give us an always curious and ambitious nature. Improvements in theories and technology allow us to push the limits of our understanding a little further every time. In this regard, one of the main goals of particle physics is to reveal the underlying nature of our universe and understand it as much as we can. The aim of this work, which follows the same line of thought, focuses on studying the behaviour of devices that play a crucial role in particle detectors, silicon pixel sensors, namely.

Hereby, I continue with what is to be shared.

Acknowledgements

I would like to thank the head of the research group, Prof. Dr. Ben Kilminster, my direct supervisor, Dr. Anna Macchiolo, and also Dr. Riccardo Del Burgo, for his support and for his ingenious solutions during the laboratory days.

Clearly, I would have not reached alone to where I am now. Many people have helped me in diverse forms along the way, which I appreciate and value most highly. Like my family, Gonzalo, Guayo, Mago, Max, and my girlfriend, Marie, for their really unconditional help and for being with me day to day. My good office mates and friends. And as well, Ms. Regina Schmid, from the Physics Institute, who's small conversations arrived always at the right moment.

Table of Contents

List of Figures

List of Tables

Abbreviations

ALICE	A Large Ion Collider Experiment
ASICs	Application-Specific Integrated Circuits
ATLAS	A Toroidal LHC Apparatus
BCB	Benzocyclobutene
BPix	Barrel Pixel Detector
BR	Bias Ring
CERN	Conseil Européen Pour la Recherche Nucléaire
CMOS	Complementary Metal–Oxide–Semiconductor
CMS	Compact Muon Solenoid
CPU	Central Processing Unit
CSCs	Cathode Strip Chambers
DAQ	Data Acquisition
DC	Direct Current
DTs	Drift Tubes
DUT	Device(s) Under Test
ECAL	Electronic Calorimeter
EMI	Electromagnetic Interference
FDB	Si-Si Direct Bonded
FDD	Deep-Diffused
FPGA	Field-Programmable Gate Array
FPix	Forward Pixel Detector
FTH	Physically Thinned
GaAs	Gallium Arsenide
Ge	Germanium
HB	Hadronic Calorimeter Barrel

HCAL	Hadron Calorimeter
HDI	High-Definiton Interconect
HE	Hadronic Calorimeter End-Caps
HEP	High Energy Physics
HF	Hadronic Calorimeter Forward
HL-LHC	High Luminosity HLC
HLT	High Level Trigger
HO	Hadronic Calorimeter Outer
HPK	Hamamatsu Photonics K.K.
IT	Inner Tracker (Phase 2)
JSI	Jožef Stefan Institute
L1T	Level 1 Trigger
LHC	Large Hadron Collider
LHCb	LHC Beauty
LINAC2	Linear Accelerator 2
NIEL	Non Ionizing Energy Loss
NMOS	N-type Metal-Oxide-Semiconductor
OS	Operating System
OT	Outer Tracker
PCB	Printed Circuit Board
PMOS	P-channel Metal-Oxide-Semiconductor
PS	Proton Booster
PSB	Proton Synchroton Booster
QCD	Quantum Chromodynamics
R&D	Research & Development
ROC	Read Out Chip
RPCs	Resistive Place Chambers
SCR	Space Charge Region
SCSI	Space Charge Sign Inversion
SEEs	Single Event Effects
Si	Silicon
SiO_2	Silicon Dioxide
SMU	Sensor Measure Unit

SPS	Super Proton Synchroton
SRH	Shockley–Read–Hall
TBPX	Tracker Barrel Pixel
TEC	Tracker End-Caps
TEPX	Tracker Extension Pixel
TFPX	Tracker Forward Piel
TIB	Tracker Inner Barrel Detector
TID	Tracker Inner Disk Detector
TID	Tracker Inner Disk
TID	Total Ionising Dose
TOB	Tracker Outer Barrel Detector
UZH	Universität Zürich
WLCG	Worldwide LHC Computing Grid

Physical Constants

Speed of Light	c	=	$2.997\ 924\ 58 \times 10^{8}$ ms^{-1}	(exact)
Electron Volt	eV	=	$1.602\ 176\ 634 \times 10^{-19}$ J	(exact)
Boltsman Constant	k_B	=	$1.380\ 649 \times 10^{-23}$ JK^{-1}	(exact)
Avogadro's Number	N_0	=	$6.022\ 140\ 76 \times 10^{23}$	(exact)
Elementary Charge	q_e	=	$1.602\ 176\ 634 \times 10^{-19}C$	(exact)
Electron Mass	m_e	=	$9.109\ 383\ 701(28) \times 10^{-31}kg$	
Classical Electron Radius	r_e	=	$2.817\ 940\ 322(19) \times 10^{-15}$m	

Angstrong	Å	=	10^{-10} m
Barn	b	=	10^{-28} m^2
Rad	rad	=	10^{-2} Gy

Derived Units

Pa	pressure (pascal)	kg $m^{-1}s^{-2}$
$^{\circ}C$	temperature (degree Celsius)	$(^{\circ}C + 273.15)K$
T	magnetic flux density (tesla)	kg $s^{-2}A^{-1}$
Gy	ionizing radiation dose (gray)	Gy(m^2 s^{-2})
P	power	W (Js^{-1})
ω	angular frequency	$rads^{-1}$
$\mathcal{L}$	instantaneous luminosity	$cm^{-2}s^{-1}$
Φ_{eq}	$1MeV$ neutron equivalent fluence	n_{eq} cm^{-2}
σ	electric conductance	S($kg^{-1}m^{-2}s^3A^2$)
ε	electric field	m kg $s^{-3}A^{-1}$
η	pseudorapidity	$= -\log\left(\frac{\tan\theta}{2}\right)$

Chapter 1

Introduction

One way of studying the underlying phenomena embedded in the quantum world, is to reveal it by creating the adequate conditions.

In a highly energetic collision between two protons, for example, elusive short-lived particles can emerge and interact with others during short periods of time, after which they will cease to exist, or at least for our detection methods. From another point of view, these short-lived particles are a manifestation of excited states of fundamental fields, which in the event of the collision, gained localised energy in a short period of time.

The Large Hadron Collider (LHC) is a machine built for such purpose, and it studies a wide range of phenomena, starting with the Standard Model including the Higgs boson (e.g. Figure 1.1), and what lies beyond, as super-symmetry and candidates for dark matter.

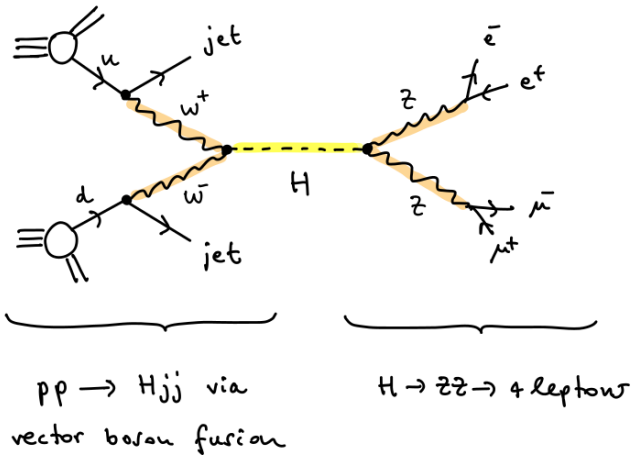

FIGURE 1.1: Higgs boson production at the LHC via vector boson fusion, and decay via the 4 lepton channel [1]. (Go back to The muon system)

For the previous, the collisions between protons happen inside detectors that measure the particles emerging from the collisions. One of such detectors is the Compact Muon Solenoid (CMS), and it can reconstruct the trajectories of the particles as they travel through its tracking system. The tracking system, or tracker, is entirely built up with silicon sensors and it is the innermost system of the CMS. It contains the Pixel Tracker and the Strip Tracker. The former, being the closest to the beam pipe, is made by 65 million silicon (Si) pixel sensors, as it name suggests. And due to its distance from the collisions, it receives the highest radiation doses in all the detector.

With the intention of increasing the discovery capacities, the LHC will undergo a major upgrade in the following years, the High Luminosity LHC (HL-LHC), and will operate at a maximum centre-of-mass energy of $14TeV$ and with an increased instantaneous peak luminosity up to 7 times the design value of $10^{34}cm^2s^{-1}$, which corresponds to approximately 200 inelastic proton-proton collisions per beam crossing.

For CMS, one of the main challenges posed by the high luminosity upgrade will be to withstand the much larger amount of radiation that will be produced, especially in the Pixel Tracker, which will need to be replaced. Given the previous, silicon pixel sensors will require new technologies and a careful design to fulfil their duty duly.

For that reason, the aim of this thesis is to test the required sensor technology to instrument the CMS pixel detector of the new Tracker. For the previous, thin planar silicon sensors have been electrically characterised after being irradiated with neutrons, in order to investigate the effects of radiation damage on the operational parameters of the devices.

The results of the studies performed have been used as direct reference for the decision of the technology of the sensors to be installed in the the CMS Pixel detector for the HL-LHC.

About a bird's-eye perspective of this work;

In chapter 1, where we are, a brief motivation behind particle physics is presented. As well, a short introduction to the CMS, the LHC, and their upgrades are given, which in turn, explains the reason behind the research conducted for this thesis.

In chapter 2, the LHC will be described including the main detectors, its basic working principles, subsystems, and as well, its upcoming upgrade, the HL-LHC.

In chapter 3, the CMS experiment will be described, similarly as before, including its basic working principles and subsystems, but with emphasis on the Inner Tracker (IT) and the pixel modules.

Chapter 4 is dedicated to the Phase 2 upgrade of the CMS, which is a preparation for the High Luminosity era. The discussion here will turn towards the tracker; limitations of the current tracker and requirements for the upgraded tracker will be presented. The silicon pixel sensors that will equip the IT will be described as well.

Chapter 5 will serve as a walk-through of the physics behind particle detectors and radiation damage. The theoretical framework will cover semiconductor physics, semiconductor devices, and will give an overview of radiation induced effects, as it boils down to the effects of radiation damage on the operational parameters of silicon pixel sensors.

With the introduction and the framework already set;

Chapter 6 will present the experimental work and the results in a detailed manner. A precise description of the sensors and the measurements performed will be given, and the data will be plotted and shown in graphs.

Finally, in chapter 7, the results and conclusions obtained will be commented.

Chapter 2

Large Hadron Collider

Since its start on the 10th of September of 2008 when the first beam successfully run a round trip [34], and until present day, the Large Hadron Collider (LHC) [35] is the most powerful particle accelerator ever built and the newest addition to the CERN [36] (Conseil Européene pour la Recherche Nucléaire) accelerator complex.

The LHC is located in an underground tunnel, at an average depth of $100m$, at the border between Switzerland and France, as shown in Figure 2.1.

The LHC accelerates two proton beams in opposite directions employing superconducting magnets cooled up to -271.3°C. They travel in groups (bunches) through pipelines which are kept at ultrahigh vacuum pressures ranging between 10^{-7} and $10^{-9}Pa$ [37]. Protons reach speeds of up to 99.9999% the speed of light, c, and will eventually engage in proton-proton (pp) collisions leaving a plethora of different particles as collision debris.

The protons are obtained by stripping off electrons out of hydrogen atoms kept in a small hydrogen bottle, shown in Figure 2.2. Then, they are first fed into a chain of pre-accelerators of increasing energy, which will finally lead to the injection into the LHC ring. The pre-accelerators reach the following energies: Linear Accelerator 2 (LINAC2) up to 50 MeV, Proton Synchrotron Booster (PSB) up to 1.4 GeV, Proton Synchrotron (PS) up to 25 GeV, Super Proton Synchrotron (SPS) up to 450 GeV [38]. The pre-accelerator chain scheme is shown in Figure 2.3.

More information can be found in [39].

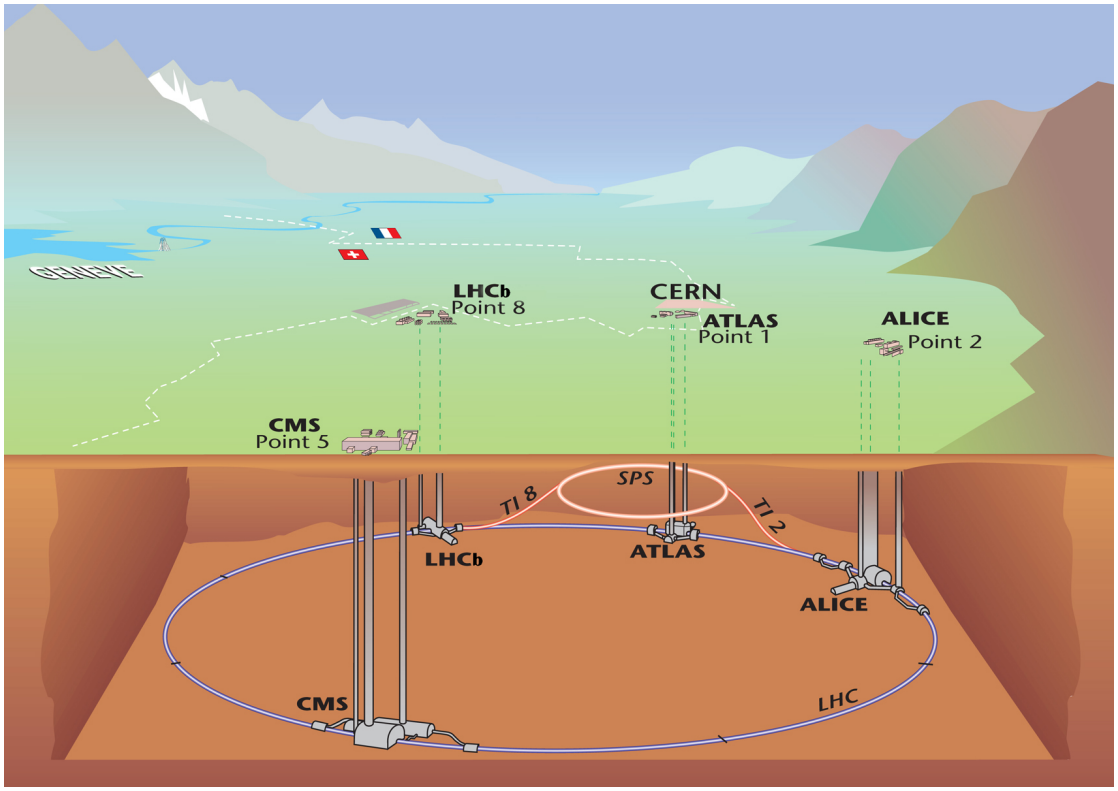

FIGURE 2.1: The CERN accelerator complex is shown below the Swiss-French border [2]. (Go back to Large Hadron Collider)

FIGURE 2.2: Hydrogen bottle used to feed protons to Linac2 accelerator. Where it all starts [3]. (Go back to Large Hadron Collider)

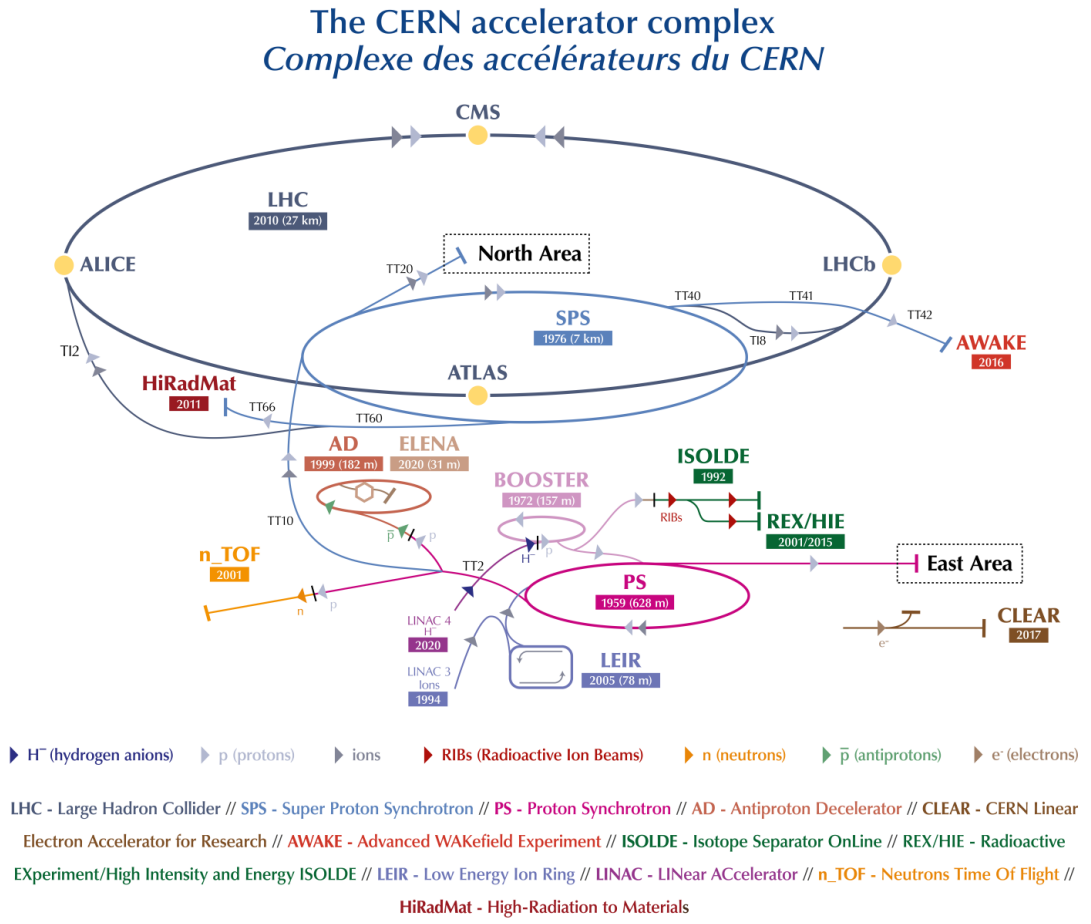

FIGURE 2.3: The CERN accelerator complex is shown including all the experiments and pre-accelerators [4]. (Go back to Large Hadron Collider)

2.1 Proton-proton collisions

The performance of particle colliders is usually quantified by the particle beam energy and the luminosity ($\mathcal{L}$). The luminosity depends on the beam parameters and can be defined as the ratio of the number of events (pp collisions in this case) in a certain period of time, to the event's cross-section. The number of events generated per unit of time is given by:

$$\frac{dN_{events}}{dt} = \sigma_{events} \cdot \mathcal{L}, \tag{2.1}$$

where N_{events} is the number of events, σ_{events} is the event's cross-section, and $\mathcal{L}$ is the instantaneous luminosity of the collider, measured in number of events per unit of time per unit of area, $cm^{-2}s^{-1}$.

Assuming Gaussian distributions for the beams and assuming them to be equal, which is often justified, we can express the instantaneous luminosity of two beams colliding head-on as [40]:

$$\mathcal{L} = \frac{N_1 N_2 f N_b}{\pi \sigma_x \sigma_y}, \tag{2.2}$$

where N_1 and N_2 are the number of particles per bunch, f is the revolution frequency, N_b is the number of bunches, and σ_x and σ_y parametrize the beam spread across the x and y axis, respectively.

In a simplistic way, we can think of Luminosity as the amount of data that a collider is capable of generating.

2.2 Main detectors

The beams travelling inside the LHC are accelerated, bent and focused by means of specific magnet arrays, which as well squeeze them moments before they are made to collide. These collisions happen in 4 specific Interaction Points (IPs) along the ring, corresponding to the locations of the four big particle detectors: ATLAS, CMS, ALICE, LHCb, as shown in Figure 2.4.

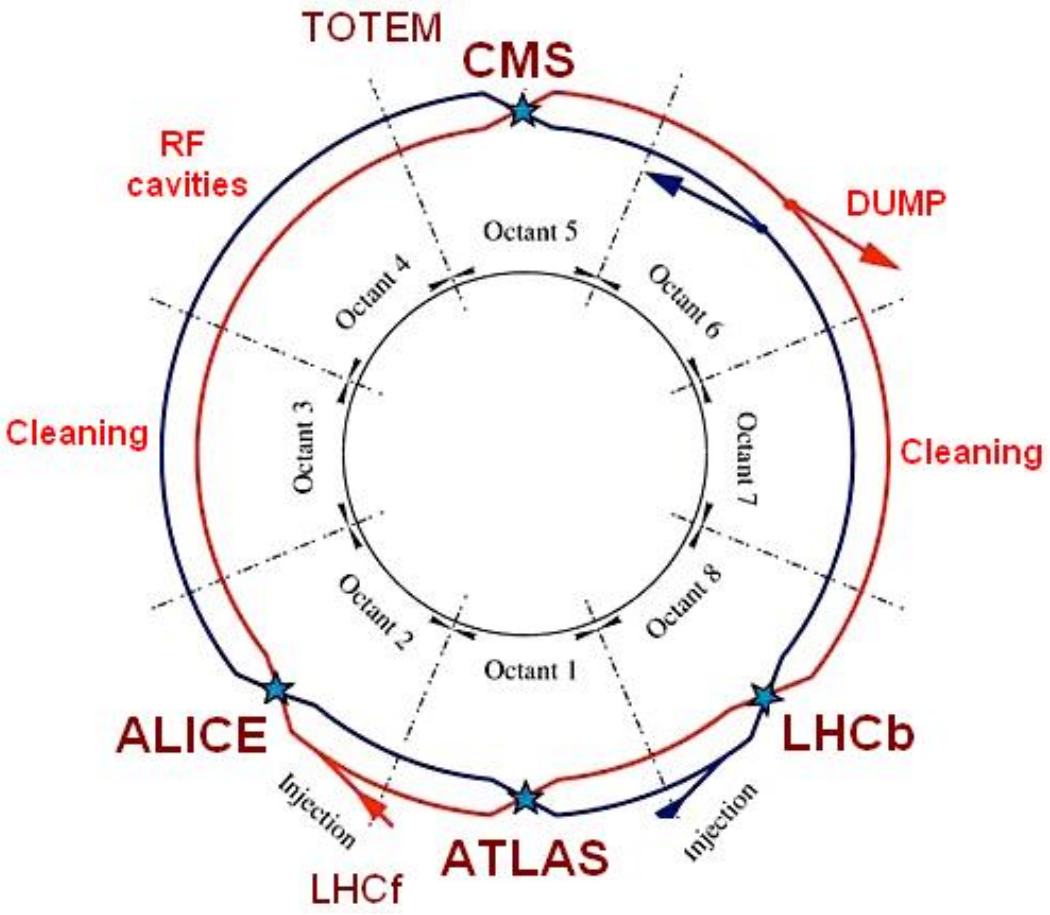

FIGURE 2.4: A diagram of the LHC ring is shown. Pipelines are shown with red and blue lines starting with the injection points. The IPs are marked with blue stars at the locations of the main experiments: ATLAS, CMS, ALICE, and LHCb [5]. (Go back to Main detectors)

2.2.1 Atlas

Atlas (A Toroidal LHC Apparatus) is one of the two general-purpose detectors and the largest of the 4 experiments. It has a cylindrical shape and it is $46m$ long, $25m$ in diameter and weights 7000 tonnes. In July of 2012, and in conjunction with CMS, Atlas announced the discovery of the Higgs boson [41]. A schematic view of the ATLAS detector can be seen in Figure 2.5.

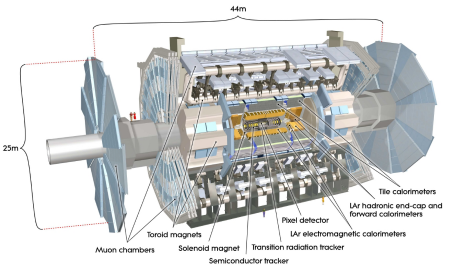

FIGURE 2.5: ATLAS detector [6].

2.2.2 CMS

CMS (Compact Muon Solenoid) is a general-purpose detector built around a solenoidal superconducting magnet delivering a 4 T magnetic field and weighting around 12000 tonnes, which gives its name. CMS is 21 meters long, 15 meters wide and 15 meters high [42]. A schematic view of the CMS detector can be seen in Figure 2.6.

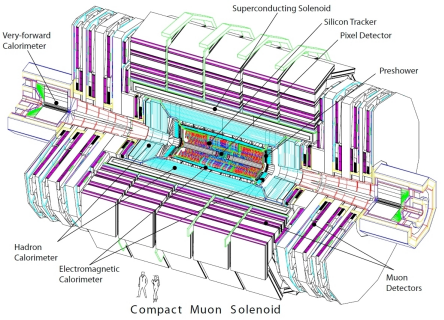

FIGURE 2.6: CMS detector [7].

2.2.3 Alice

Alice (A Large Ion Collider Experiment) is dedicated to collisions of heavy ions, allowing the study of quark-gluon plasma, which is of particular interest for Quantum Chromo Dynamics (QCD) research [43]. A

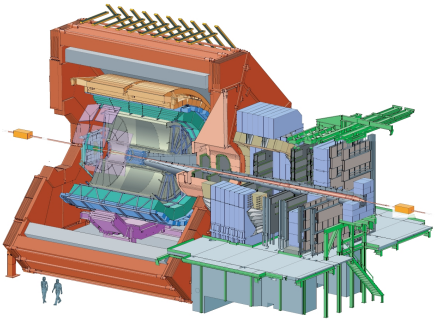

FIGURE 2.7: ALICE detector [8].

schematic view of the ALICE detector can be seen in Figure 2.7.

[aa]

2.2.4 LHCb

LHCb (LHC-beauty) is specialized in studying matter/antimatter unbalance in b quarks [44]. A schematic view of the LHCb detector can be seen in Figure 2.8.

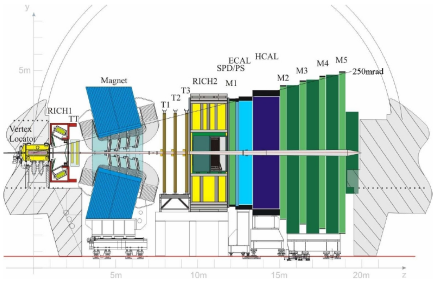

FIGURE 2.8: LHCb detector [9].

2.3 HL-LHC

The High Luminosity upgrade for Large Hadron Collider will give a formidable performance boost allowing to achieve an instantaneous luminosity seven times higher than the design value. This will have a direct impact on the discovery capacity of the collider and will allow experiments to increase their data sample by an order of magnitude. On the other hand, experiments will have to cope with the challenges of the increased luminosity, like higher levels of radiation, greater data bandwidth, and increased pile-up number. Hence, upgrades are forthcoming [45], [46].

2.3.1 Programme

The HL-LHC is expected to start operations around 2028-2029. This upgrade is part of a large ongoing programme composed by periods of data taking, referred to as Run 1, Run 2, etc. interleaved with long shutdown periods, referred to as LS1, LS2, etc. The programme schedule can be seen in Figure 2.9 and is briefly outlined below.

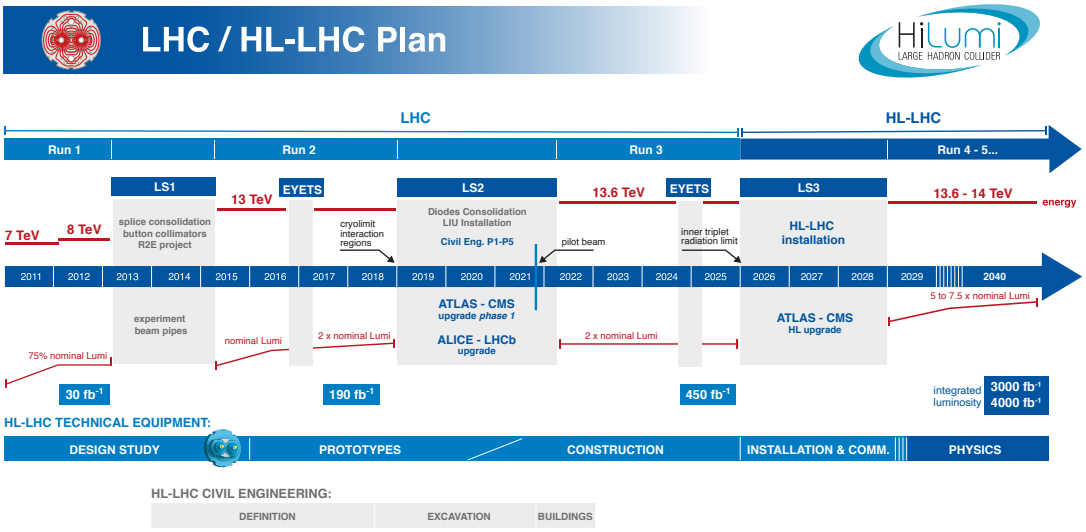

FIGURE 2.9: The LHC and HL-LHC programme [10]. (Go back to Programme)

- Run 1 (2009–2013)

  Run 1 was the first operational run, it started on November 2009 and achieved a center-of-mass energy of 1.18 TeV per beam. On March 2010, a combined energy of 7 TeV was achieved, leading to the start of the main research programme. Energy was increased to a combined energy of 8 TeV for the 2012 Run.

- LS1 (2013–2015)

  The two year upgrade Started on February 2013. The objective was to be able to deliver collisions at 14 TeV. Detectors and pre-accelerators (PS and SPS) were enhanced.

- Run 2 (2015–2018)

  The LHC restarted on April 2015, delivering up to 6.5 TeV per beam and with 13 TeV total. In June 2016, the collider instantaneous luminosity reached for first time the design value of $10^{34}\text{cm}^{-2}\text{s}^{-1}$ [47]. Luminosity was further increased in 2017 reaching twice the design value. The total number of collisions was also heighten, doubling the number obtained in 2016.

- LS2 (2018–2021)

  Long Shutdown 2 started on December 2018. The LHC and the rest of CERN's accelerator complex received a substantial upgrade in order to proceed with the HL-LHC project schedule.

- Run 3 (2022-2025)

  Run 3 is scheduled to start in the Spring of 2022 and will run until the end of 2025 with a combined center-off-mass energy of 14 TeV. Integrated luminosity during Run 3 is expected to double the one reached during Run 2.

- LS3 (2026-2028)

  Long Shutdown 3 is scheduled for 2024 until th end of 2028. All upgrades for the HL-LHC and for the experiments are planned to be finished during this phase.

- Run 4 (2029+)

  HL-LHC era will start with Run 4 at the end of 2029.

2.3.2 Luminosity and upgrades

To reduce the statistical uncertainty of measurements by half with the actual LHC configuration and luminosity, it would have taken 10 years starting from 2020. On the other hand, the HL-LHC will reach a peak luminosity of more than $7 \cdot 10^{34}$ $\text{cm}^{-2}\text{s}^{-1}$. This will allow to reach the goal of an integrated luminosity of $250 fb^{-1}$ per year and $3000 fb^{-1}$ in 10-11 years after the upgrade, which will be around ten times the integrated luminosity of the first 12 years of operation of the LHC. Furthermore, in the *ultimate luminosity scenario*, the HL-LHC should be able to reach an Integrated luminosity of $4000 fb^{-1}$ by the end of the HL-LHC programme.

For this, the new HL-LHC configuration will count with key technological upgrades to reach the intended goals, like new $11 - 12$ T superconducting magnets, compact superconducting crab cavities with ultra-precise phase control, new beam collimation system, and high-power superconducting links with negligible energy dissipation [46], [45]. Consequently, detectors will also have to upgrade their systems. CMS upgrade will be discussed in CMS Phase-2 Upgrade.

Some of the most important upgrades of the LHC systems are listed below [48]:

- Powerful focusing magnets

  New, more powerful superconducting quadrupole magnets will be installed in the insertion regions on either side of the ATLAS and CMS experiments to focus the particle bunches before they collide. The new magnets are made of niobium-tin and perform better than the previous ones, reaching a magnetic field intensity of 12 T instead of 8.

- Crab cavities for tilting the beams

  Inside Crab cavities, beams will be tilted such that they acquire a transverse momentum before meeting each other. This will increase the overlap area of the bunches, and thus, increasing the probability of collision. A total of sixteen crab cavities will be installed on either side of each of the ATLAS and CMS experiments.

- Reinforced machine protection

  As there will be more particles contained in the beams, more and new collimators must be installed along the ring. Collimators absorb particles that stray from the beam trajectory which could otherwise damage the machine.

- More compact and powerful bending magnets

  New niobium-tin superconducting dipole magnets will be installed. They will generate an 11 T magnetic field, compared the actual 8.3 T dipole magnets.

- Innovative superconducting links

  Superconducting power lines will connect the power converters to the accelerator. These cables, made of magnesium diboride, will be able to carry currents of up to 10^5A.

- Upgraded pre-accelerator chain

  As the HL-LHC's performance also relies heavily on the injector chain, it will be upgraded as well. A new linear accelerator, Linac4, will replace Linac2. The PS Booster, the PS and the SPS will also be upgraded.

Chapter 3

Compact Muon Solenoid

As mentioned earlier, CMS is a multi-purpose apparatus operating in the LHC at CERN. As such, it is designed to investigate a broad range of physics in the TeV scale, like the Standard Model including the Higgs boson, and to search for new physics as extra dimensions, supersymmetry, or particles that could be responsible for Dark Matter. The CMS detector is built around a huge solenoid magnet that can generate a magnetic field of around 4 T. The whole detector and the magnet weight 14000 and 12000 tonnes, respectively.

The CMS experiment consists of a number of detector subsystems working in coalition. Each is designed to measure different properties of the subatomic debris that emerges from the particle collisions taking place at its centre. By combining the outputs of each of these, physicists are able to reconstruct the events that took place and gain an insight into the underlying physics. [49]: The Silicon Tracker, the Electromagnetic Calorimeter, the Hadron Calorimeter, the Muon System, the Magnet System, and the Trigger and Data Acquisition systems. A schematic view of the CMS showing the layered structure of its subsystems is shown in Figure 3.1 and Figure 3.2.

3.1 Subsystems

3.1.1 Superconducting magnet

One outstanding feature of CMS is definitely its powerful superconducting magnet. It works at a temperature of $3.5°K$ and is able to generate a 3.8T magnetic field, which is oriented parallel to the z axis as shown in Figure 3.3. These powerful magnets are used to bend charged particle trajectories, as charged particles having a transverse momentum component inside the field will suffer a deflection due to the Lorentz force and the bending

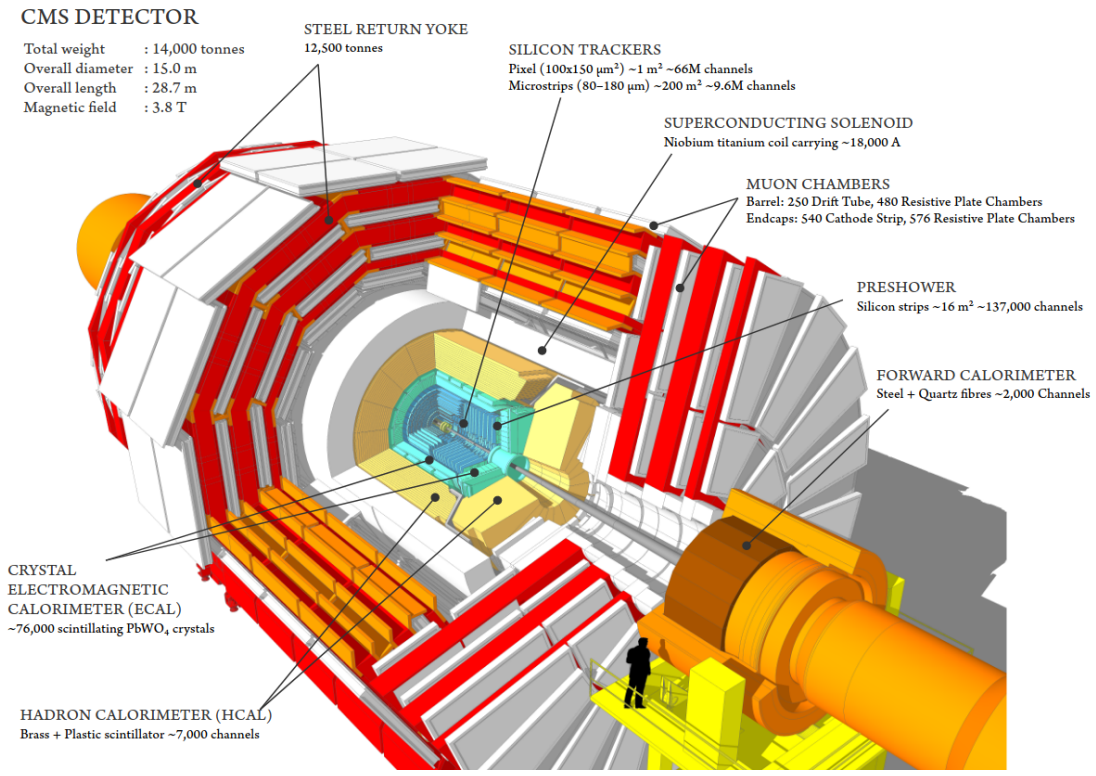

FIGURE 3.1: CMS Phase 1 detector cutaway diagram showing the different subsystems [11]. (Go back to Compact Muon Solenoid)

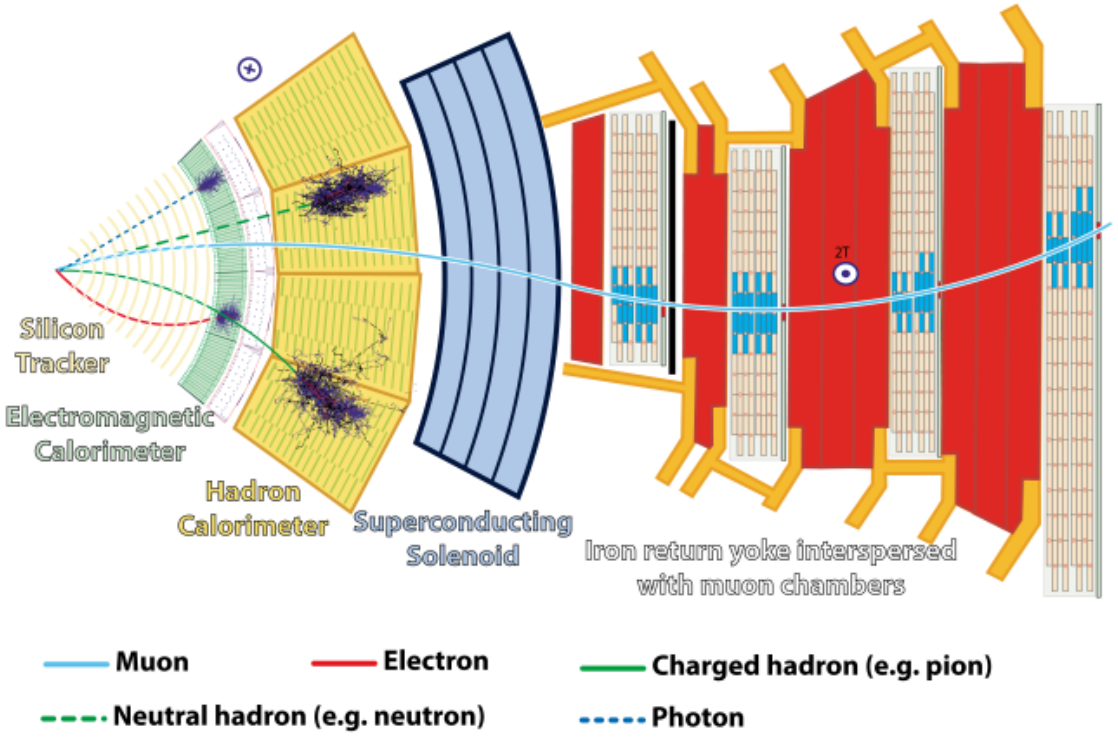

FIGURE 3.2: CMS slice showing the different subsystems and the tracks left by different types of particles [12]. (Go back to Compact Muon Solenoid, Superconducting magnet)

radius can be calculated from the tracks. An example of tracks bending is shown in Figure 3.2. The bending radius is used for calculating the transverse momentum, which is of great importance. The magnet is composed of a superconducting solenoid coil made of niobium-titanium and an iron return yoke. The tracker and the calorimeter fit inside the magnet coil, and the muon chambers are interleaved between the layers of the iron yoke. This design allows efficient and fast muon triggering, which is an advantage for the goals of this detector. More information can be found in [50].

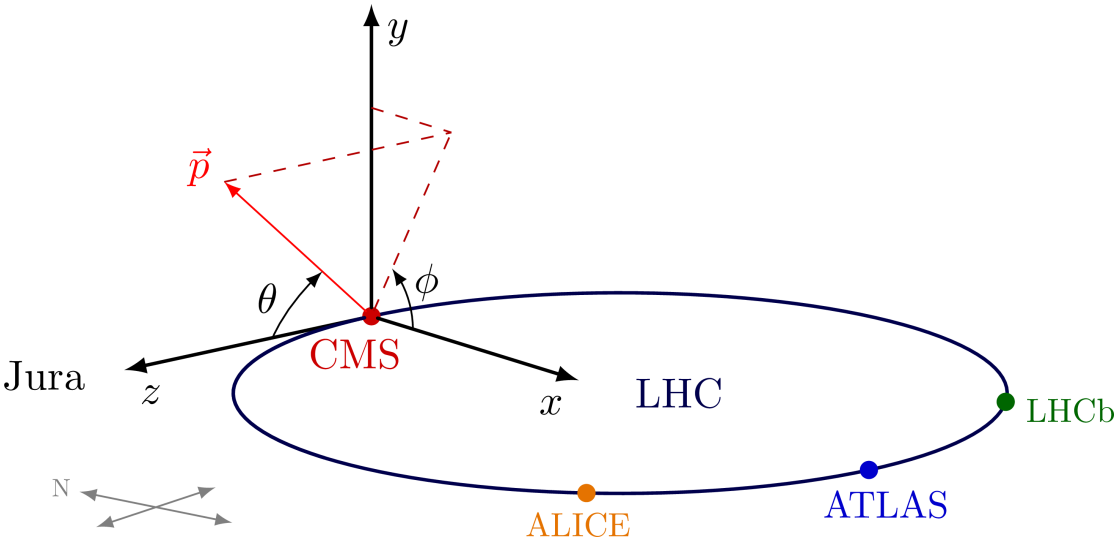

FIGURE 3.3: CMS conventional coordinate system [13]. (Go back to Superconducting magnet)

3.1.2 Inner tracking system

The CMS inner tracking system is composed by two subsystems, both being based on silicon detector technology. The innermost one is the pixel detector and it is designed with a cylindrical symmetry. The silicon strip tracker, which surrounds the pixel detector, is composed of 10 barrel layers extending outwards to a radius of 1.1 m. The original pixel barrel system was replaced during the end-of-year extended technical stop between 2016 and 2017 with an upgraded version (Phase-1) . Compared to the original pixel detector, the upgraded detector has a better tracking performance and lower mass with four barrel layers and three end-cap disks on each side to provide hit coverage up to an absolute value of pseudorapidity of $|\eta| = 2.5$. Pseudorapidity is defined as:

$$\eta = -\log\left(\frac{\tan\theta}{2}\right), \tag{3.1}$$

where the polar angle θ is the angle between the *z-axis* and the projection of the momentum of the particle onto the *y-z* plane. θ lies in the range $[0, \pi]$.

The layout of the Phase 1 Tracker is shown in Figure 3.4. The tracker is composed of a total of 1440 pixel and 15148 strip detector modules covering around 200 m^2 of active silicon surface. More information can be found in [51], [15].

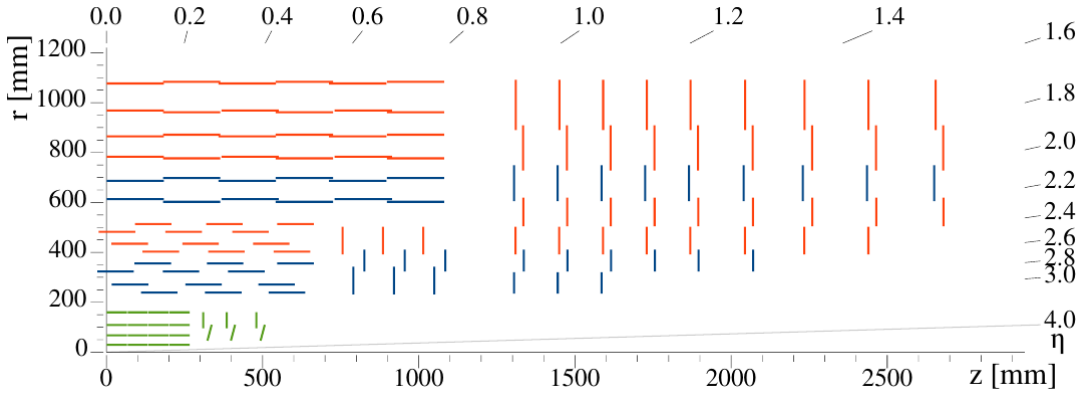

FIGURE 3.4: Sketch of one quarter of the Phase-1 CMS tracking system in r-z cut. The pixel detector is shown in green. Single-sided and double-sided strip modules are depicted in red and blue colors, respectively [14]. (Go back to Inner tracking system)

3.1.2.1 Pixel detector

The Pixel detector is the innermost system of all CMS and it is fully built using silicon pixel sensors with a size of 100×150 μm^2 reaching a total of 124 million channels. This system is the most exposed to radiation effects in the CMS, as the density of particles per unit of volume is maximal. This leads to a higher fluence and particle occupancy with respect to the rest of the sub-systems. Good spatial and time resolution, and radiation hardness are required for operating in these conditions successfully.

The Pixel detector is composed by the Barrel Pixel Detector (BPix) with 4 barrel layers and 3 disks in each end-cap in the Forward Pixel Detector (FPix). BPix layers are located at mean radii of $29mm$, $68mm$, $109mm$, and $160mm$. The FPix disks which extend from 6 to 15 cm in radius will be placed on each side at $z = \pm 34.5$ and $z = \pm 46.5$ cm. A diagram comparing the original layout (Phase 0) with the Phase 1 design can be seen in Figure 3.5. More information can be found in [51].

3.1.2.2 Silicon strip tracker

The silicon strip tracker works in a similar way as the pixel detector but the sensors take the shape of a long strip. The detector is composed by 4 subsystems: the Inner Barrel Tracker (TIB), the Inner Disks tracker (TID), the Outer Barrel Tracker (TOB) and outer End-Caps Tracker (TEC).

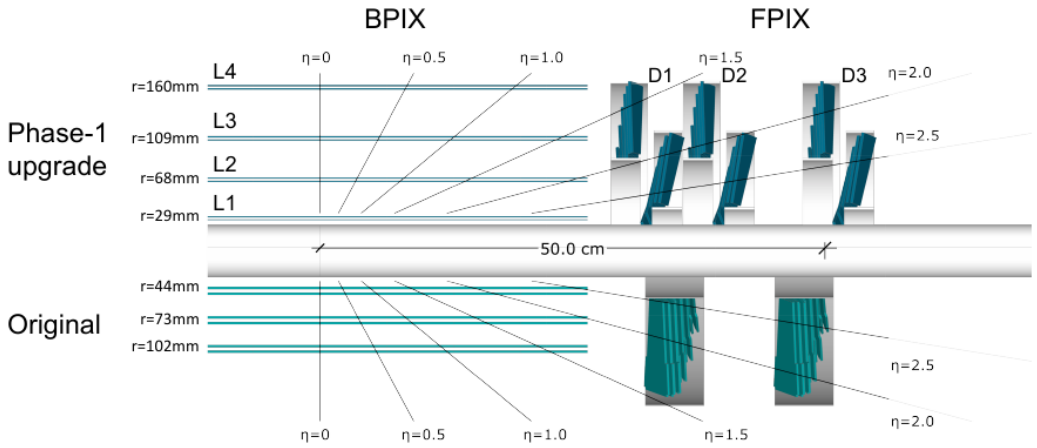

FIGURE 3.5: CMS Phase 1 pixel detector compared to the original detector [15].
(Go back to Inner tracking system)

The TIB/TID subsystems implement 320 μm thick silicon micro-strip sensors with their strips parallel to the beam axis in the barrel and along the radial direction on the disks. The strip pitch is 80 μm on layers 1 and 2, and 120 μm on layers 3 and 4 in the TIB, leading to a single point resolution of 23 μm and 35 μm, respectively. In the TID, the mean pitch varies between 100 μm and 141 μm. The TIB and TID are surrounded by the TOB. It has an outer radius of 116 cm and consists of 6 barrel layers of 500 μm thick micro-strip sensors with strip pitches of 183 μm on the first 4 layers, and 122 um on layers 5 and 6. The tracking system extends up to a value of $|\eta|$=2.4. More information can be found in [51].

3.1.3 Electromagnetic calorimeter

The Electromagnetic calorimeter (ECAL) is an homogeneous calorimeter designed to measure the energy of electrons and photons as they are stopped completely inside its volume. These particles are of particular interest in the study of the Higgs boson and the search for new physics. The detector is build up using lead tungstate crystals. Lead tungstate is a very dense material but transparent to light and exhibits scintillation when particles deposit energy on it. Scintillation light is then detected by photodetectors, where the light yield is proportional to the amount of energy deposited in the crystals and the penetration depth is proportional to the logarithm of the energy deposition. The latter allows to keep this type of detectors compact.

The geometry of the calorimeter includes a cylindrical barrel section with two end-cap discs which ensure hermeticity is kept in order to prevent particles escaping and being

undetected. The ECAL can be considered the second layer of detectors, being located between the Silicon tracker and the Hadronic calorimeter. The barrel consists of 61,200 crystals grouped into 1700 crystal modules. The end-caps seal off the barrel at both ends and consist of 15,000 crystals. The ECAL also includes a pre-shower detectors located in front of the end-caps to help distinguish single high-energy photons from lower energy photon pairs. More information can be found in [50].

3.1.4 Hadron calorimeter

The Hadron calorimeter (HCAL) is a sampling calorimeter that measures the energy of hadrons (e.g. protons, neutrons, and pions). It is designed to be hermetic as this aspect is crucial to ensure a precise event reconstruction. Its aim is to capture, as far as possible, all particles emerging from the collisions, such that the reconstructed imbalance of momentum and energy in the traverse direction to the beam can be used in the search for invisible particles or new physics.

It is composed of brass and steel layers as absorbing material, interleaved with fluorescent scintillator tiles. As hadronic particles traverse the absorber layers, they produce various secondary particles which can themselves cross other layers and produce more particles, thus creating a particle shower. The progression of the shower through the layered scintillator produces light that will be measured.

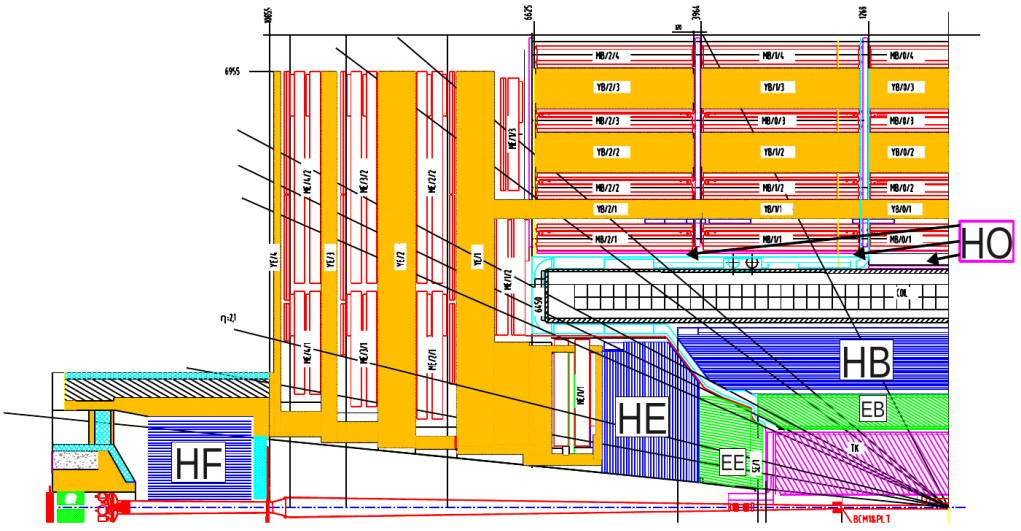

Figure 1.2: An r-Z schematic drawing of a quarter of the CMS detector showing the location of the HB, HE, HO, and HF calorimeters in CMS.

FIGURE 3.6: Sketch of one quarter of the CMS detector in r-z cut showing the barrel (HB), end-caps (HE), outer (HO), and forward (HF) calorimeters [16]. (Go back to Hadron calorimeter)

The HCAL is composed by the Barrel Hadronic Calorimeter (HB), End-caps Hadronic Calrimeter (HE), Outer Hadronic (HO), and forward (HF) calorimeters, as it is shown in Figure 3.6. The pseudorapidity region with $\eta < 1.3$ is covered by HB and HO, $1.3 < \eta < 3$ is covered by HE. The region $3 < \eta < 5$ is covered by HF. More information can be found in [16].

3.1.5 The muon system

The CMS most important task is to detect muons and this is achieved by a robust system that allows fast identification and good momentum resolution. Muons are produced in the Higgs boson decay H$\rightarrow ZZ \rightarrow 4\mu$, for example.

Because muons can easily traverse the previous layers of the detector without being absorbed, the muon chambers are placed as the last system and are composed by 3 subsystems, each using a different gaseous detector technology. Drift Tube gas chambers (DTs), which have good spacial resolution at a low flux, are interleaved with the iron return yoke in the barrel and cover the pseudorapidity for $\eta \leq 1.2$. Cathode Strip Chambers (CSCs) are located in the end-caps and cover $0.9 < \eta < 2.4$. Finally, Resistive Plate Chambers (RPCs), which have good time resolution, are present in the barrel and in the end-caps and complement the other two systems.

The RPC time resolution is of the order of nanoseconds and its information are used by the trigger system to make immediate decisions on whether to keep or discard the event. Muon transverse momentum and position information is also used by the tracker system allowing it to increase its performance.

3.1.6 Trigger and data acquisition

At maximum performance, CMS hosts around 1 billion pp interactions every second with a bunch-crossing time of 25 ns. It is naturally not viable and too expensive to read-out, process, and store this amount of data (ca. 40 TB), and even if it could be done, the great majority of events are "soft" collisions which are well studied and are of little or no interest when seeking for evidence of new physics.

The decision of whether an event will be kept or discarded is taken by the CMS trigger system which is composed of the Level-1 Trigger (L1T) and the

The L1 trigger works with an input data frequency of 40 MHz and produces an output of 100 KHz. It has around 1 μs to make a decision. This system provides an extremely fast and automatic decision based on whether an event produced interesting decay products,

as particles with large amount of energy. The data feeding the L1 trigger comes from the muon detector and the calorimeters.

After L1 trigger has decided to keep an event, data from all the other sub-detector systems will be fed into the HL trigger for further decision making. The HL trigger works with an input data frequency of 100 KHz and produces and output of 1 KHz. It has around 40 ms to make a decision. A diagram with the Trigger system is shown in Figure 3.7.

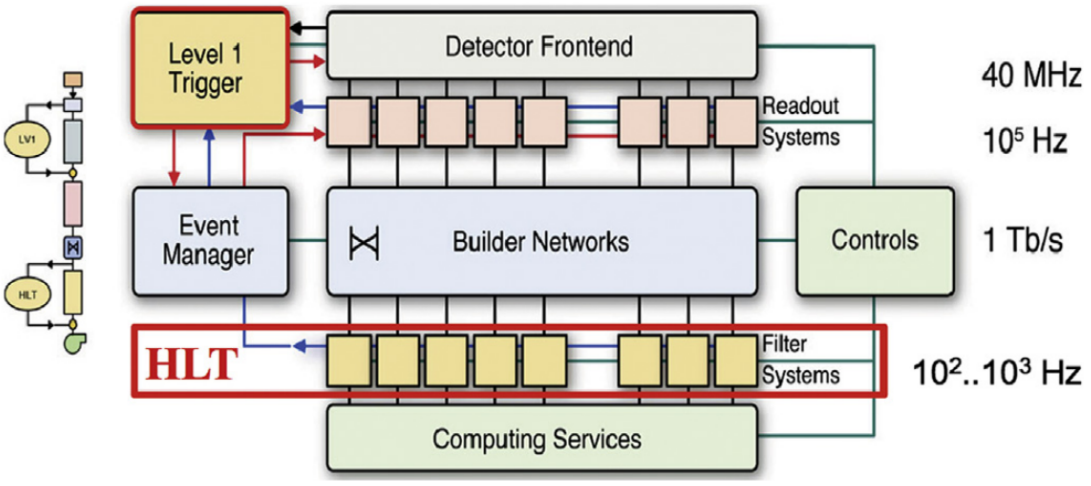

FIGURE 3.7: Overview of the CMS trigger system [17]. (Go back to Trigger and data acquisition)

The HL trigger employs complex algorithms that also include tracking information to reconstruct the events while having different trigger channels working in parallel. Data from events selected out by the trigger system is handled by a distributed computing and data storage infrastructure called Worldwide LHC Computing Grid (WLCG). This grid is composed by 4 different tiers or levels, that store, processes, and analyses data. The computing power of the grid comes from tens of thousand of standard CPUs around the world collaborating in parallel.

At peak performance, more than 5 petabytes of information per year are processed by the WLCG.

Chapter 4

CMS Phase-2 Upgrade

The CMS detector will undergo a mayor upgrade, commonly referred to as Phase-2. This upgrade will serve as preparation for the HL-LHC era to be able to cope with the high-radiation environment and to fully exploit the increase in luminosity.

The detector will need improved radiation hardness for the high radiation environment in which it will work, higher granularity to adequately manage the larger pileup and high particle density, larger bandwidth to be able to cope with the increased data rates, and an improved trigger that can perform adequately under demanding conditions. Hence, some of the subsystems of CMS will be completely replaced, like the silicon tracking system, and others will receive an upgrade.

4.1 Main features

The CMS first level hardware trigger (L1) frequency will be increased to 750 kHz data rate, as compared to the actual one at 100 kHz, and the latency will be decreased from the present value of 3.2 μs to 12.5 μs. The high-level trigger (HLT) will be operated with 7.5 kHz data rate.

In the muon chambers, the front-end electronics for the Drift Tube chambers (DTs) and Cathode Strip Chambers (CSCs) will be replaced by improved versions. In the forward region, new chambers based on Gas Electron Multiplier technique (GEM) will be installed. In the barrel section, the ECAL will be equipped with new front-end boards that will allow the exploitation of the information from single crystals in the L1 trigger. Silicon photomultipliers (SiPMs) will be used in the barrel region of the HCAL for read out, instead of the actual Hybrid Photo-Diodes (HPDs). The ECAL and HCAL end-cap calorimeters will be replaced by a new sampling calorimeter based primarily on silicon

pad sensors. The new silicon tracker will have increased overall capabilities, including the new feature of track information being fed to the L1 trigger, previously exclusive to HLT. More information can be found in [14].

4.2 CMS tracker upgrade

As commented previously, before the start of the HL-LHC, both the strip tracker and the Phase 1 pixel detector will have to be replaced due to the significant damage and performance degradation they would suffer during operation at the HL-LHC environment, and to cope with the more demanding operational conditions without sacrificing the physics potential.

4.2.1 Actual tracker limitations

Accumulated radiation damage in the pixel sensors causes a reduction in the charge collection efficiency, as well as a change in the Lorentz angle. This leads to a decrease in neighbouring pixels charge sharing, and hence, to a lower spatial resolution and a reduced hit efficiency. The two most radiation sensible properties of the actual sensors are the depletion voltage and the leakage current.

Studies on the expected performance of the current tracking system as a function of integrated luminosity have shown unacceptable degradation beyond about 300 fb^{-1}. As well, limitations in readout bandwidth and trigger latency will also be present.

The new Phase-2 tracker will have to address these limitations previous exposed and will consist of an Inner Tracker (IT) based on silicon pixel modules and an Outer Tracker (OT) made from silicon modules with strip and macro-pixel sensors. More information can be found in [52].

4.2.2 Requirements for the new tracker

- **Increased radiation tolerance**

  The upgraded tracker must be fully efficient up to a target integrated luminosity of 4000 fb^{-1}, taking the *ultimate luminosity scenario* as baseline, and as well, taking in consideration the replacement of the innermost layers of the barrel and forward calorimeters, BPix L1 and FPix R1, respectively, at the term of Run 5. For an integrated luminosity baseline of 3000 fb^{-1}, FLUKa simulations [53] show that the radiation exposure of the detector in the innermost regions of the Inner tracker

will reach a fluence of $1MeV$ neutron equivalent Φ_{eq}[1] of $2.3 \cdot 10^{16}$ $\mathrm{n_{eq}cm^{-2}}$, which is about one order of magnitude higher than the requirements considered for the design of the actual tracker [55]. Thus, radiation hardness is one of the top priorities for the Phase 2 upgrade. A simulated integrated particle fluence for the Phase 2 tracker can be seen in Figure 4.1.

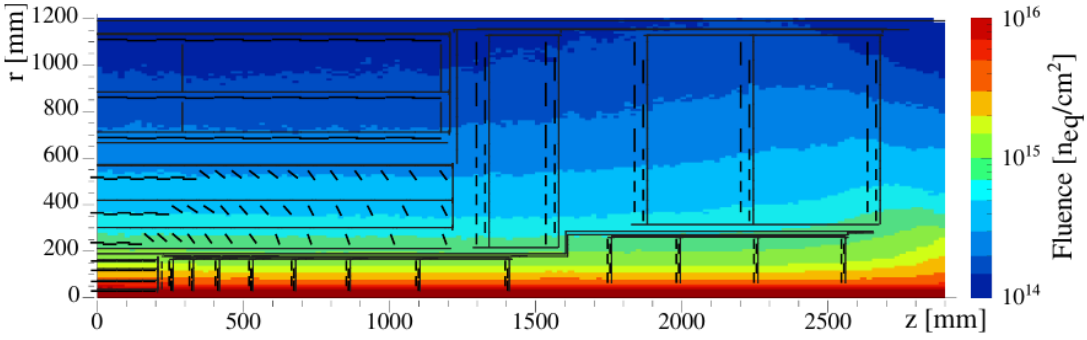

FIGURE 4.1: Integrated $1MeV$ neutron equivalent particle fluence for the Phase-2 tracker. The estimates correspond to a total integrated luminosity of $3000fb^{-1}$ of pp collisions at $\sqrt{s} = 14TeV$. The simulation was performed employing the CMS FLUKA geometry version 3.7.2.0 [14]. (Go back to Requirements for the new tracker)

- **Increased Granularity**

  Due to the high level of pile-up, to guarantee an efficient tracking performance, the channel occupancy must be kept at around or below the per cent level in the OT and per mille level in the IT, which requires a high channel density and high granularity. As well, increased granularity will help to improve two track separation, needed to fully exploit the large amounts of collision data that will be generated during high luminosity operations, and to recreate the events as precisely as possible. It is important, for example, in the di-muon decay channel of the Higgs boson. Target pile-up values of 140 and 200 collisions per bunch crossing are used to benchmark the performance of the detector.

- **Reduced material in the tracking volume**

  The amount of material affects detectors negatively and influences the performance of the tracker system, and of the overall event reconstruction in CMS. Reducing the so called *material budget* will tackle all the above and increase an overall efficiency by interfering the least with the traversing particles.

- **Robust pattern recognition**

  Fast and efficient track finding in high pile-up conditions will be of great importance and the design of the upgraded tracker takes both in consideration.

[1] Is defined as the fluence of $1MeV$ neutrons producing the same displacement damage in a silicon structure in a detector as induced by an arbitrary particle fluence with a specific energy distribution. ASTM Standard E722 $1MeV$ Silicon Equivalent Fluence Metric [54].

- **Tracking contribution to the L1T**

  Selection of interesting physics events at the L1 trigger becomes extremely challenging in high luminosity environments because of the high collision rate. Nonetheless, the CMS will use tracking information in the L1 trigger event selection, which, within others, will improve the transverse momentum resolution of numerous objects at level of L1 trigger, like particle jets, and will contribute to the mitigation of pileup.

- **Extended tracking acceptance**

  The overall CMS physics capabilities will greatly benefit from an extended acceptance of the tracker and calorimeters in the forward region. The upgraded tracking system will provide efficient tracking up to a pseudorapidity $|\eta| \approx 4$. A diagram of a quarter of the tracker layout can be seen in Figure 4.2 [14].

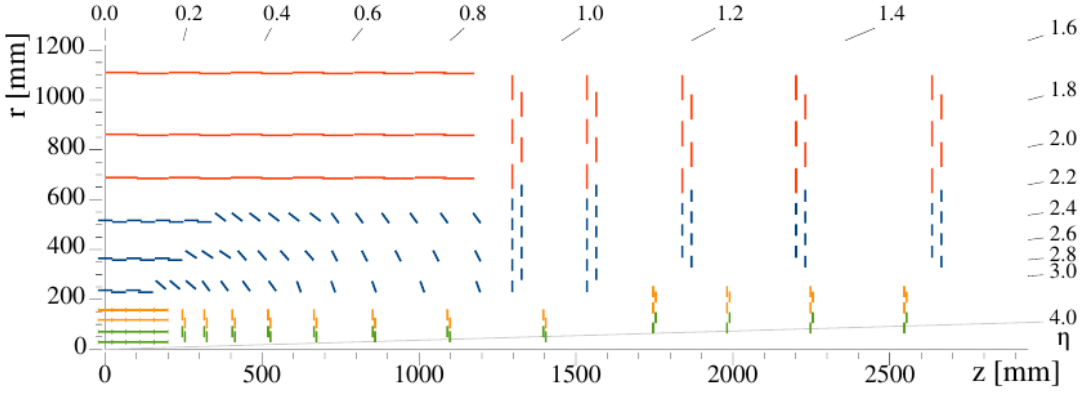

FIGURE 4.2: Sketch of one quarter of the Phase 2 CMS tracking system in r-z cut. In the IT, the green lines correspond to pixel modules made of two read-out chips and orange lines to pixel modules with four read-out chips. In the OT, the red and blue lines represent modules with two strip sensors and modules with a strip and a macro-pixel sensor, respectively [14]. (Go back to Requirements for the new tracker)

4.2.3 Inner tracker and Si pixel sensors

The IT will be exposed to extreme conditions as radiation levels of 1.2Grad of Total Ionising Dose (TID) and $1MeV$ neutron equivalent fluences Φ_{eq} of $2.3 \cdot 10^{16} \mathrm{n_{eq}}\ \mathrm{cm}^{-2}$ in the innermost layer. The hit rate will reach 3.2GHz cm^{-2}, the trigger latency will reach 12.8μs and the trigger rate, 750 kHz. In addition, the increased luminosity will be accompanied by a significant increase in the number of pileup events per collision which will grow up to 200, five times higher than the current value of ~ 40.

The new IT will be fully built by hybrid silicon pixel modules, i.e. silicon sensors read out by Application-Specific Integrated Circuits (ASICs), and will be composed of $\sim$ 2billion silicon pixels with a total 2500μm^2 of area.

The barrel part of the detector, known as TBPX, will be made out of four cylindrical layers, each 400mm long. The innermost one will be located 30mm away from the beam. The TBPX is made by two quasi-equal halves, with four and five modules per end, avoiding a projective gap at $|\eta| = 0$.

Eight small disks per end, with four rings of modules each, will compose the forward part of the detector (TFPX), while the extension to pseudorapidity of $|\eta| = 4$ will be reached with four large disks per end, containing five rings each (TEPX). A layout of a quarter of the IT detector can be see in Figure 4.4.

There are two types of modules that will be used in this layout; the two inner layers of the TBPX and the two inner rings of TFPX disks will be double-chip modules, shown in green in Figure 4.5, while the two outer layers of TBPX, the outer rings of TFPX and TEPX will be based on quad-chip modules, shown in yellow in Figure 4.5.

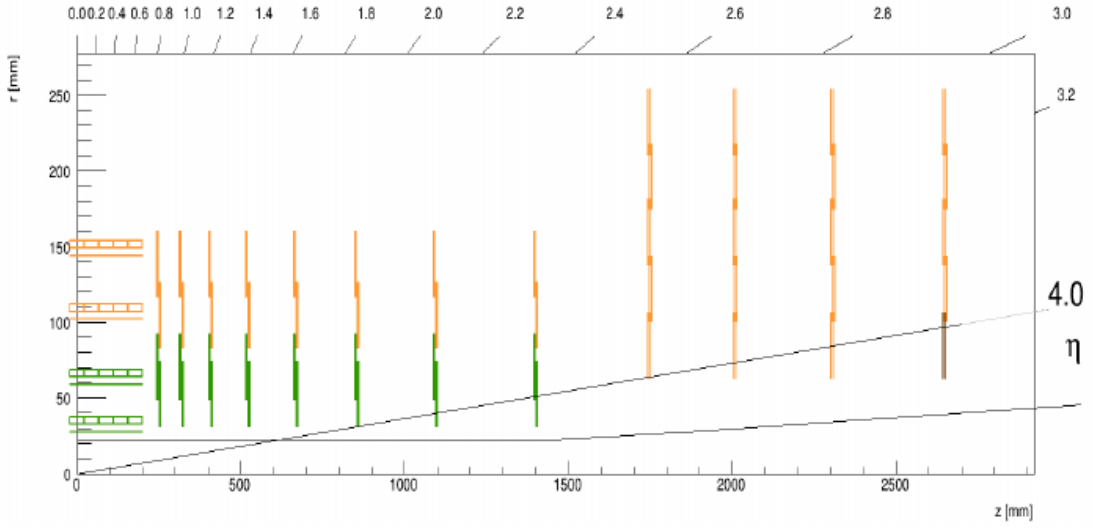

FIGURE 4.3: Sketch of one quarter of the Phase 2 CMS IT system in r-z cut. Double-chip modules are shown in green and quad-chip modules are shown in orange. [18]. (Go back to Inner tracker and Si pixel sensors)

Power, cooling, and data transmission services will be carried on a cylindrical shell enclosing the pixel detector called the service cylinder and will be independent for each quarter of the detector, Z+/Z- and X+/X-.

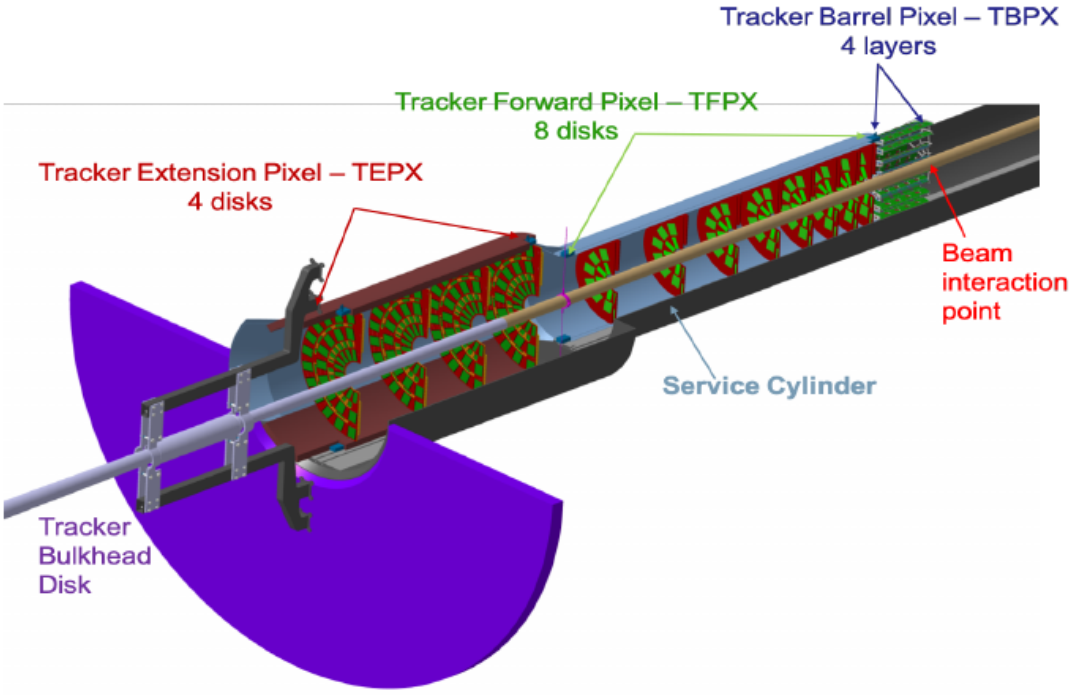

FIGURE 4.4: sketch of half of the Phase 2 IT system layout showing the TBPX, TFPX, and TEPX [18]. (Go back to Inner tracker and Si pixel sensors)

4.2.3.1 Pixel modules

- Module

  The IT modules have a relatively simple design. A High-Density Interconnect (HDI) Printed Circuit Board (PCB) is used to distribute data, commands and power to and from the modules. Figure 4.5 shows the design of the HDI for the barrel section with double-chip (left) and quad-chip modules (right). The chips of a module (dark blue) are bump bonded to the silicon sensor (light blue) which will be glued to the HDI (in green).

- Read-out ASICs and sensors

  ATLAS and CMS are carrying out a Research and Development (R&D) project in the framework of RD53A [56] with the objective of creating radiation-hard small-pitch pixel sensors in $65nm$ Complementary Metal–Oxide–Semiconductor (CMOS) technology compatible with the RD53A Read-Out Chip (ROC) [57]. Achieving high efficiencies for $1MeV$ neutron equivalent fluences Φ_{eq} higher than $1.0 \cdot 10^{16}$ $\mathrm{n_{eq}cm^{-2}}$ levels is challenging and requires an equally radiation hard ASIC to read out the sensor. Special light-carrier boards hosting single-chip pixel modules with minimised material have been developed and allow an easy handling of irradiated modules during irradiations and test-beams. The aspect ratio of the pixel can be

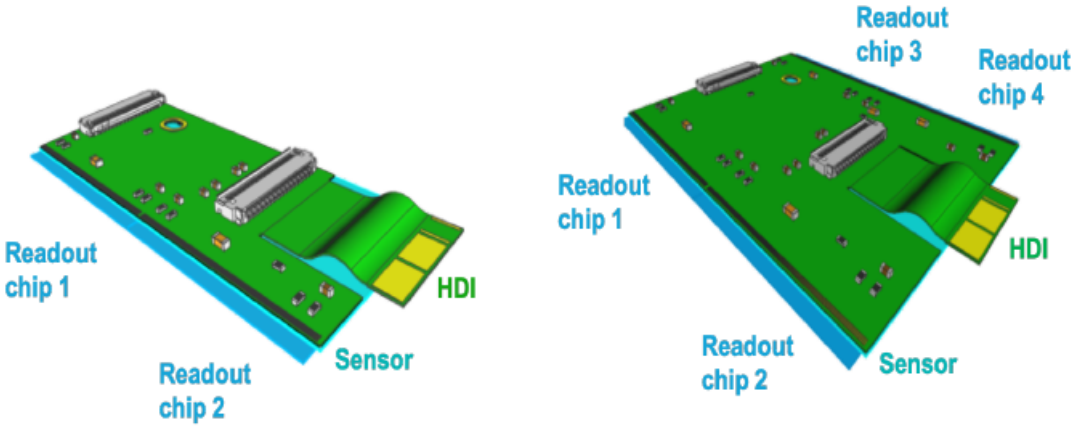

FIGURE 4.5: Sketch of the Phase 2 modules for the IT system. 1×2 module and 2×2 module design are shown in the left and right, respectively [18]. (Go back to Pixel modules)

either square, with 50x50μm^2, or rectangular, with 25x100μm^2. Pixel area will be decreased by a factor of 6 compared to Phase 1, allowing them to achieve low occupancy and improved track separation. The readout ASIC has a cell size of 50x50μm^2 and it can be used to test pixel modules of both ratios.

Two options of sensor technology are being explored: thin planar sensors and 3D sensors, both of $\sim$ 150μm active thickness. The thin planar n-in-p sensors are the baseline choice for the CMS IT outer layers and rings. They require high bias voltage ($600V - 800$V) for efficient charge collection after irradiation at the maximum fluences foreseen for Phase 2 [18].

- Read-out

  The e-links used for the readout of the pixel chips will be running at 1.28 Gbps and will be carrying the data from L1 trigger, as well as monitoring information from the Data Aquisition (DAQ) and control system. In total, there will be 7k readout channels and 4k control e-links used in the CMS IT system to connect the modules to the port-cards, where the transformation from the electrical to the optical stage of the signals will take place.

Each pixel chip will consume about $\sim$ 2A and will need a supply voltage of 1.4-1.5 V. Around 50kW will be required to be delivered to the Inner Tracker system to power the 4000 pixel modules. Most of this power will be consumed by the ASICs. The use of Direct Current (DC) power conversion has been excluded due to radiation hardness and material budget reasons. Therefore, a serial power distribution system has been proposed to power the pixel modules [14].

Chapter 5

Particle detector physics and radiation damage

The Following chapter will offer a theoretical framework of the relevant physics phenomena behind particle detectors and radiation damage for the research done.

The following sub-chapters are heavily based on the following sources:

[19] ,[28] ,[58] ,[59] ,[22] ,[28] ,[25] ,[60] ,[26] ,[21] ,[23].

5.1 Semiconductor physics

Solid-state materials can be grouped into three classes: insulators, semiconductors, and conductors. Figure 5.1 shows the range of electrical conductivities σ and the corresponding resistivities $\rho = 1/\sigma$ for some important materials in each group. Insulators, like fused quartz and glass, have very low conductivities, on the order of $10^{-18} S/cm$ to $10^{-8} S/cm$. On the other hand, Conductors, such as aluminium and silver, have high conductivities, typically ranging from $10^{4} S/cm$ to $10^{6} S/cm$. Semiconductors have conductivities between those of insulators and those of conductors and are generally sensible to temperature, illumination, magnetic fields, and impurity atoms. This sensitivity in conductivity makes the semiconductor one of the most important materials for electronic applications.

Currently, Si (Silicon) is one of the most studied elements in the periodic table, and silicon technology is by far the most advanced among all semiconductor technologies. This is due to several reasons: favourable energy band-gap, possibility to tune the band-gap properties, natural abundance and lower cost of device-grade silicon than any other semiconductor material.

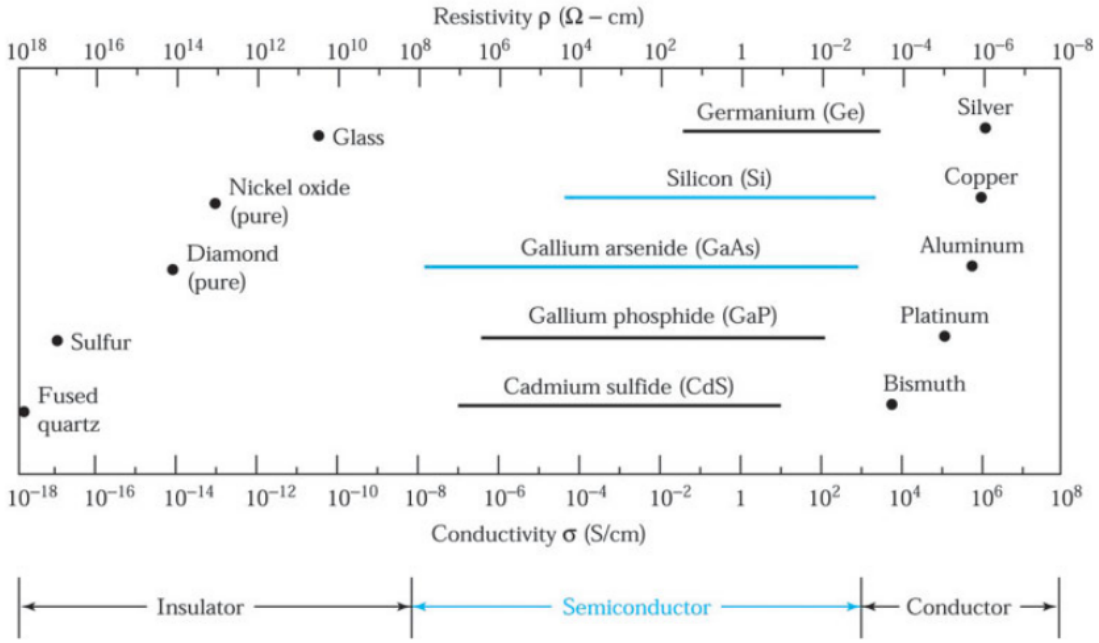

FIGURE 5.1: Typical range of conductivities for insulators, semiconductors, and conductors [19]. (Go back to Semiconductor physics)

The semiconductor materials that will be studied are single crystals; that is, the atoms are arranged in a three dimensional periodic structure. The periodic arrangement of atoms in a crystal is called a lattice. In a crystal, an atom never moves far from a single, fixed position. The thermal vibrations associated with the atom are centred about this position. We will restrict the treatment of semiconductor physics to crystalline material as it is of interest for the research performed.

5.1.1 Crystal structure

Most commonly used semiconductors are single crystals with diamond lattice like Si and Ge (Germanium) or zincblende lattice like GaAs (Gallium Arsenide) and other compound semiconductors, as shown in Figure 5.2.

The lattice is arranged in a tetrahedron shape, as shown in Figure 5.3a, and each atom shares its four outer valence electrons with those of the neighbours forming covalent bonds. A schematic two-dimensional representation of this situation, which does not conserve the relative position of the atoms, is shown in Figure 5.3b.

5.1.2 Energy bands

The schematic two-dimensional representation of the tetrahedron may be generalised to present a complete crystal, as shown in Figure 5.4. At low temperatures all valence

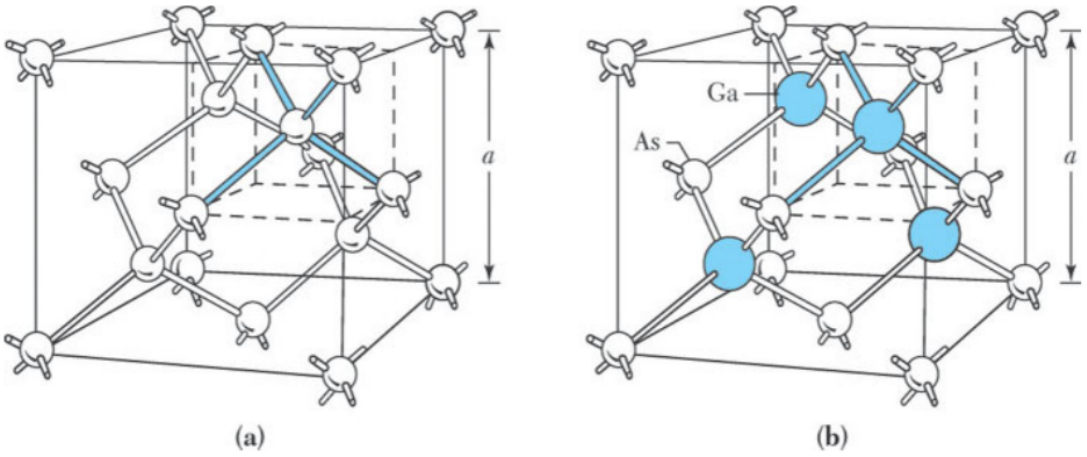

FIGURE 5.2: (a) diamond lattice, (b) zincblende lattice [19]. (Go back to Crystal structure)

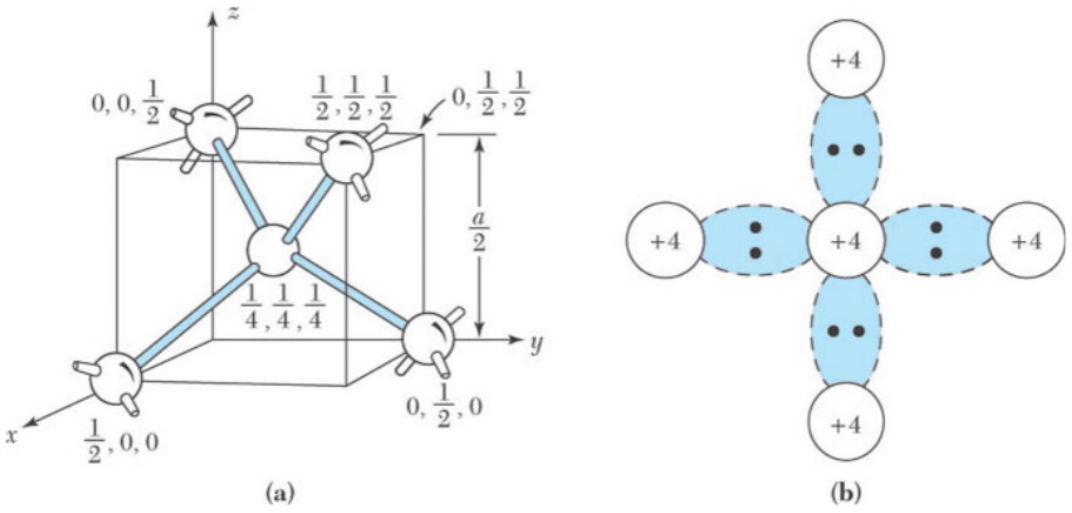

FIGURE 5.3: (a) a tetrahedron bond, (b) schematic two-dimensional representation of a tetrahedron bond [19]. (Go back to Crystal structure)

electrons remain bound in their respective tetrahedral lattice but at higher temperatures thermal vibrations may break the covalent bonds and a valence electron may become a free electron, leaving behind a free hole. Both the electron and the hole are then available for conduction.

In Figure 5.5, the energy levels as a function of the lattice spacing are shown for two energy levels in silicon, where it can be seen that at very large distances each atom has the same two energy levels. Then, if the two atoms approach to each other, the electron wave functions begin to overlap and the energy levels split into two, explained by Pauli's exclusion principle. For the same reason, when N atoms come together to form a solid, each energy level splits into N separate but closely spaced levels, thereby, resulting in a continuous band of energy levels for each quantum number n. It is considered continuous,

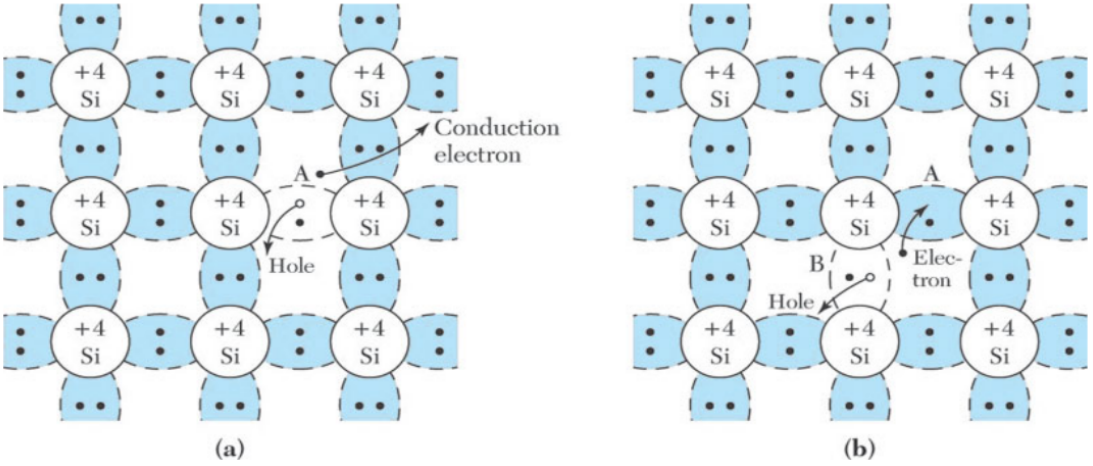

FIGURE 5.4: The basic bond representation of intrinsic silicon. (a) a broken bond at position A, resulting in a conduction electron and a hole. (b) a broken bond at position B [19]. (Go back to Energy bands)

partly because the separation between energy levels becomes comparable with the lattice vibrational energy, to which the electrons are strongly coupled, and partly because the separation in energy levels also becomes comparable with the time averaged energy uncertainty, explained by Heisenberg's uncertainty principle.

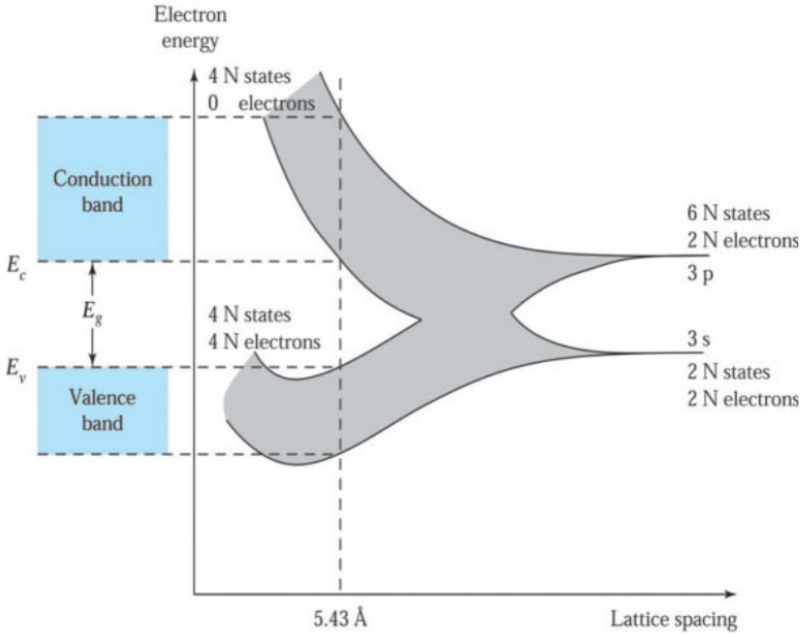

FIGURE 5.5: Formation of energy bands as a diamond lattice crystal is formed by bringing isolated silicon atoms together [19]. (Go back to Energy bands)

The spacing of 5.43 Å shown in Figure 5.5 corresponds to the minimum total energy of the electrons, not very far from the minimum energy of the electrons in the filled valence band. At low temperature the crystal reaches a completely filled valence band and an

empty conduction band; at room temperature the thermal energy is high enough to lift a few electrons to the conduction band, thus creating a weak conductivity due to free electrons and holes.

5.1.2.1 Direct and indirect band-gap

In semiconductor physics, the band-gap of a semiconductor can be of two basic types, a direct band-gap or an indirect band-gap, as shown in Figure 5.6. The minimal-energy state in the conduction band and the maximal-energy state in the valence band are characterised by a certain crystal momentum (k-vector) in the Brillouin zone. If the k-vectors are different, the material has an indirect gap. The band-gap is called direct if the crystal momentum of electrons and holes is the same in both the conduction band and the valence band, such that an electron can directly emit a photon. In an indirect gap, a photon cannot be directly emitted because momentum is not shared and the electron will have to pass through an intermediate state, transferring momentum to the crystal lattice.

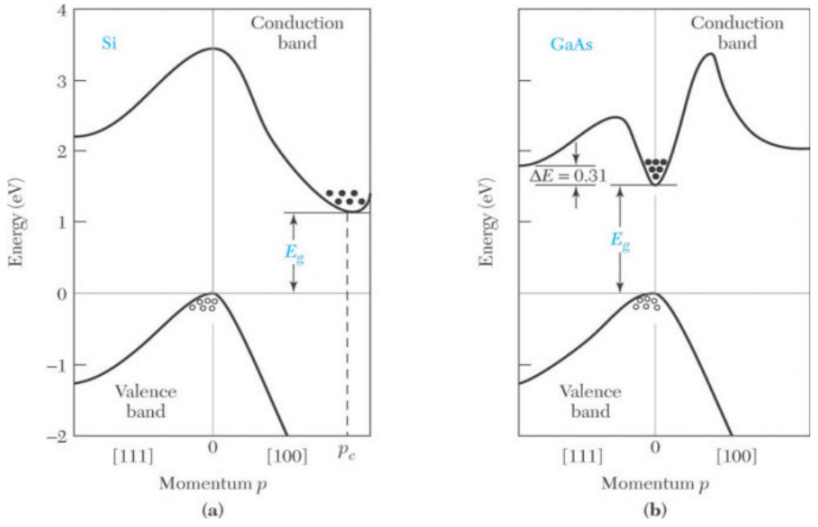

FIGURE 5.6: Energy band structures of (a) Si and (b) GaAs. Circles indicate holes in the valence bands and dots indicate electrons in the conduction bands [19]. (Go back to Direct and indirect band-gap)

For silicon, as in Figure 5.6a, the maximum energy in the valence band occurs at $p = 0$, but the minimum energy in the conduction band occurs along the [100] direction at $p = p_c$, which is the momentum at the minimum energy of the conduction band. Therefore, when an electron makes a transition from the maximum point in the valence band to the minimum point in the conduction band, not only an energy change ($\geq E_g$) but also some momentum change ($\geq p_c$) is required. For gallium arsenide, as in Figure 5.6a, the maximum in the valence band and the minimum in the conduction band occur at

the same momentum ($p = 0$). Thus, an electron making a transition from the valence band to the conduction band can do so without a change in momentum. This difference between direct and indirect band structure is very important for light-emitting diodes and semiconductor lasers as they require direct semiconductors to generate photons efficiently.

5.1.3 Intrinsic and extrinsic semiconductors

Ideal intrinsic semiconductors contain no impurities compared with the number of thermally generated electrons and holes; in practice, very few. For estimating the number of free charge carriers (electrons and holes) under equilibrium conditions we recur to the occupation probability of an electronic state. The probability that an electron occupies an electronic state with energy E is given by the Fermi–Dirac distribution function:

$$F(E) = \frac{1}{1 + \exp\left(\frac{E - E_F}{k_B \cdot T}\right)}, \tag{5.1}$$

where k_B is the Boltzmann constant, T is the absolute temperature in degrees Kelvin, and E_F is the energy of the Fermi level. The Fermi level is the energy at which the probability of occupation by an electron is exactly 1/2.

The distribution function $F(E)$ versus the energy $E - E_F$ for various temperatures is shown in Figure 5.7.

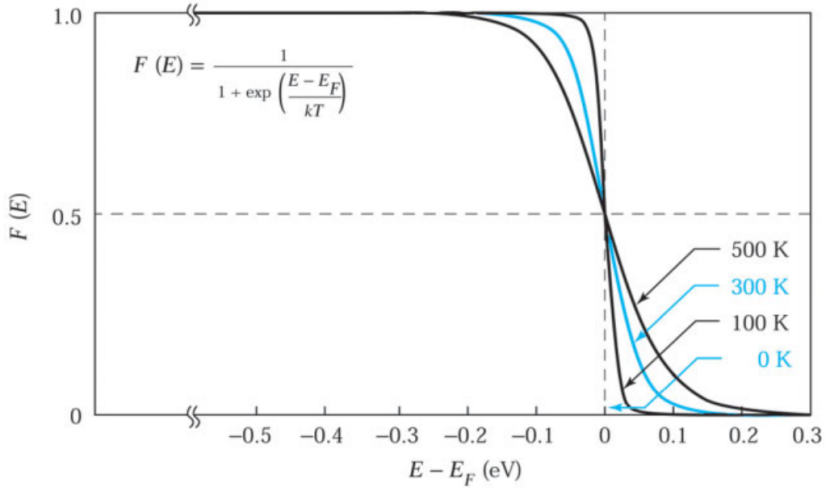

FIGURE 5.7: Fermi distribution function $F(E)$ versus $(E - E_F)$ for various temperatures [19]. (Go back to Intrinsic and extrinsic semiconductors)

Equation 5.1 can be approximated separately for electrons and holes for certain energy ranges:

$$F_n(E) \cong \exp\left(\frac{E_F - E}{k \cdot T}\right), \text{ for } (E - E_F) > 3k_BT, \tag{5.2}$$

$$F_p(E) \cong 1 - \exp\left(\frac{E - E_F}{k \cdot T}\right), \text{ for } (E - E_f) < 3k_BT, \tag{5.3}$$

These last equations can be regarded as the probability that an electron or whole occupies a state located at energy E.

The density of states in the conduction and valence bands is obtained by considering the number of states $N(E_{kin})$ in the unit volume in a small kinetic-energy interval dE_{kin} around E_{kin}:

$$N(E_{kin})dE_{kin} = 4\pi\left(\frac{2m}{h^2}\right)^{\frac{3}{2}} E_{kin}^{\frac{1}{2}} dE_{kin} \tag{5.4}$$

Regarding Figure 5.8, the density of states N(E), which varies as E for a given electron effective mass, the Fermi distribution function, and the carrier concentrations for an intrinsic semiconductor are shown. The density of free electrons n is obtained by integrating the carrier concentration $n(E)$ (5.8d) obtained by operating the product of the density of states $N(E)$ (5.8b) and the occupation probability $F_n(E)$ (5.8c) over the conduction band. The upper shaded area in Figure 5.8d corresponds to the electron density.

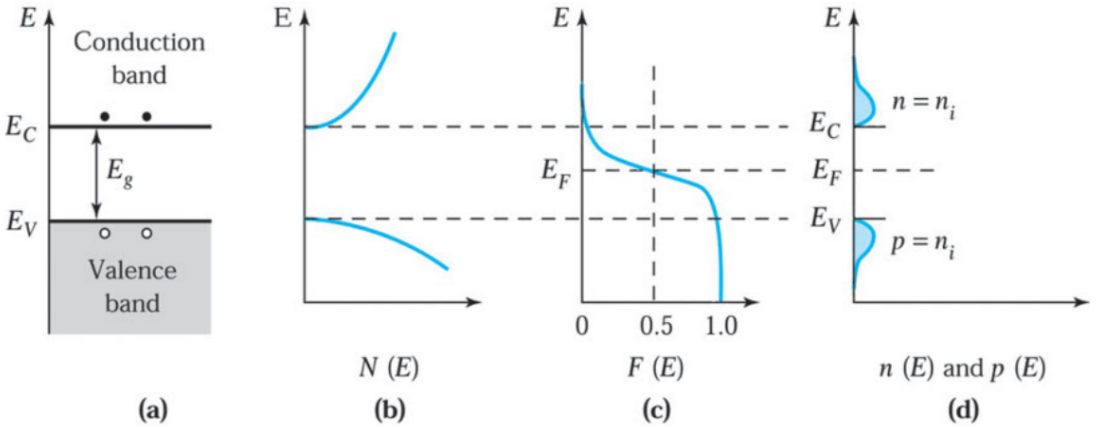

FIGURE 5.8: Intrinsic semiconductor. (a) schematic band diagram, (b) density of states, (c) Fermi distribution function, (d) carrier concentration [19]. (Go back to Intrinsic and extrinsic semiconductors)

There are a large number of allowed states in the conduction band. However, for an intrinsic semiconductor there will not be many electrons in the conduction band. Therefore, the probability of an electron occupying one of these states is small.

The density of free electrons n is then:

$$n = N_C \exp\Big(\frac{E_F - E_C}{k_B T}\Big), \tag{5.5}$$

similarly for holes, we have:

$$p = N_C \exp\Big(\frac{E_V - E_F}{k_B T}\Big), \tag{5.6}$$

where N_C and N_V are the effective densities of states in the conduction and valence bands, respectively, and E_C and E_V are the energies of the bottom of the conduction band and at the top of the valence band, respectively.

Intrinsic semiconductors are rarely used in semiconductor devices since it is extremely difficult to obtain sufficient purity in the material. Moreover, in most cases one intentionally alters the properties of the material by adding small amounts of specific impurities to the material, which is commonly referred to as doping. Depending on the type of the impurity, the doping results in an n-type semiconductor with an excess of electrons in the conduction band or a p-type with additional holes in the valence band.

Figure 5.9 shows a two-dimensional schematic bond representation of a silicon crystal with one silicon atom replaced by an (a) arsenic atom with five valence electrons, and one with one silicon atom replaced by a (b) boron atom with three valence electrons. In the former, only four electrons are used in the formation of covalent bonds between the arsenic atom and neighbouring atoms, while the fifth is not bound to a specific atom but is free for conduction at a moderate temperature. We say that the arsenic atom is a donor and the silicon becomes of n-type because of the addition of the negative charge carriers. Similarly, in the latter case, an additional electron is accepted to form four covalent bonds around the boron, and a positively charged hole is created in the valence band. This is a p-type semiconductor and the boron plays as acceptor.

It should be stressed that the crystal as a whole remains uncharged, since the charge of the free electron is compensated by the excess charge of the arsenic nucleus bound in the crystal lattice.

The replacement of a native atom of the lattice by a different atom is accompanied by the creation of localised energy levels in the band-gap. These levels may be of donor E_D or acceptor E_A type. If donor levels E_D are close to the conduction band, as is the case of phosphorous or arsenic atoms in silicon, these states will be almost completely ionised at room temperature and the electrons will be transported to the conduction band, as shown in Figure 5.10a. This is due to the many nearby states with similar energy level in

the conduction band, with which the donor states have to share their electrons. Likewise, for the acceptor levels close to the valence band, the states will be populated almost completely and holes will be created in the valence band, as shown in Figure 5.10b.

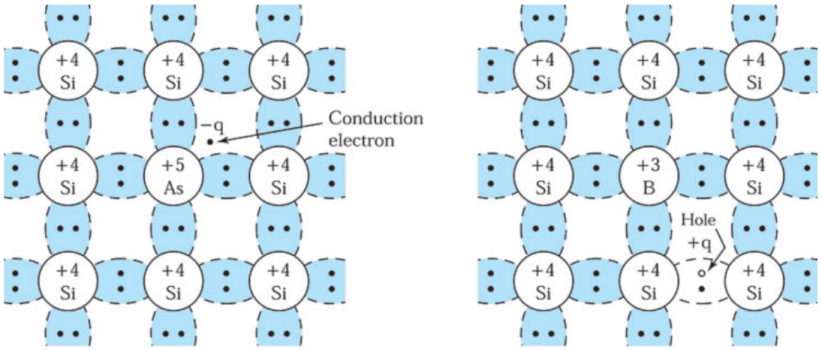

FIGURE 5.9: Schematic energy band representation of extrinsic semiconductors with (a) donor ions and (b) acceptor ions [19]. (Go back to Intrinsic and extrinsic semiconductors)

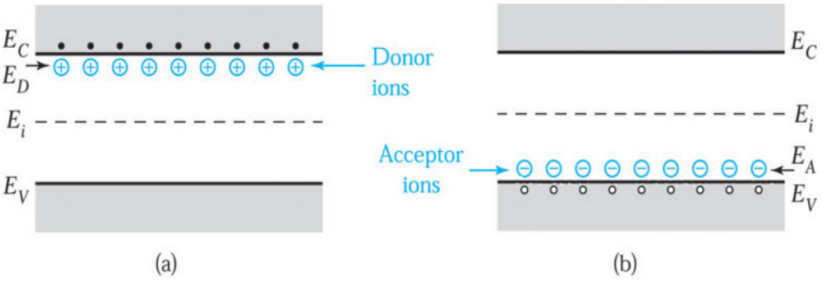

FIGURE 5.10: two-dimensional schematic bond representation of an extrinsic silicon crystal doped with (a) one arsenic atom and (b) one boron atom. [19]. (Go back to Intrinsic and extrinsic semiconductors)

We can then express the electron and hole densities in terms of the intrinsic carrier concentration n_i and the intrinsic Fermi level E_i.

$$n = n_i \exp\left(\frac{E_F - E_i}{k_B T}\right) \tag{5.7}$$

$$p = n_i \exp\left(\frac{E_i - E_F}{k_B T}\right) \tag{5.8}$$

The energy band representation for donors and acceptors in an extrinsic semiconductor can be seen in Figure 5.11.

The increase of majority carriers (electrons in the case of n-type material) is accompanied by a decrease of minority carriers according to the mass-action law $n \cdot p = n_i^2$.

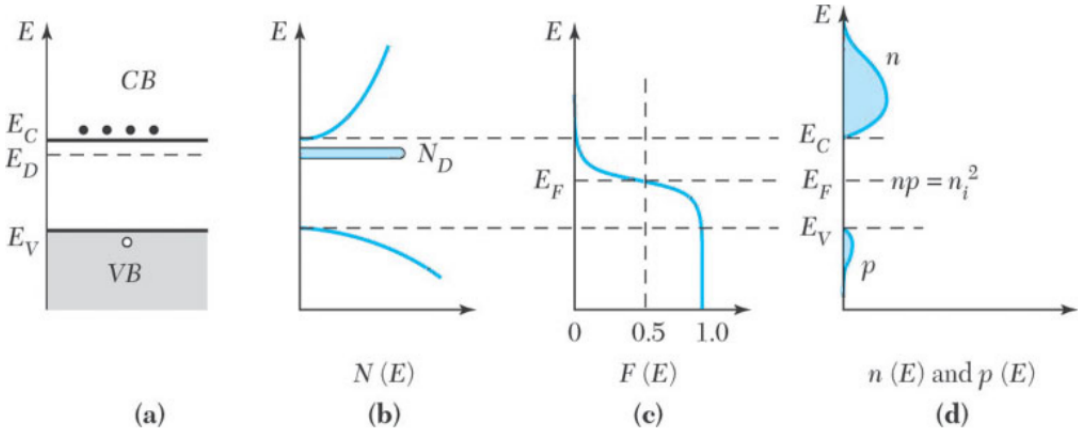

FIGURE 5.11: n-type semiconductor. (a) schematic band diagram, (b) density of states, (c) Fermi distribution function, (d) carrier concentration. Note that $np = n_i^2$ [19]. (Go back to Charge carrier transport)

5.1.4 Charge carrier transport

In this chapter we will consider phenomena that occur either through the application of an external electric field, in what is called drift, or because of non homogeneous distribution of movable charge carriers, in what is called diffusion. The process of creation and destruction of free charge carriers will also be considered here.

Movable charge carriers, electrons in the conduction band and holes in the valence band, are essentially free particles since they are not associated with a particular lattice place. Their mean kinetic energy is $3/2k_BT$, so that the mean velocity at room temperature is of the order of $10^7 cm/s$. They scatter on imperfections within the lattice, which are due to thermal vibrations, impurity atoms, and defects. A typical mean free path is $10^{-5} cm$ and a mean free time is $\tau_c \approx 10^{-12} s$.

5.1.4.1 Drift

In the field-free case, the average displacement of a movable charge-carrier due to random motion will be zero. However, if an electric field ε is present, the charge carriers will be accelerated in between random collisions in a direction determined by the electric field and a net average drift velocity ν will be different form 0:

$$\nu_n = -\frac{q\tau_c}{m_n}\varepsilon = -\mu_n\varepsilon \tag{5.9}$$

$$\nu_p = -\frac{q\tau_c}{m_p}\varepsilon = -\mu_p\varepsilon, \tag{5.10}$$

where q is the elemental charge, τ_c is the mean free time, m_n and m_p are the effective mass of the negative and positive charge carriers, respectively, and μ_n and μ_p are the electron and hole mobilities, respectively.

This relationship holds for fields small enough that the velocity change due to acceleration by the electric field is small with respect to the thermal velocity, and the mean collision time is independent of the electric field.

Scattering occurs on imperfections of the crystal lattice that are due to thermal vibrations and other sources such as crystal defects and doping atoms. Thus, mobilities μ_n and μ_p are dependent on temperature and doping concentration.

5.1.4.2 Diffusion

Consider now the situation of a non homogeneous distribution of free charge carriers in a semiconductor crystal and neglect all effects that are due to electric fields, i.e. the electric field due to non homogeneous charge-carrier distribution and/or doping concentration.

Although the net average displacement of an individual charge-carrier is zero in the absence of forces due to an electric field, the probability of carriers crossing from the side showing the higher concentration to that of the lower is larger than in the opposite case, as there are more particles having a chance to do so.

This effect, called diffusion, will result in a smoothing of the charge distribution. It is mathematically described by the diffusion equation:

$$F_n = -D_n \nabla n \tag{5.11}$$

$$F_p = -D_p \nabla p, \tag{5.12}$$

where F_n is the flux of electrons, D_n the diffusion constant, and ∇n the gradient of carrier concentration. And in the same manner for the p sub-indexed terms.

Combining the expressions for drift and diffusion one can express the current densities as follows:

$$J_n = q\mu_n n\varepsilon + qD_n \nabla n \tag{5.13}$$

$$J_p = q\mu_p p\varepsilon - qD_p \nabla p \tag{5.14}$$

Mobility and diffusion are related to each other by the Einstein equation:

$$D_{n,p} = \frac{k_B T}{q} \mu_{n,p} \tag{5.15}$$

5.1.5 Charge carrier generation and recombination

Free electrons and holes may be generated by the lifting of electrons from the valence band into the conduction band, thus creating simultaneously equal numbers of electrons and holes. This can be accomplished by various mechanisms such as thermal agitation, optical excitation, and ionisation by penetrating charged particles.

5.1.5.1 Thermal generation

Thermal generation of charge carriers usually has a detrimental effect in semiconductor radiation detectors because it leads to noise superimposed onto the signals. In some direct semiconductors the band-gap is small enough, compared with the thermal voltage at room temperature, for electrons to be excited directly from the valence to the conduction band. Therefore, semiconductors like GaAs have to be operated at low temperature. In others, like the indirect semiconductors Si and Ge, the probability of direct excitation at room temperature is extremely low. Here, the thermal excitation occurs in two steps, going through intermediate local states in the band-gap, as shown in Figure 5.12. These intermediate states are created by imperfections within the crystal and by impurities. Note that for indirect semiconductors (Si, Ge), the minimum energy needed for a band-to-band transition (electron–hole pair generation) is not simply given by the width of the band-gap. As the maximum of the valence band and the minimum of the conduction band are located at different momenta, as shown in Figure 5.6, additional momentum has to be transferred in the process.

5.1.5.2 EM radiation induced generation

This effect is the basis of photo detectors and solar cells. The schematics of the basic process is shown in Figure 5.13. A photon is absorbed and its energy is used to lift the electron from the valence band into the conduction band. If the photon energy is above the band-gap E_G, the electron will be lifted into one of the empty states of the conduction band, leaving behind a hole in the valence band. Electrons and holes will subsequently move towards the band-gap edges, thereby emitting energy in the form of phonons (lattice vibrations) or lower energy photons. Absorption of photons with

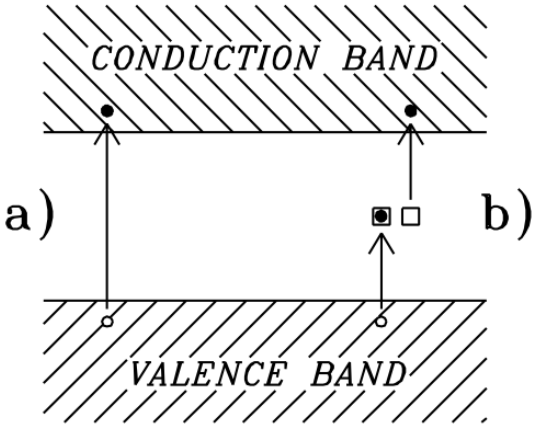

FIGURE 5.12: (a) direct and (b) indirect excitation of electrons [20]. (Go back to Thermal generation)

energies below E_G is in principle also possible if there are local states in the band-gap due to lattice imperfections.

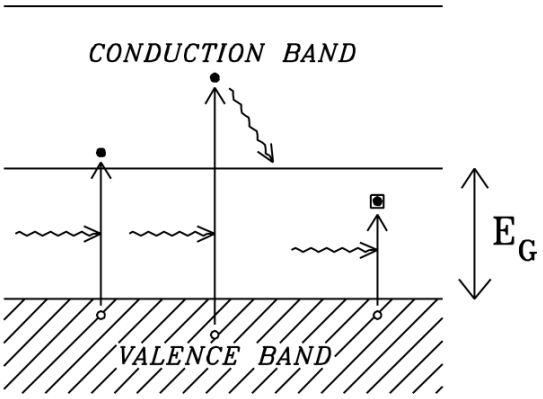

FIGURE 5.13: Generation of electrons and holes by absorption of photons of energies $E = E_G$, $E > E_G$ and $E < E_G$ [20]. (Go back to EM radiation induced generation)

5.1.5.3 Generation by charged particles

Charged particles traversing material lose part of their energy through elastic collisions with electrons. The Bethe-Bloch formula gives the rate of ionisation loss of a charged particle in matter, as shown below, including corrections for density and shell effects:

$$\frac{dE}{dx} = 2\pi N_0 r_e^2 m_e c^2 \rho \frac{Z}{A}\frac{z^2}{\beta^2}\left[\ln\left(\frac{2m_e\gamma^2 v^2 W_{max}}{I^2} - 2\beta^2 - \delta - 2\frac{C}{Z}\right)\right], \tag{5.16}$$

where x is the path length in g/cm^2, N_0 is Avogadro's number, $r_e = e^2/4\pi m_e c^2 cm$ is the classical electron radius, m_e is the electron mass, ρ is the density of the medium, Z is

the atomic number of the medium, A is the atomic weight of the medium, z is the charge of a traversing particle, $\beta = v/c$ is the velocity of a traversing particle, $\gamma = 1/(1-\beta^2)$, W_{max} is the maximum energy transfer in a single collision, I is the effective ionisation potential averaged over all electrons, δ is a density correction, and C is a shell correction.

The rate of energy loss as a function of particle energy for a charged pion is shown in Figure 5.14.

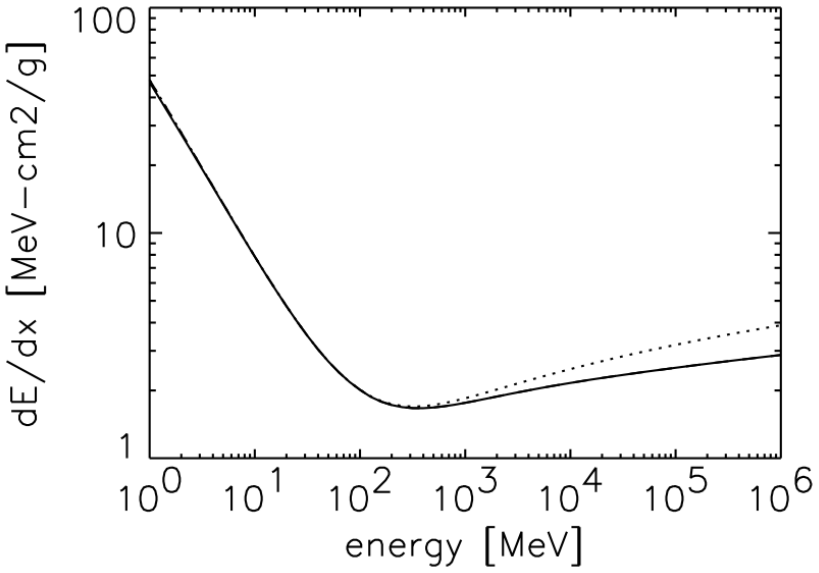

FIGURE 5.14: Rate of energy loss due to ionisation as a function of kinetic energy for a charged pion traversing Silicon, with (continuous line) and without (dotted line) density and shell corrections [20]. (Go back to Generation by charged particles)

Energy and velocity of the incident particle with mass M are related by relativistic kinematics as:

$$E = \gamma M c^2 = \frac{Mc^2}{\sqrt{1-\beta^2}}, \tag{5.17}$$

which for small velocities reduces to:

$$E_{kin} = E - Mc^2 = \frac{Mv^2}{2} \tag{5.18}$$

The maximum energy transfer produced by a head-on collision is given by:

$$W_{max} = \frac{2m_e c^2 \beta^2 \gamma^2}{1 + 2s\sqrt{1+\beta^2\gamma^2} + s^2}, \tag{5.19}$$

which for $M \ll m_e$ reduces to:

$$W_{max} \approx 2m_e c^2 \beta^2 \gamma^2. \tag{5.20}$$

In semiconductors, only part of the energy loss is used for the creation of electron–hole pairs. In silicon, the average energy used for the creation of an electron-hole pair is $3.6eV$, three times larger than the band-gap energy difference, of $1.12eV$. This is true for radiation energies that are large with respect to the band-gap.

5.1.5.4 Multiplication processes

If an electron or hole is created in, or moved into, a high-field region inside a semiconductor, it may be accelerated strongly enough in between collisions to acquire sufficient energy for the creation of a new electron–hole pair. An avalanche may thereafter develop and lead to device breakdown. Although charge multiplication may cause problems in poorly designed semiconductor devices leading to electrical breakdown, one can also make use of this effect in a controlled way for signal amplification, as in avalanche diodes, for example.

5.1.5.5 Recombination

Once an excess of minority charge carriers (e.g. electrons in p-type material) is created, it will take some time for the system to come back to thermal equilibrium. The transition back to equilibrium is due to recombination of the excess of the minority carriers (electrons) with the majority carriers (holes). For indirect band-gap semiconductors, such as silicon, a direct recombination process is very unlikely, because the electrons at the bottom of the conduction band have non-zero momentum with respect to the holes at the top of the valence band so it requires a large momentum transfer to the crystal lattice. Recombination occurs instead in two step processes, involving the capture and emission of electrons and holes into and out of the inter-gap generation and recombination centres, as shown in Figure 5.15, where the recombination center shown contains a single energy level that is neutral when not occupied by an electron and negative when occupied.

5.1.5.6 Lifetime

A very important parameter of detector-grade semiconductor material is the charge-carrier lifetime, both recombination and generation lifetime. These terms describe the transient behavior from a non-equilibrium charge distribution, obtained either by injection of additional carriers or by their removal, to a charge distribution in equilibrium condition.

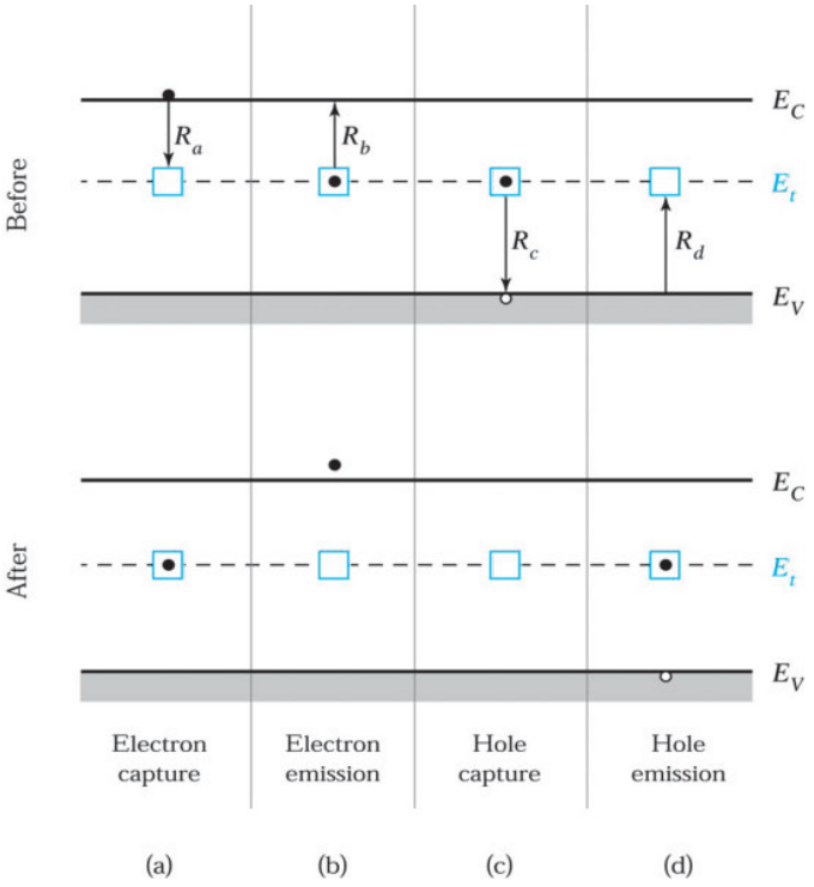

FIGURE 5.15: Indirect generation and recombination processes of (a) electron capture, (b) electron emission, (c) hole capture, and (d) hole emission at thermal equilibrium [19]. (Go back to Recombination)

Carrier recombination itself can take place by several mechanisms, the most important are direct band-to-band radiative recombination, deep level defect mediated or non-radiative band-to-band Auger recombination, as shown in Figure 5.16.

In most materials, one of the above processes will have a much higher probability of occurrence than the others and will largely determine the effective lifetime of the excited carriers, τ, given by:

$$\frac{1}{\tau} = \frac{1}{\tau_{rad}} + \frac{1}{\tau_{trap}} + \frac{1}{\tau_{Aug}}, \tag{5.21}$$

where τ_{rad}, τ_{trap}, τ_{Aug} are the radiative, trap, and Auger lifetimes, respectively. Auger recombination is usually more likely, since the Auger rate is proportional to the square of the doping density. For most semiconductors, however, especially those with indirect band-gap, short lifetimes are mainly due to impurities and defects, especially for those traps and defects that introduce energy levels near the middle of the band-gap.

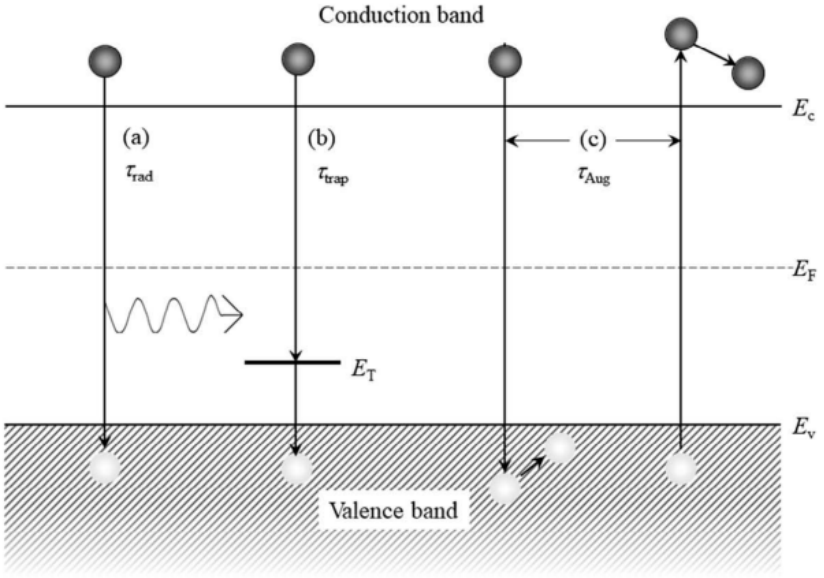

FIGURE 5.16: Schematic of carrier recombination mechanisms in semiconductors illustrating (a) radiative emission, (b) deep level trap mediated, and (c) non-radiative band-to-band Auger recombination [21]. (Go back to Lifetime)

The generation lifetime is closely related to the current generated in the Space Charge Regions (SCR) of electronic devices, such as a reversely biased diode.

5.1.6 The PN-junction

In this chapter we discuss the behaviour of a single-crystal semiconductor material built by joining together two extrinsic semiconductors of opposite doping, p-type and n-type, forming the well known *pn-junction*. The most important characteristic of p–n junctions is that they rectify, that is, they allow current to flow easily in only one direction. The current-voltage characteristics of a typical silicon pn-junction can be seen in Figure 5.17.

5.1.6.1 Thermal equilibrium

In Figure 5.18a we see two regions of p-type and n-type semiconductor materials that are uniformly doped and physically separated before the junction is formed. Note that the Fermi level E_F is near the valence band edge in the p-type material, and near the conduction band edge in the n-type material. While p-type material contains a large concentration of holes with few electrons, the opposite is true for n-type material.

When the p-type and n-type semiconductors are jointed together with no external forces acting upon them, as shown in Figure 5.18b, the device will move towards thermal equilibrium. For that, we will find that the large carrier concentration gradients found

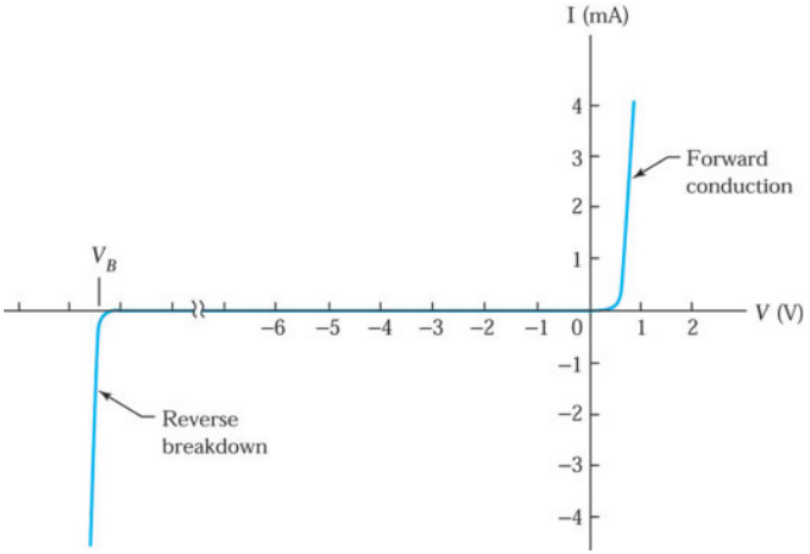

FIGURE 5.17: Current-voltage characteristics of a typical silicon pn-junction [19]. (Go back to The PN-junction)

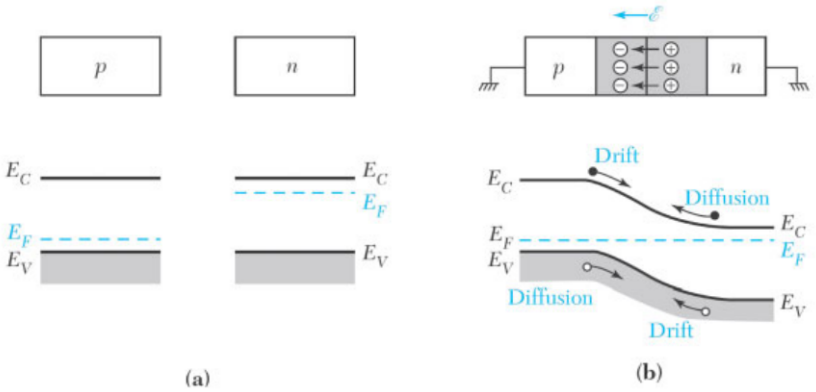

FIGURE 5.18: (a) uniformly doped p-type and n-type semiconductors before the junction is formed, (b) the electric field in the depletion region and the energy band diagram of a p–n junction in thermal equilibrium [19]. (Go back to Thermal equilibrium)

at the junction cause carrier diffusion. Holes from the p-side diffuse into the n-side, and electrons from the n-side diffuse into the p-side. As holes continue to leave the p-side, some of the negative acceptor ions near the junction, N_A^-, are left uncompensated because the acceptors are fixed in the semiconductor lattice, whereas the holes are mobile. Similarly, some of the positive donor ions near the junction, N_D^+, are left uncompensated as the electrons leave the n-side. Consequently, a negative space charge forms near the p-side of the junction and a positive space charge forms near the n-side. This space charge region creates an electric field that is directed from the positive charge towards the negative charge, as indicated in Figure 5.18b in the diagram at the top. The electric field is in the direction opposite to the diffusion current for each type of charge carrier. The bottom diagram in Figure 5.18b shows that the hole diffusion current flows from left to right, whereas the hole drift current due to the electric field flows from right to

left. The electron diffusion current also flows from left to right, whereas the electron drift current flows in the opposite direction. Note that because of their negative charge, electrons diffuse from right to left, opposite to the direction of electron current.

At thermal equilibrium at a given temperature, the individual electron and hole currents flowing across the junctions are identically zero. Thus, for each type of carrier the drift current due to the electric field must exactly cancel the diffusion current due to the concentration gradient, as shown below:

$$J_p = J_p(drift) + J_p(diffusion) \tag{5.22}$$

$$J_p = \mu_p p \frac{dE_F}{dx} \tag{5.23}$$

$$J_n = J_n(drift) + J_n(diffusion) \tag{5.24}$$

$$J_n = \mu_n n \frac{dE_F}{dx} \tag{5.25}$$

In the equilibrium, the diffusion potential, or built-in potential inside the space charge can be derived by the difference of the electric potential between the intrinsic levels in the n and p regions:

$$V_{bi} = \psi_n - \psi_p = \frac{k_B T}{q} \ln\left(\frac{N_A N_D}{n_i^2}\right), \tag{5.26}$$

where ψ_n and ψ_p are the electric potential in the n and p regions, respectively. With the requirement that the total charge in the space-charge region is zero, and considering the abrupt junction approximation, as shown in Figure 5.19, the width W of the total depletion layer can be derived from Equation 5.26:

$$W = \sqrt{\frac{2\epsilon\epsilon_0}{q}\left(\frac{N_A + N_D}{N_A N_D}\right) V_{bi}}, \tag{5.27}$$

where ϵ and ϵ_0 are the permittivity of the medium and of classical vacuum.

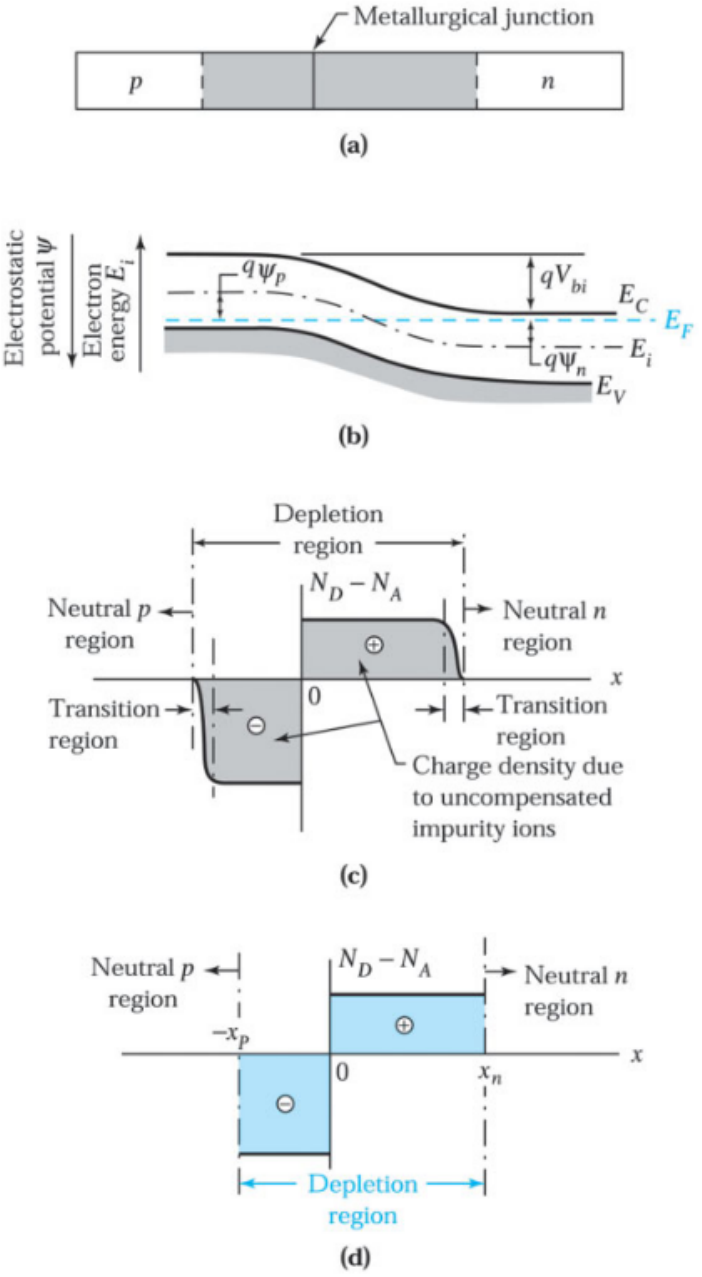

FIGURE 5.19: (a) A p–n junction with abrupt doping changes at the metallurgical junction, (b) energy band diagram of an abrupt junction at thermal equilibrium, (c) space charge distribution, (d) rectangular approximation of the space charge distribution [19]. (Go back to External voltage)

5.1.6.2 External voltage

If an external voltage is applied across the semiconductor, the system is not in thermal equilibrium anymore, and the previous equilibrium considerations can only be applied in an approximate way. Depending on the polarity, the external voltage increases or decreases the intrinsic potential barrier of the pn-junction.

If a positive voltage V_F is applied to the p-side with respect to the n-side, the p–n junction becomes forward biased, as shown in Figure 5.20b. The total electrostatic potential across the junction decreases by V_F. Thus, forward bias reduces the depletion layer width. Similarly, if a positive voltage V_R is applied to the n-side with respect to the p-side, as shown in Figure 5.20c, the p–n junction now becomes reverse-biased and the total electrostatic potential across the pn-junction increases by V_R. This time we see that reverse bias increases the depletion layer width.

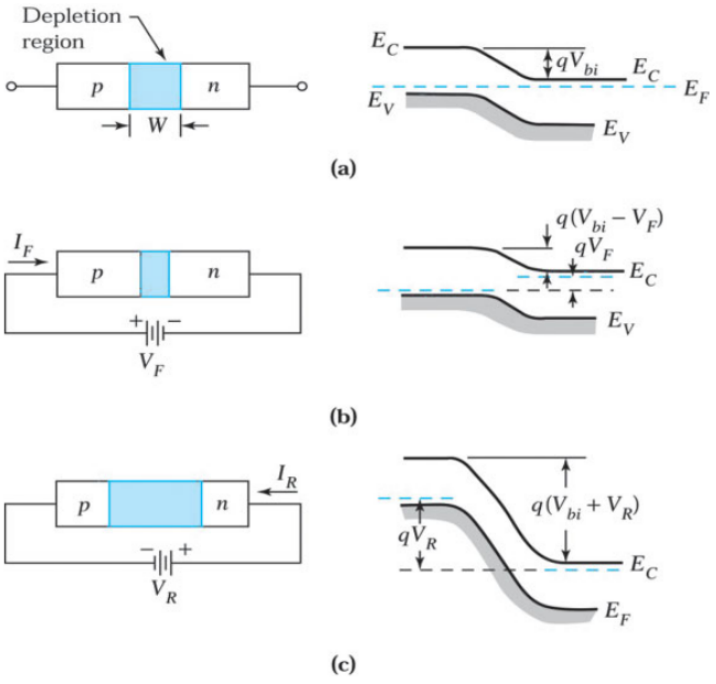

FIGURE 5.20: Schematic representations of depletion layer width and energy band diagrams of a p–n junction under various biasing conditions. (a) thermal-equilibrium condition. (b) forward-bias condition. (c) reverse-bias condition. [19]. (Go back to External voltage)

Similarly as in equation 5.27, the width W of the total depletion layer can be expressed as:

$$W = \sqrt{\frac{2\varepsilon\varepsilon_0}{q}\left(\frac{N_A + N_D}{N_A N_D}\right)(V_{bi} - V)}, \tag{5.28}$$

where V is the external voltage applied.

Then, considering the approximation of $V \ll V_{bi}$ and assuming that mobile carriers are negligible in the depletion region, bias voltage required to deplete the whole thickness $W = D$ of the device, the depletion voltage V_{dep}, can be obtained:

$$V_{dep} = \frac{qN_D D^2}{2\varepsilon\varepsilon_0} \tag{5.29}$$

The electric field configurations for under-depletion, full-depletion and over-depletion conditions are shown in Figure 5.21.

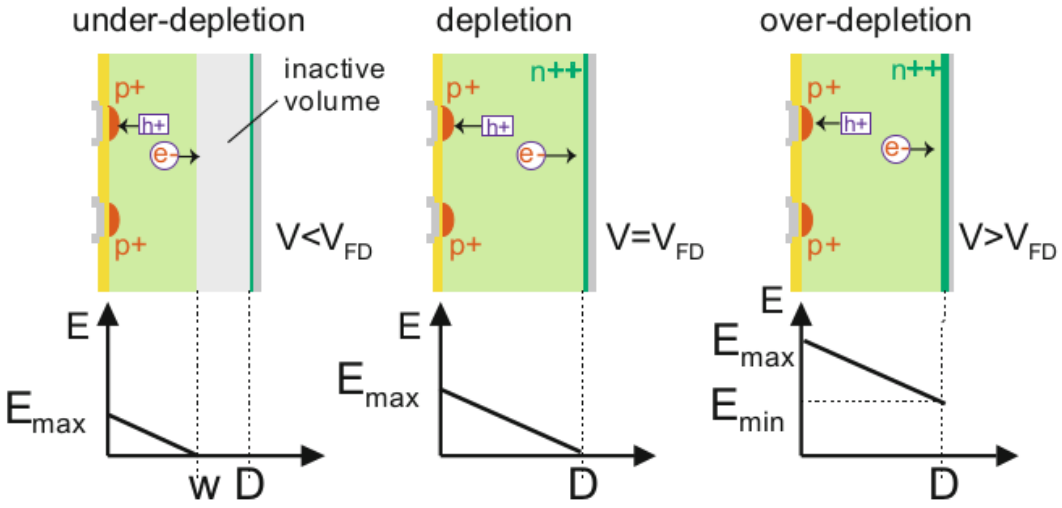

FIGURE 5.21: The field in the silicon bulk is linear, depleting a certain volume. The left scheme shows the under-depleted case with $V_{bias} < V_{FD}$, while the right scheme shows the over-depletion case $V_{bias} > V_{FD}$. The scheme in the middle depicts full depletion with $V_{bias} = V_{FD}$. The maximum field E_{max} is on the segmented side for $p^+ - n$, where the strips are on ground voltage potential and the backside is on high voltage potential [22]. (Go back to External voltage)

5.1.6.3 Dark current

In a reversed biased semiconductor, the total reverse current flowing through the device can be approximated by the sum of the diffusion current and the generation current. The dominant generation and recombination processes are those from electron and hole emissions through band-gap generation and recombination centres as the capture processes can be ignored as their rates are proportional to the concentration of free carriers, which is very small in the reverse-biased depletion region. This current is called dark current, or leakage current, and it is considered as an undesired effect.

Starting with the defect occupancy with electrons f_t, given by:

$$f_t = \frac{c_n n + e_p}{c_n n + e_n + c_p p + e_p}, \tag{5.30}$$

where c_n and c_p are the capture coefficients for electrons and holes, n and p are the electron and hole densities, and e_n and e_p are the emission rates for electrons and holes,

respectively. c_n is given by $c_n = \sigma_n \upsilon_{th,n}$, where $\upsilon_{th,n}$ is the thermal velocity for electrons. e_n is given by $e_n = c_n n_i \exp((E_t - E_i)/k_B T$, where n_i is the intrinsic carrier density, E_i the intrinsic Fermi level, and K_B the Boltzmann constant.

In the space charge region of a detector, the carrier densities are very low and can often be neglected simplifying Equation 5.30 to become:

$$f_t = \frac{e_p}{e_n + e_p} \tag{5.31}$$

Defect levels produce leakage current by the subsequent emission of electrons and holes, as in the transfer of electrons from the valence to the conduction band, for example. The generation rate G_t of a single defect type t in the case of neglectable free carrier concentrations is given by:

$$G_t = N_t f_t e_n = N_t (1 - f_t) e_p = N_t \frac{e_n e_p}{e_n + e_p}. \tag{5.32}$$

Summing over all defect types and taking into account the active volume of a sensor with depletion width w and area A, results into the total leakage current of the device:

$$I = q_e \omega A \sum_{defects} G_t, \tag{5.33}$$

where q_e is the elementary charge.

The current in a typical reverse biased semiconductor increases linearly with W until the device is fully depleted. For higher bias voltages, an eventual breakdown is observed, where the dark current increases abruptly. This can be caused by avalanche breakdown, charge multiplication, or by Zener breakdown.

5.2 Radiation damage

The intention of this chapter is to introduce the effects of radiation, at the microscopic and macroscopic level, on silicon sensors. The basics of radiation damage are contained in the so-called Hamburg Model [25].

Traversing particles interact with the material through ionising and Non-Ionising Energy Loss (NIEL) processes. Different mechanisms cause damage in the surface layer and in

the bulk of the silicon sensors, as well as in the read-out electronic systems, impacting different parameters. The three main effects brought by radiation are:

- Displacement of atoms from their positions in the lattice (bulk)
- Transient and long-term ionisation in insulator layers (surface)
- Formation of interface defects (surface)

5.2.1 Surface damage

The surface damage encloses all radiation induced damages in the SiO_2 (Silicon Dioxide) layer and in the $SiO_2 - Si$ interface. Therefore, AC-coupled sensors, and NMOS (N-type Metal-Oxide-Semiconductor) and PMOS (P-channel Metal-Oxide-Semiconductor) transistors in all kinds of electronics are specially susceptible to these effects. Damage in the surface of sensors is introduced by ionisation and in contrast to the situation in the silicon bulk, creation of electron–hole pairs is not fully reversible. Depending on the oxide quality, recombination varies between several percent and almost 100%. In addition to recombination, generated charge carriers can also be captured by existing defects with highly suppressed emissions, since the band-gap is much larger in oxide and nitride layers. The mobility of electrons in the oxide is several orders or magnitude higher than that of holes, leading to a fast separation of electron-holes pairs. Electrons drift to the metal electrode, while the holes drift to the $Si - SiO_2$ interface, as seen in Figure 5.22. In addition, the defect concentration is especially high at the interface due to lattice mismatch and dangling bonds. As a result, a high trap density makes positive static charges to accumulate at the interface. Negative charges are now attracted from the bulk side towards the interface and accumulate there, decreasing the inter-strip resistance and increasing polarisability, thus capacitance. As a second step, also negative traps are attracted towards the interface from the bulk side. The use of <100> silicon minimises the effect by reducing the number of dangling bonds. The field configuration with and without high oxide charge concentration is shown in Figure 5.23.

Summarizing, due to ionisation, insufficient recombination and subsequent trapping of holes at the $Si - SiO_2$ interface, the following macroscopic results deteriorate the sensor operational parameters:

- Increase of inter-strip capacitance, thus increasing noise
- Decrease of inter-strip resistance, thus increasing cross-talk
- Increase of flat-band voltage, as an indicator for oxide charge.

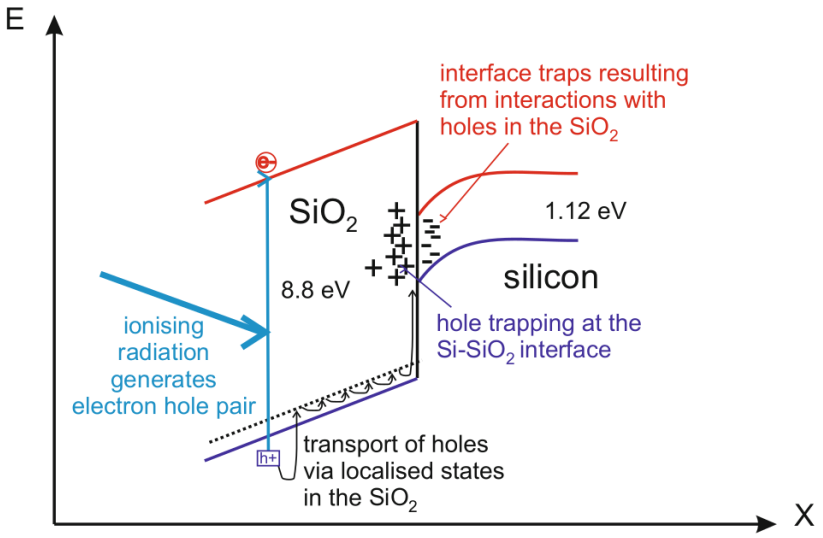

FIGURE 5.22: Surface damage in the $Si - SiO_2$ interface [22]. (Go back to Surface damage)

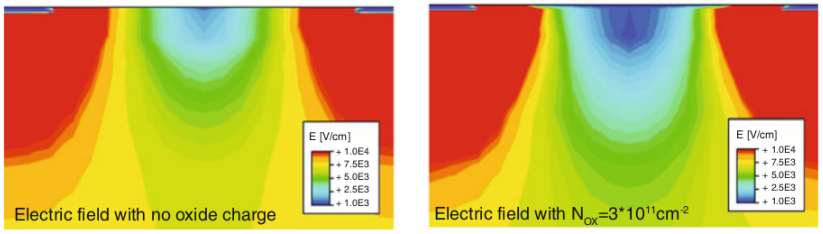

FIGURE 5.23: Inter-strip region fields with/without oxide charges. The additional charges do disturb the field distribution. The low-field region in the intermediate region of the strips (right picture) allows for negative charge carriers. These are increasing polarisability and thus capacitance and are decreasing the strip-by-strip insulation, which is completely defined by the field distribution [22]. (Go back to Surface damage)

Additionally, static charge centres have several other effects for NMOS and PMOS transistors in read-out chips:

- Threshold voltage shift of transistor V_{thr}
- Increased noise
- Increased leakage current

The main drawback of radiation damage in electronics is the increase of transistor threshold voltage V_{thr} and leakage current. The increased threshold voltage derives from the screening effect of the oxide charge concentration. On the other hand, the impact of non-ionising interactions on the surface is negligible as displacement of atoms in a highly irregular lattice is of no effect whatsoever.

5.2.2 Bulk damage

Electrons and hadrons with energies of the order of hundreds of keV are able to displace silicon atoms from the lattice. As the silicon structures used in HEP applications are based on mono-crystalline silicon, damage to the crystal structure leads to intermediate energy levels in the bulk, creating new generation and recombination centres.

To understand the behaviour of the depletion voltage, leakage current or charge trapping of in irradiated sensor it is necessary to consider the following:

- Damage to the lattice created by traversing particles
- Annealing processes

The following sections describe the microscopic and macroscopic changes in the silicon bulk of sensors with radiation and the subsequent changes with time, referred to as annealing. Annealing includes processes like diffusion, migration, break-up, re-configuration of defects. The introduced models describe the evolution of sensor macroscopic parameters like leakage current, depletion voltage and charge collection efficiency. A significant dependency on the type of radiation particle exists. In addition, for charged particles, a strong dependence is seen for different irradiated silicon materials, especially on their oxygen or carbon content.

5.2.2.1 Displacement damage

Traversing particles do not only ionise the lattice but also interact with the atomic bodies via the electromagnetic and strong forces, resulting in Non ionising Energy Loss (NIEL). Within this interaction, atoms are displaced and can lead to the creation of structures like interstitials I, vacancies V, di-vacancies V^2, and others, as depicted in Figure 5.24. All these defects result in a deformation of the lattice. In addition, diffusing Si atoms (interstitials I) or vacancies often form combinations with impurity atoms, like oxygen, phosphorus or carbon, again with different properties. All these lattice displacements create intermediate energy levels in the band-gap, changing the initial silicon properties. The main changes in the macroscopic parameters are:

- Increase of leakage current (dark current)
- Change of depletion voltage
- Decrease of charge collection efficiency

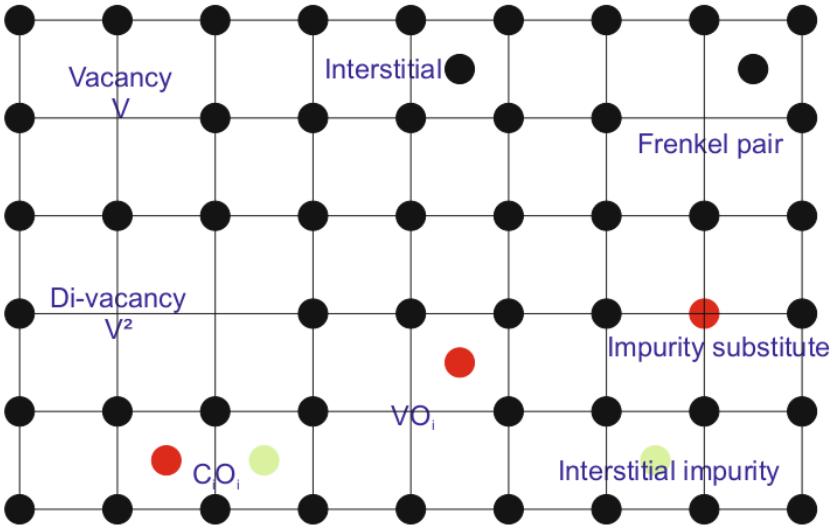

FIGURE 5.24: Atomic displacements in the lattice after collision with traversing particles. These vacancies, interstitials, and complex clusters create new levels in the energy scheme of the semiconductor and therefore change the elementary properties. As abbreviation, vacancies are labelled V, interstitials I, di-vacancies V^2. Impurities are labelled with their atomic sign, their index defines their position as substitute or interstitial, e.g. C_s or C_i [22]. (Go back to Displacement damage)

The basic important levels and their roles and macroscopic effects can be seen in Figure 5.25. The dependence of the damage on the type of particle and the energy can be seen in Figure 5.26, where the simulation of defect distribution and clustering show clear differences. $10MeV$ protons (left) produce a homogeneous vacancy distribution, while $24GeV$ protons (middle) leave a more clustered signature, and $1MeV$ neutrons produce even more clustered and isolated defects, as they interact only by the strong interaction.

Charged particles, via the Coulomb force, enhance small energy transfer and therefore local short distance defects, known as Frenkel pairs. Neutral particles, like neutrons, acting via the strong force, result mainly in long-range cluster defects. With enough energy, the initial primary knock on atom acts further on several additional lattice atoms. In the non-relativistic approach, the maximum transferred energy $E_{R,max}$ can be calculated in the case of recoil for a particle with mass m_p and kinetic energy E_p with:

$$E_{R,max} = 4E_p \frac{m_p m_{Si}}{(m_p + m_{Si})^2} \tag{5.34}$$

For electrons with energy E_e and mass m_e, higher kinetic energies are needed for lattice damage and $E_{R,max}$ can be calculated by the approximate relativistic relation:

$$E_{R,max} = 2E_e \frac{E_e + 2m_e c^2}{m_{Si} c^2}. \tag{5.35}$$

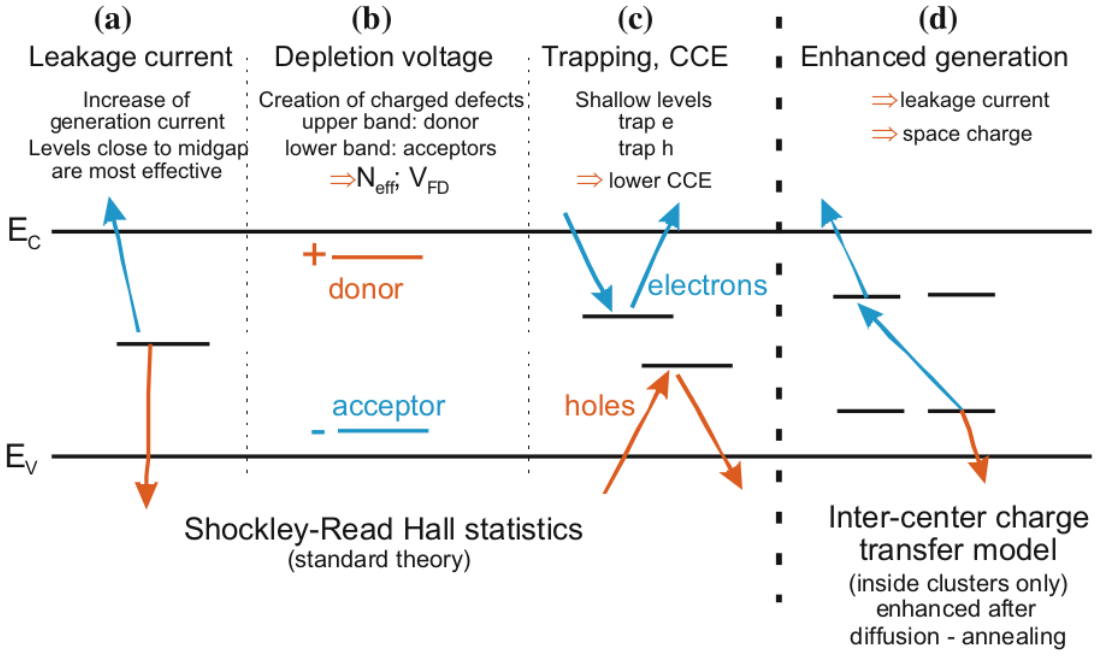

FIGURE 5.25: The different defect level locations and their effects. All relevant defect levels due to radiation are located in the forbidden energy gap. (a) mid-gap levels are mainly responsible for dark current generation. (b) donors in the upper half of the band-gap and acceptors in the lower half can contribute to the effective space charge. (c) deep levels, with de-trapping times larger than the detector electronics peaking time, are detrimental. Charge is lost, the signal decreases, and the charge collection efficiency is degraded. Defects can trap electrons or holes. (d) combinations of different defects into defect clusters additionally enhance the effects [22]. (Go back to Displacement damage)

Also, the energies needed to knock an atom from its original lattice place are clearly dependent on the binding forces and therefore on the material. In the case of silicon, the minimum energy needed to displace a single lattice atom (Frenkel pair production) is $E_{single\ defect} \approx 25eV$, while the one needed to produce a defect cluster is $E_{cluster} \approx 5keV$, as shown in Table 5.1.

Particle	$E_{single\ defect}$	$E_{cluster}$
neutron, proton	185 eV	35 KeV
electrons	225 eV	8 MeV
^{60}Co gammas	1 MeV	No cluster

TABLE 5.1: Minimum kinetic particle energies to create single point or cluster defects [22].

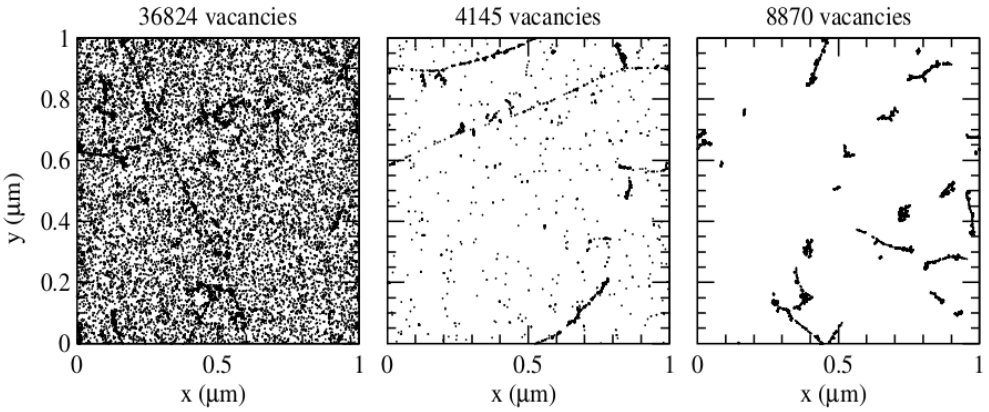

FIGURE 5.26: Simulation of defect formation with radiation. Initial distribution of vacancies produced by $10MeV$ protons (left), $23GeV/c$ protons (middle), and $1MeV$ neutrons (right). The plots are projected over $1\mu m$ depth (z) and correspond to a fluence of 10^{14} cm^{-2} [23]. (Go back to NIEL normalisation)

5.2.2.2 NIEL normalisation

The Non Ionising Energy Loss (NIEL) hypothesis allows a first-order normalisation of radiation damage with respect to different particles with different energies and assumes that radiation damage effects scale linearly with NIEL. According to the NIEL hypothesis, the damage manifestation depends only on energy transferred in collisions regardless of particle energy and type, and irrespective of the distribution of the primary displacements over energy and space, but they scale linear with NIEL. In that way, the damage produced by different particles and with different energies should be scalable and their dependence can be absorbed into the normalised value of the total fluence of the radiation that caused the damage effects.

Then the displacement damage $D(E)$ can be calculated by:

$$D(E) = \sum_i \sigma_i(E_{kin}) \int_0^{E_{R,max}} f_i(E_{kin}, E_R) P(E_R)\, dE_R, \tag{5.36}$$

where all possible interactions are summed up. σ_i is the cross-section of the process and $f_i(E,T)$ is the probability of having a collision of a particle with E_{kin} transferring a recoil energy of E_R. $P(E_R)$ is the Lindhard partition function, describing the fraction of energy going into silicon atom displacement (e.g. $P(E_R) \approx 43\%$ for $1MeV$ neutrons [23]). The resulting displacement functions $D(E)$ are plotted in Figure 5.27. As standard, the $1MeV$ neutron equivalent fluence $[n_{1MeV/cm^2}]$ is used and abbreviated with Φ_{eq}, corresponding to $D_{neutron}(1MeV)/cm^2 = 95MeVmb/cm^2$ [54].

It is therefore possible to scale radiation damage from different particles and different energies by a simple numerical factor, called hardness factor K, to make comparisons

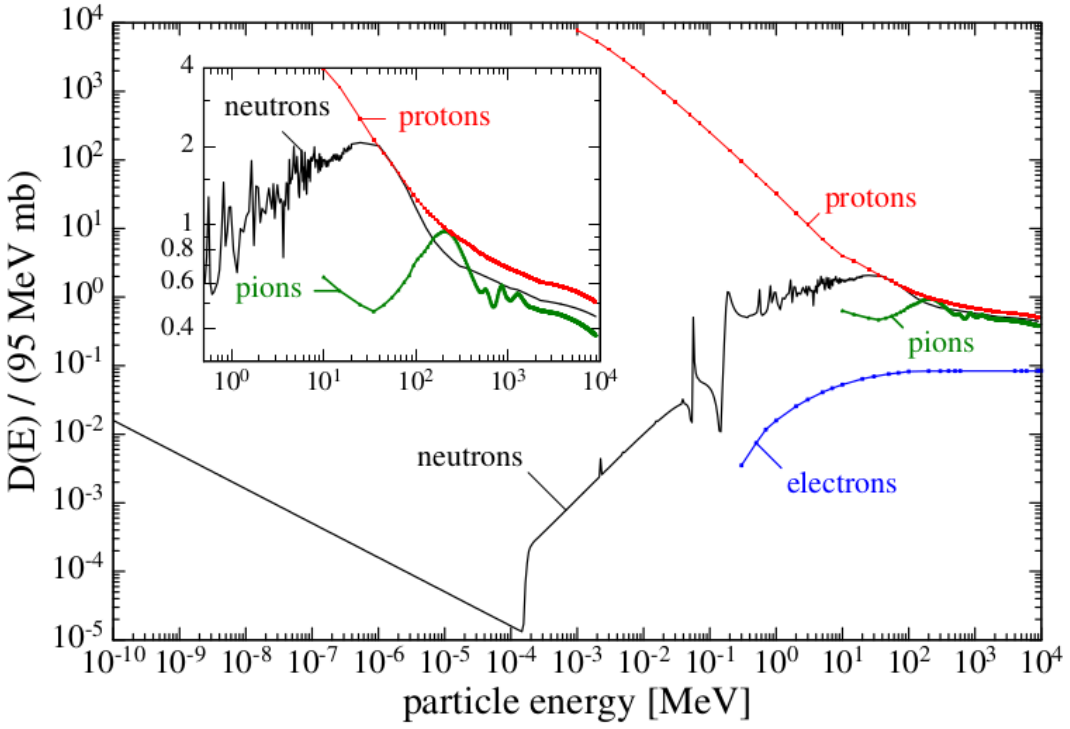

FIGURE 5.27: Non-ionising energy loss (NIEL) cross-sections normalised to $95MeVmb$ [23], data from [24]. (Go back to NIEL normalisation)

possible. k is defined as the ratio of the individual damage particle factor for a given energy and $1MeV$ neutrons as:

$$k = \frac{\int D(E)\phi(E)\,dE}{95MeVmb \cdot \phi} = \frac{\Phi_{eq}}{\phi} \tag{5.37}$$

where $\phi = \int \phi(E)\,dE$ is the irradiation fluence. The 1 MeV neutron equivalent fluence Φ_{eq} is then calculated by:

$$\Phi_{eq} = k\phi = k \int \phi(E)\,dE; \quad \left[\Phi_{eq} = n_{1MeV/cm^2}\right] \tag{5.38}$$

5.2.2.3 Annealing - diffusion of defects

Interstitials I and vacancies V have high mobility at temperatures $T > 150K$ and there is a possibility of forming the following structures:

- Frenkel pair recombination ($I + V \rightarrow$ Si)
- Multi-vacancy and multi-interstitial combination (e.g. $V + V \rightarrow V_2$)

- Combination of more complex defects (e.g. $C_i + O_i \rightarrow C_iO_i$ or $V + P \rightarrow VP$),

where the former types are short-range and very mobile processes and therefore happen with a shorter time constant, while the latter happens with a longer time constant. The whole process is called annealing, with a beneficial part reducing the damage and a reverse annealing part degrading macroscopic sensor properties. Some parts are stable and do not evolve with time. The diffusion processes are naturally temperature dependent and some effects, like depletion voltage evolution, can even be effectively frozen out at temperatures below $0°C$. In addition, different levels in the energy band behave differently with respect to time constants and temperatures. The effects of annealing on defect distribution can be seen in Figure 5.28, where the plots correspond exactly to the initial vacancy concentration of the simulation data shown in Figure 5.26, and have the same fluence and depth scaling. Clear signatures of defect redistribution can be observed due to the effects of annealing.

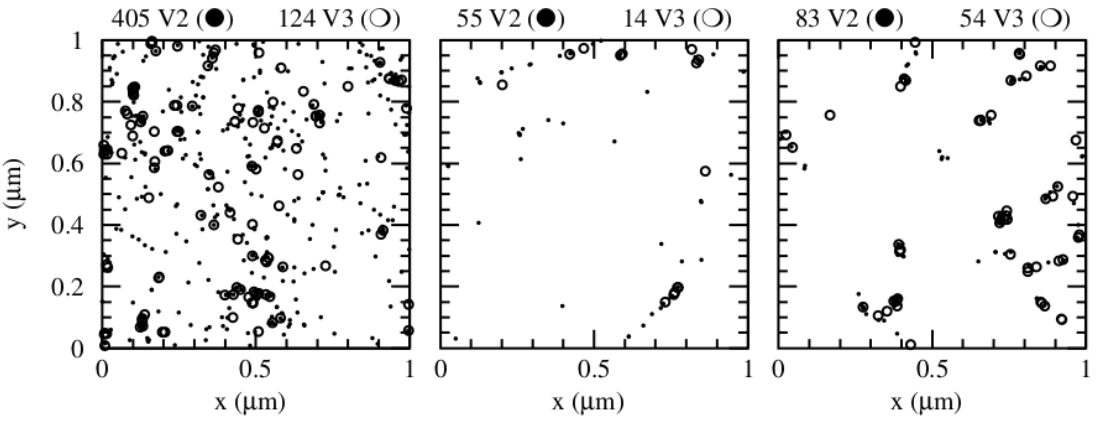

FIGURE 5.28: Simulation of defect annealing. Final distribution of defects after $10MeV$ proton (left), $24GeV/c$ proton (middle) and $1MeV$ neutron (right) irradiation, and annealing. The plots correspond exactly to the initial vacancy concentration of Figure 5.26 and have the same fluence and depth scaling. [23]. (Go back to Annealing - diffusion of defects)

To summarize, the macroscopic changes induced by annealing are highly temperature dependent, frozen out at sub-zero temperatures and are dominant at room temperature and above. Leakage current, charge collection efficiency, and depletion voltages evolve with time in the following way and will be discussed thoroughly later:

- leakage current always decreases
- trapping probability decreases for holes and increases for electrons
- acceptor levels first decay in the beneficial phase and increase later in the reverse annealing phase. In a n-type bulk, this leads to an increase/decrease of depletion voltage before and decrease/increase after type inversion.

The recipe is to benefit from the beneficial annealing for voltage and current and avoid the reverse annealing phase to stay in applicable bias voltage levels.

5.3 Radiation effects on detector systems

The various sensor types employed in the LHC experiments suffer from performance degradation induced by radiation. This originates mostly from displacement damage effects occurring in the silicon bulk of the devices. In this section, we present a general overview of displacement damage effects with relevance for all silicon sensor types and in the framework of the Shockley–Read–Hall (SRH) theory, as seen in [58]. As well, a brief section about damage on electronic devices is included.

5.3.1 Impact of defects on silicon sensors

As mentioned before, radiation induced electrically active defects generate energy levels in the silicon band-gap and affect the overall performance of detectors. Theoretically, the impact of each defect can be calculated if the capture cross sections for holes and electrons, their position in the band-gap, the defect type (acceptor or donor), and the concentration of the defects are known. An in-depth analysis can be found in [59].

The main macroscopic parameters affected will be treated below.

5.3.1.1 Leakage current

The leakage current, or dark current, is mainly produced by defect levels close to the middle of the band-gap and follows the NIEL hypothesis [60].

The increase of leakage current leads to increase of noise in the amplifiers and to an increase of power consumption. As the leakage current depends exponentially on the temperature, cooling is a very effective means to mitigate the detrimental effects.

Fluence dependence

After exposure to highly energetic particles, following the NIEL hypothesis, the radiation induced increase of the leakage current is proportional to the particle fluence and independent of the type, resistivity, and impurity content of the used silicon material. The increase of leakage current as a function of the irradiated fluence for various silicon sensor is shown in Figure 5.29.

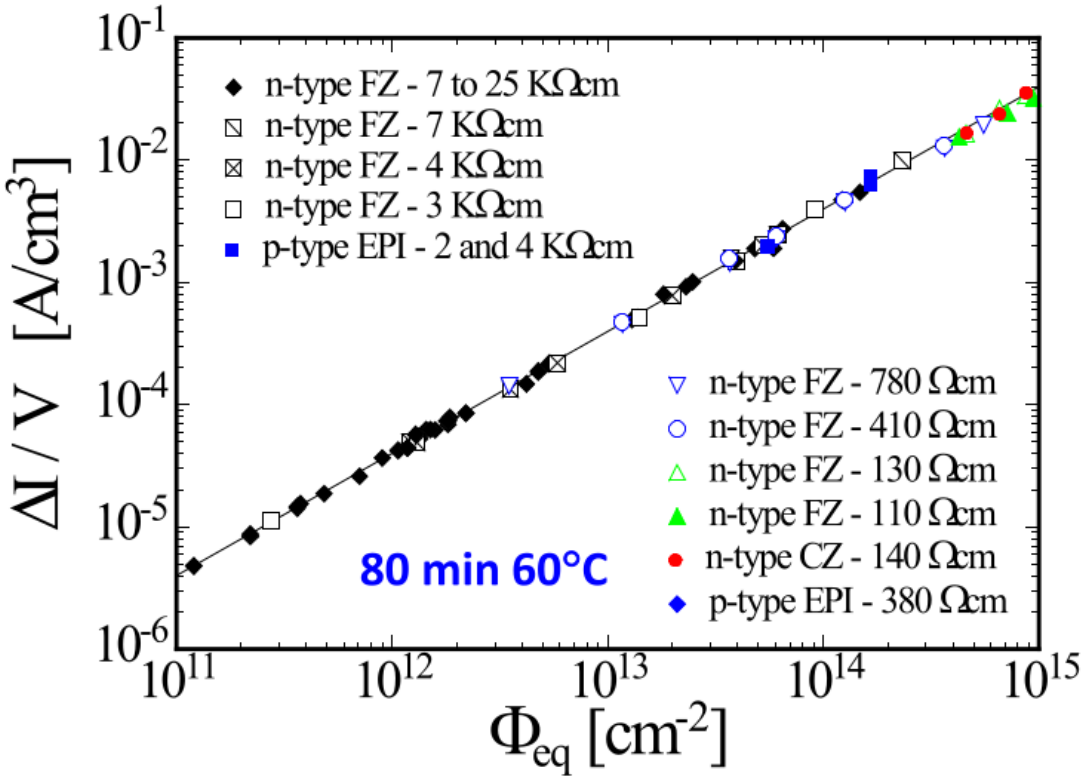

FIGURE 5.29: Radiation induced leakage current increase as function of particle fluence for various silicon detectors made from silicon materials produced by various process technologies with different resistivities and conduction type. The current was measured after annealing for $80min$ at $60°C$ and is normalised to the current measured at $20°C$ [25]. (Go back to Fluence dependence)

The proportionality factor is called current related damage factor, α, and is defined as:

$$\alpha = \frac{\Delta I_{leak}}{V \Phi_{eq}}, \tag{5.39}$$

where ΔI is the leakage current increase caused by irradiation, V the volume contributing to the current, and Φ_{eq} the 1 MeV neutron equivalent particle fluence.

Temperature dependence and scaling

The temperature dependence of the leakage current is dominated by the position of the energy levels in the band-gap, their cross-sections, their concentrations, and the temperature dependence of the band-gap itself. The most efficient generation centres are the ones at the intrinsic energy level.

Again, following the NEIL hypothesis, α (Equation 5.39) can be expressed as a function of time and temperature, only:

$$\alpha = \alpha(t, T), \tag{5.40}$$

therefore, being able to express ΔI_{leak} as a function time and temperature:

$$\Delta I_{leak}(t, T) = \alpha(t, T)\ \Phi_{eq}\ \mathrm{V}. \tag{5.41}$$

The dependence of I_{leak} on the temperature has the following shape:

$$I(T) \propto T^2 \exp\left(\frac{-E_{eff}}{2k_B T}\right), \tag{5.42}$$

where T is the measurement temperature, and E_{eff} is the effective band-gap energy in silicon.

Such that the leakage current on a sensor irradiated at a given $1MeV$ equivalent fluence Φ_{eq} and measured at a specific temperature can be scaled to a different temperature in order to compare data from different measuring temperatures. As with the following parametrization:

$$\frac{I(T)}{I(T_0)} = \left(\frac{T}{T_0}\right)^2 \exp\left[\frac{E_{eff}}{2k_B}\left(\frac{1}{T} - \frac{1}{T_0}\right)\right], \tag{5.43}$$

where $I(T_0)$ is the current measured at T_0, $I(T)$ is the current scaled to the target temperature T, E_{eff} is the effective band-gap energy in silicon, and k_B is the Boltzmann constant [28].

In a recent work [61], experimental results obtained from different irradiated silicon sensors were evaluated and obtained $E_{eff} = 1.214 \pm 0.014\ eV$ from a fit to Equation 6.2.3.

In practical terms, the temperature scaling of the leakage current translates into a reduction of the leakage current by around $8 - 10\%$ per degree centigrade in the temperature range from RT to $-20°C$.

Annealing effects and parametrization

The annealing behaviour of the current related damage factor α after irradiation can be seen in Figure 5.30 for various annealing temperatures ranging from $21 - 106°C$, where α is continuously decreasing with increasing annealing time.

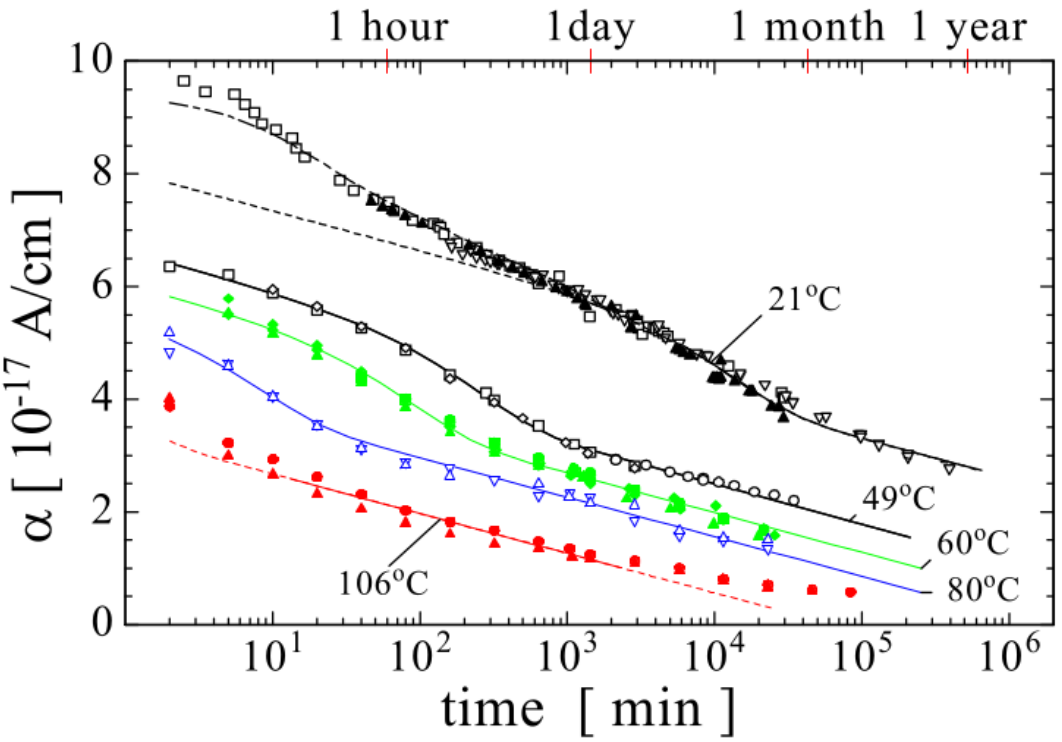

FIGURE 5.30: Current related damage factor α as a function of accumulated annealing time at different temperatures. Solid lines are fits to data [26]. (Go back to Annealing effects and parametrization)

The annealing temperature is the temperature at which the samples are stored or heated to accelerate the defect diffusion in the silicon lattice. This temperature shall not be confused with the measurement temperature of the leakage current, which, in the given example, is $20°C$. A parametrization of the data with an exponential and logarithmic term is proposed for the evolution of α:

$$\alpha(t) = \alpha_0 + \alpha_1 \cdot e^{-\frac{t}{\tau_1}} + \alpha_2 \cdot \ln\left(\frac{t}{t_0}\right), \tag{5.44}$$

where t_0, τ_1, α_0, α_1, and α_2 are constant coefficients. The complete parameter set and a discussion on their physical meaning can be found in [60], [26].

5.3.1.2 Depletion voltage - effective space charge - effective doping concentration

In undamaged sensors, the doping of the bulk, with Phosphorus or Boron, constitutes the effective space charge formed by the excess of free electron and holes in the lattice. Radiation induced changes to the effective space charge lead to a change of the distribution of the electric field in the volume of the device, normally diverting from linearity. This

shifts the depletion voltage to lower or higher values. In the latter case, higher operation voltages might need to be applied to establish an electric field throughout the full sensor volume in order to avoid under-depletion (loss of active volume), and therefore, signal. If sufficiently high voltage cannot be applied, or breakdown of the sensor is at risk, sensors will have to be operated in under-depletion conditions and this in turn will lead to a loss in signal amplitude. Non homogeneous distribution of effective space charge can also lead to double junction effects or the shift of the highest electric field towards other regions. Furthermore, high local fields can lead to impact ionisation effects or breakdown. It has been shown that the change of the space charge in silicon is strongly material dependent (e.g. oxygen content) and depending on the particle type used for the irradiation experiment (e.g. neutron vs. proton damage). This implies that this damage effect does not directly scale with NIEL in all scenarios and can be altered or mitigated by defect engineering approaches (e.g. change of impurity content). Defects can contribute with positive charge (donors) or negative charge (acceptors) to the space charge and thus alter the electric field distribution and the depletion voltage of devices. Neglecting free carriers, the effective space charge N_{eff} is then given by the sum of all positively charged donors N_D and all negatively charged acceptors N_A as:

$$N_{eff} = \sum_{donors} (1 - f_t) N_t - \sum_{acceptors} f_t N_t, \tag{5.45}$$

where the index t is running over all donor and acceptor like defect types t with concentration N_t.

The radiation induced defects lead to a change in the effective space charge N_{eff} that is reflected in a change of the depletion voltage V_{dep} of silicon detectors. The depletion voltage V_{dep} is given by:

$$V_{dep} = \frac{q_e \cdot |N_{eff}| \cdot d^2}{2\epsilon\epsilon_0}, \tag{5.46}$$

where d is the thickness of the device, q_e the elementary charge, ϵ the relative permittivity of silicon, and ϵ_0 the vacuum permittivity. It shall be noted that Equation 5.46 assumes a constant space charge over the volume of the damaged detector, which is not always the case, so it should be understood that the parametrizations considered give precise values for the prediction of the depletion voltage while obtaining N_{eff} back using Equation 5.46 might incur in systematic errors. It shall be mentioned that, in highly irradiated detectors, contrary to undamaged detectors, the space charge is no longer identical to the free carrier concentration in thermal equilibrium so results of characterisation methods

determining the free carrier density are therefore not easily correlated with the space charge determined from full depletion voltage analysis.

Fluence dependence

Irradiation of silicon sensors results, in most of the cases, in the formation of negative space charge which implies a modification of the effective space charge, leading to a change of the depletion voltage.

The effective space charge as a function of accumulated particle fluence of an n-type sensor is shown in Figure 5.31. Before irradiation the sensor was of high resistivity n-type (phosphorus doped) base material resulting in a positive space charge of around 10^{11} cm^{-3} . Irradiation of the sensor results in the formation of negative space charge, which compensates the initial positive space charge. With increasing particle fluence, the net space charge decreases and reaches very low values corresponding to almost intrinsic silicon. This point is called type inversion or Space Charge Sign Inversion (SCSI), as the space charge sign changes from positive to negative. Increasing the particle fluence beyond the SCSI point leads to more and more negative space charge values. The depletion voltage rises accordingly and eventually reaches values that cannot be applied to the detector any more without causing breakdown. The applied voltage will have to be kept below the depletion voltage and the detector is operated under-depleted. For high resistivity p-type sensors no "type inversion" is usually observed as the initial space charge is already negative before irradiation. However, in some cases, after neutron and after charged hadron irradiation, silicon materials have shown different behaviours [60].

Annealing effects and parametrization

The effective doping concentration after irradiation changes with annealing and can be accelerated at higher temperatures and decelerated or stopped when reaching low temperatures. In Figure 5.32, a typical annealing behaviour after high fluence irradiation can be seen.

The change of the effective doping concentration with irradiation ΔN_{eff} is given by:

$$\Delta N_{eff} = N_{eff,0} - N_{eff}(t), \tag{5.47}$$

where $N_{eff,0}$ is the value before irradiation and $N_{eff}(t)$ is the value after irradiation. In Figure 5.32, ΔN_{eff} is positive such that the radiation induced change of N_{eff} has a negative sign, implying that the overall produced space charge due to radiation is a negative one, in accordance to what can be seen in Figure 5.31.

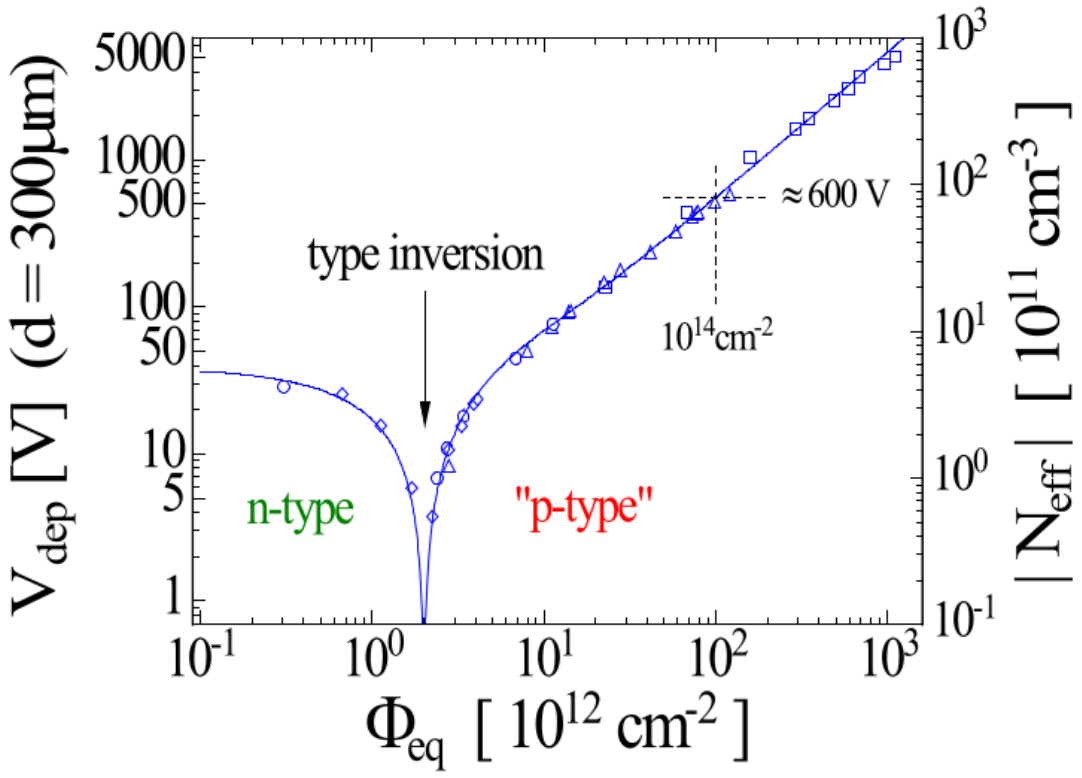

FIGURE 5.31: Effective doping concentration (depletion voltage) as a function of particle fluence for a standard FZ n-type silicon sensor [27]. (Go back to Fluence dependence)

The time dependence of N_{eff} can be parametrized as:

$$\Delta N_{eff}(t) = N_A(t) + N_C + N_Y(t), \tag{5.48}$$

where N_C is the stable damage component, which does not change with time after irradiation, N_A is the short term or beneficial annealing component, and N_Y is the reverse annealing component. They are parametrized as:

$$N_A(t) = g_a \ \Phi_{eq} \exp\left(\frac{-t}{\tau_a}\right) \tag{5.49}$$

$$N_C = N_{C,0}(1 - \exp(-c \ \Phi_{eq})) + g_c \ \Phi_{eq} \tag{5.50}$$

$$N_Y(t) = g_y \ \Phi_{eq}\left(1 - \exp\left(\frac{-t}{\tau_y}\right)\right), \tag{5.51}$$

where $N_{C,0}$ represents the fact that often an incomplete doping removal is observed (i.e., $N_{C,0}$ represents only a fraction of the initial doping concentration), c is the removal coefficient, and g_a, g_c, and g_y are the introduction rates for the space charge defined as the beneficial annealing, the stable damage, and the reverse annealing, respectively. The temperature dependence of the time constants for the beneficial τ_a, and the reverse

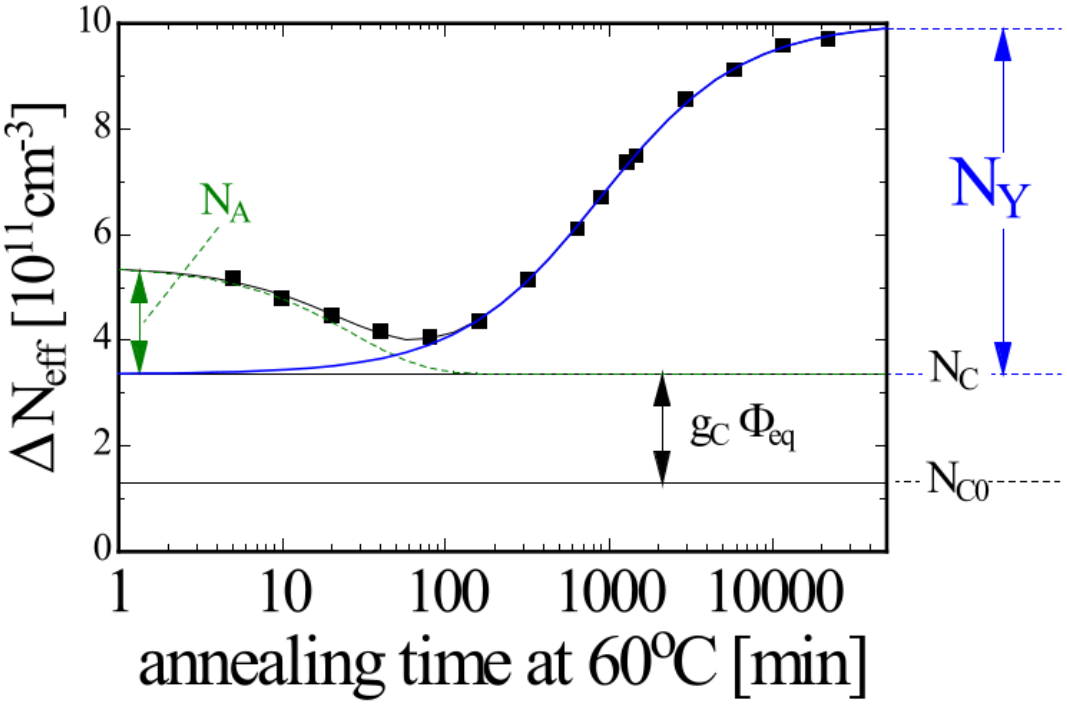

FIGURE 5.32: Evolution of the effective doping concentration as a function of annealing time. The data shown here were taken at room temperature while the annealing took place at 60°C [25]. (Go back to Fluence dependence)

annealing τ_y has been found to follow an Arrhenius equation with activation energies of 1.09 eV and 1.33 eV.

Donor removal

By the term donor removal we understand the transformation of electrically active shallow donors (usually phosphorus) into defect complexes that no longer have the properties of those shallow dopants. The positive space charge contributed by the shallow dopants is therefore lost and the overall space charge is altered.

5.3.1.3 Charge collection efficiency - charge carrier trapping

As seen before, charge carriers generated by ionising particles or photons in the space charge region travel towards the electrodes accelerated by the electric field inside the sensor and constitute the sensor signal. Defect levels can act as charge carrier traps capturing carriers, and if the release (detrapping) time of the charge carriers is long compared to the collection time of the system, or if the concentration of defects (trapping centres) is very high, charge is lost and the overall signal of the sensor is reduced, decreasing the charge collection efficiency. Mitigation of this problem is possible by

achieving faster collection times, for example. In segmented sensors, the collection of electrons instead of holes at the sensing electrodes can be an advantage due to the higher mobility of the first. The trapping is characterised by a trapping time τ_e (inverse capture rate) for electrons and τ_h for holes:

$$\frac{1}{\tau_e} = c_n(1 - f_t)N_t \tag{5.52}$$

$$\frac{1}{\tau_h} = c_p f_t N_t, \tag{5.53}$$

Summing over all defects contributing to the trapping results into the effective trapping times τ_f and τ_h, for electrons and holes, respectively:

$$\frac{1}{\tau_{eff,e}} = \sum_{defects} c_{(n,t)}(1 - f_t)N_t \tag{5.54}$$

$$\frac{1}{\tau_{eff,h}} = \sum_{defects} c_{(p,t)} f_t N_t \tag{5.55}$$

Fluence dependence

With increasing particle fluence, the number of trapping centres increases and more charge carriers get trapped during signal formation, which leads to a decrease of the charge collection efficiency. The effective trapping time τ_{eff} can be used to describe this effect, assuming that the loss of charge depends only on the charge carrier transport time inside the sensor:

$$Q(t) = Q_0 \exp\left(\frac{-t}{\tau_{eff}}\right). \tag{5.56}$$

The effective trapping time can be separately measured for electrons and holes, as seen in Figure 5.33. A linear dependence of the inverse effective trapping time on the particle fluence is observed and can be described as:

$$\frac{1}{\tau_{eff}} = \frac{1}{\tau_{eff,0}} + \beta\Phi_{eq}, \tag{5.57}$$

where β is the effective trapping damage constant and $\tau_{eff,0}$ the effective carrier lifetime before irradiation.

Annealing effects and parametrization

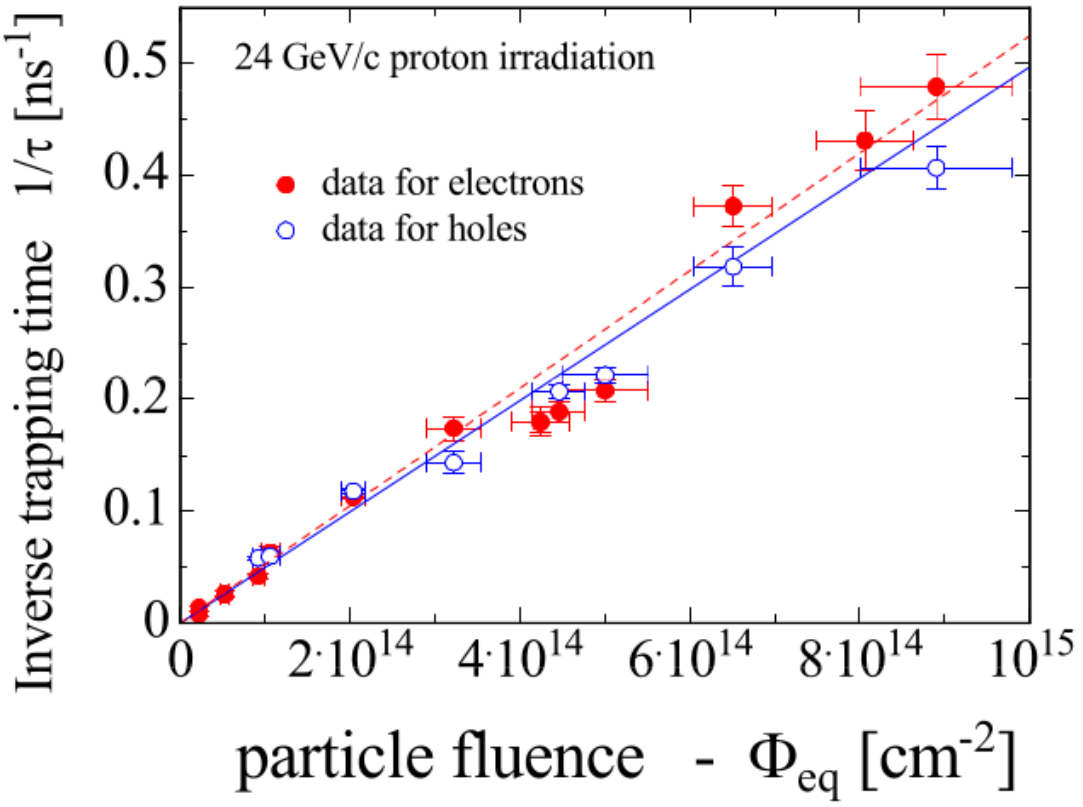

FIGURE 5.33: Inverse trapping time as function of particle fluence as measured at $0°C$ after an annealing of 30 to 60 min at $60°C$ [28], data from [29]. (Go back to Fluence dependence)

As for the leakage current and the depletion voltage, the effective trapping damage constant depends on the annealing of the sensor after irradiation, as shown in the following parametrization for holes and electrons:

$$\beta(t) = \beta_0 \exp\left(\frac{-t}{\tau_a}\right) + \beta_\infty\left(1 - \exp\left(\frac{-t}{\tau_a}\right)\right), \tag{5.58}$$

where β_0 and β_∞ denote the trapping rates β at the beginning and end of the annealing process, respectively, which are governed by the time constant τ_a. While for electrons, a reduction of trapping with annealing time has been observed, decreasing $1/\tau_{eff,e}$, for holes, the opposite behaviour is observed, as seen in Figure 5.34.

5.3.2 Impact on electronics

Radiation affects the performance of microelectronic devices in several ways and it is of great importance to understand how this happens in the LHC experiment. With such knowledge, electronics can be designed, tested and qualified to meet the goals.

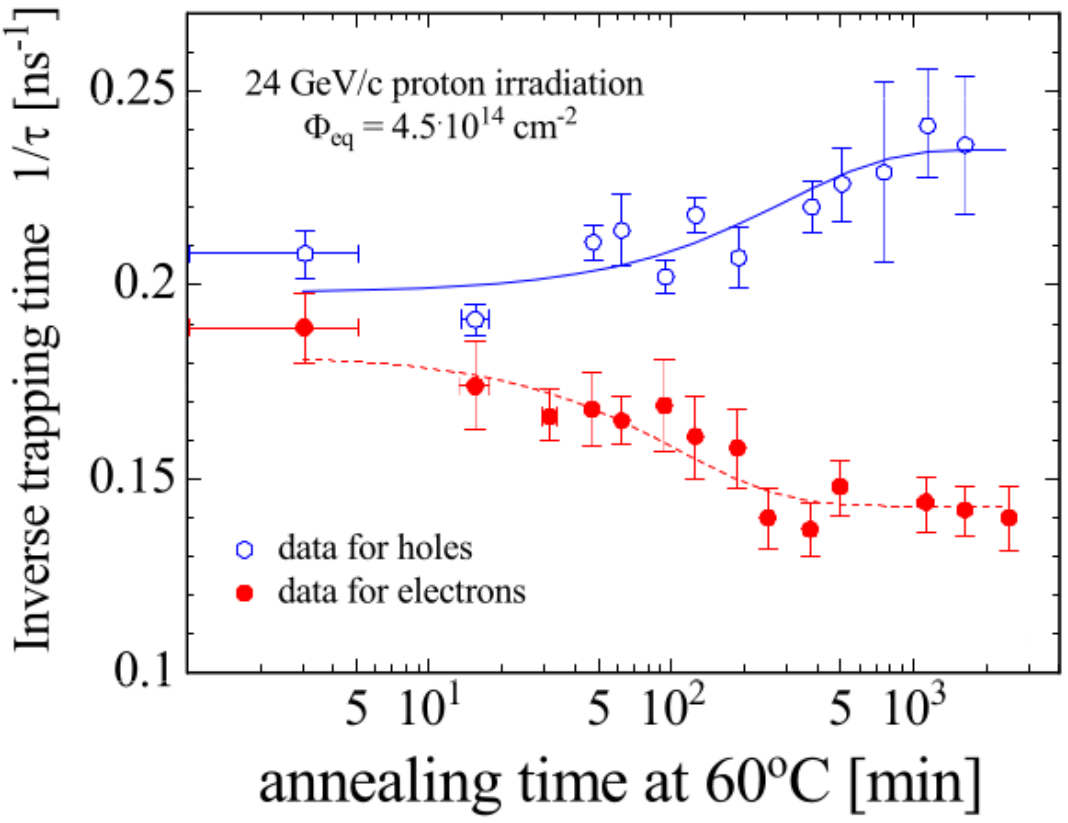

FIGURE 5.34: Evolution of the inverse trapping time as function of annealing time at 60°C [28], data from [29]. (Go back to Annealing effects and parametrization)

Furthermore, in the area of commercial-off-the-shelf electronics, a good understanding is needed in order to assess how they will perform in radiation environments as it is an application for which they were not necessarily designed for. CMOS and bipolar electronics performance in radiation environments can depend strongly on the particle type, the particle energy, the dose rate, the temperature, and the bias voltage. As it is unfeasible to recreate all these conditions in test facilities, the challenge is to be able to use the results in real scenario applications. Microelectronic devices can suffer from different types of effects:

5.3.2.1 Total ionising dose effects

Total Ionising Dose (TID) effects produce damage which accumulates over time causing device degradation and even failure. This damage is associated with the build-up of trapped charge carriers, either in an oxide layer or at the interface between the oxide and the bulk ($SiO_2 - Si$), which leads to the modification of the electric fields in the device.

While electron-hole pairs are generated by ionising radiation and normally migrate by diffusion and drift mechanisms, the charge carriers in the insulating oxide layers are characterised by a lower mobility than in the doped semiconductor regions, especially for holes, and become trapped by defects in the oxide layer. Thus, resulting in an accumulation of positive charges during irradiation. The main parameters influenced by TID in CMOS and bipolar device are:

- Shifts in the threshold voltages
- Change in the charge carrier mobility
- Increase of leakage currents

Dose values for the LHC experiments range a few Gy up to several MGy.

5.3.2.2 Single event effects

In Single Event Effects (SEEs), when an ionising particle deposits sufficient localised charge, normal functioning can be disrupted. For example, switching of bits ('1' $\leftrightarrow$ '0') in logic circuits or memory cells. Unlike TID and NIEL effects, SEEs are instantaneous and strongly dependent of the particle flux, which is proportional to the beam collision rate in the LHC. SEEs cover a range of radiation effects on electronic circuits triggered by the energy deposition of single particles traversing the device, including single event upset, single event latch-up, single event gate rupture, and single event burnout.

5.3.2.3 Displacement damage

Displacement damage in the silicon bulk also affect electronics. Though, CMOS devices are typically less sensitive to NIEL effects compared with TID due to the commonly higher charge carrier doping. On the other hand, bipolar electronics are usually more sensitive to bulk defects than CMOS ones.

Chapter 6

Electrical characterisation of silicon pixel sensors

As seen previously, the CMS Phase 2 tracker requires sensors capable of coping with the harsh environment conditions of the HL-LHC. Moreover, considering the HL-LHC *ultimate luminosity scenario* and the replacement of the tracker during LS5 as a baseline, the innermost layers will have to withstand $1MeV$ neutron equivalent fluences Φ_{eq} as high as $1.8 \cdot 10^{16}$ $n_{eq}cm^{-2}$ for an integrated luminosity of 4000 fb^{-1}, as see in Tables 6.1 and 6.2. Thus, thorough investigations are necessary to evaluate the radiation hardness and power dissipation of silicon sensors at these fluences.

This chapter focuses on the studies performed, the methods employed, and the results obtained with silicon pixel sensors. These devices were electrically characterised to study their electrical parameters and operational limits relevant to particle detection and how these are affected by radiation and annealing effects.

Under the framework outlined in chapter 5.3, we briefly mention the radiation induced effects and their impact on sensor performance:

1. Leakage current:

   Depends on fluence, temperature, and annealing effects.

2. Effective space charge (depletion voltage - effective doping concentration):

   Depends on fluence, annealing, material, particle type, and donor removal.

3. Charge carrier trapping:

   Depends on fluence and annealing.

TABLE 6.1: Integrated fluence and radiation dose for Run 4, 5, and 6 for different layers.

	Run 4		**Run 5**		**Run 6**	
Layer	Φ_{eq} [$n_{eq}cm^{-2}$]	Grad	Φ_{eq} [$n_{eq}cm^{-2}$]	Grad	Φ_{eq} [$n_{eq}cm^{-2}$]	Grad
BPix L1	$0.73 \cdot 10^{16}$	0.40	$1.16 \cdot 10^{16}$	0.63	$1.63 \cdot 10^{16}$	0.89
BPix L2	$0.20 \cdot 10^{16}$	0.11	$0.31 \cdot 10^{16}$	0.18	$0.44 \cdot 10^{16}$	0.25
FPix R1	$0.48 \cdot 10^{16}$	0.31	$0.77 \cdot 10^{16}$	0.50	$1.08 \cdot 10^{16}$	0.70
FPix R2	$0.23 \cdot 10^{16}$	0.17	$0.36 \cdot 10^{16}$	0.27	$0.51 \cdot 10^{16}$	0.38

TABLE 6.2: Integrated fluence and radiation dose for Run 4+5 and 4+5+6 for different layers.

	Run 4+5		**Run 4+5+6**	
Layer	Φ_{eq} [$n_{eq}cm^{-2}$]	Grad	Φ_{eq} [$n_{eq}cm^{-2}$]	Grad
BPix L1	$1.88 \cdot 10^{16}$	1.03	$3.51 \cdot 10^{16}$	1.91
BPix L2	$0.51 \cdot 10^{16}$	0.29	$0.94 \cdot 10^{16}$	0.55
FPix R1	$1.25 \cdot 10^{16}$	0.81	$2.34 \cdot 10^{16}$	1.50
FPix R2	$0.59 \cdot 10^{16}$	0.44	$1.11 \cdot 10^{16}$	0.82

One of the limitations of this study relies in the difference between the laboratory conditions and the real conditions. The many differences between laboratory conditions and particle detector conditions should not be disregarded. For example, experimental irradiation is done with mono-energetic single particle type beams, being different from the radiation conditions in the LHC experiments.

6.1 Experimental setting

Measurements were performed entirely in the laboratory of the UZH CMS group at the Physics Institute of the University of Zurich, Irchel campus, during the course of the years 2020-2021. The results reported in this chapter were generated exclusively with data extracted from those measurements, unless expressly indicated as different.

The instrumentation employed for the above mentioned comprehends a suite of systems which serve as a probe station, including the following main subsystems:

1. High Precision On-Wafer Probe System (Summit-12000, *Form Factor* (formerly *Cascade Microtech*)) [62].

- Chuck temperature range: $\{-60°C, +300°C\}$
- Chuck stable operational voltage range: $\pm 3000V$
- Electromagnetic interference (EMI) shielded
- Light-tight
- Moisture-free dew point $< -100°C$
- Integrated optical and digital zoom microscope *(eVue)*
- High voltage security interlock system with laser grid perimeter

2. High Performance Parameter Analyzer (4200A-SCS, *Keithley*) [63].
   - Current-Voltage measurement range with DC: $\{100fA, 1A\}$, $\{0.2\mu V, 210V\}$
   - Capacitance-Voltage measurement range: $\pm 30V$ DC bias,$\{1kHz, 10MHz\}$
3. High power Source Measure Unit (SMU) system (2657A, *Keithley*) [64].

   Voltage range:
   - $\pm 3000V$@$20mA$
   - $\pm 1500V$@$120mA$

   Resolution:
   - $100pA$@$100\mu A$
4. Pressurized dry air supply
5. External fast temperature response chiller
6. External CPU with Windows OS

The probe station is operated inside a clean room in the UZH CMS laboratory. A picture of the Probe Station suite inside the clean room is shown in Figure 6.1.

6.2 Tests performed

6.2.1 Leakage current vs bias voltage measurements

Silicon structures were electrically characterised using the probe station previously described in Experimental setting. The leakage current was measured as a function of the bias voltage applied.

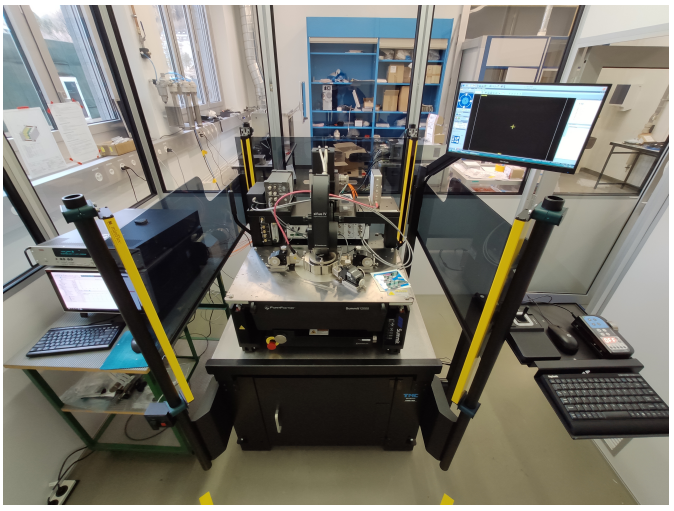

FIGURE 6.1: The Probe Station is shown with all subsystems except the dry air supply and the chiller which are located outside the clean room.

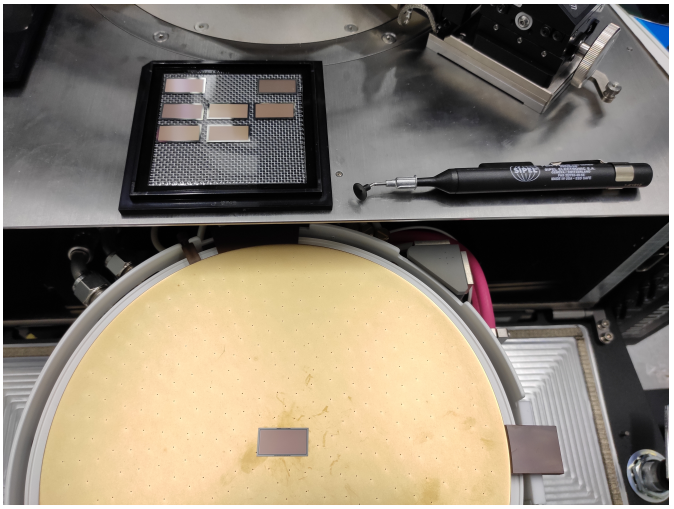

FIGURE 6.2: The chuck is ejected for placing the DUT and injected back for measuring. Vacuum is applied in concentric ring regions that can be enabled/disabled independently.

The Device(s) Under Test (DUT) were placed over a thermally controlled gold chuck equipped with vertical holes that allow vacuum to be applied to the bottom side of the DUT . This holds the DUT in a fixed position and also guarantees a good electrical connection. A picture of the Chuck with a DUT is shown in Figures 6.2 and 6.3.

A SMU Instrument from *Keithley*, described in chapter 6.1, was connected to the chuck applying a high DC voltage signal onto the backside of the sensor. Applying a high voltage signal through a large contact area instead of small one, minimises the risk of spark generation.

On the front side of the sensor, which faces the microscope, a needle serving as ground was connected by means of superficial scratches on coated areas like metallic pads or guard rings. A picture of probes with needles can be seen in Figure 6.4. Prior to contact, the needle lays diagonally, as seen in Figure 6.5. Pressing it slightly further from establishing

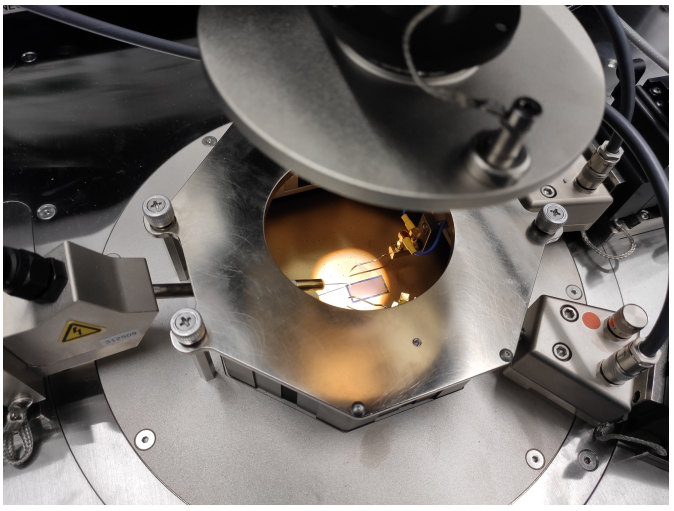

FIGURE 6.3: The probe station measuring chamber is shown with the DUT laying inside, placed on top of the chuck, and with the needle probes in place. Lowering the microscope closes the aperture and seals the chamber.

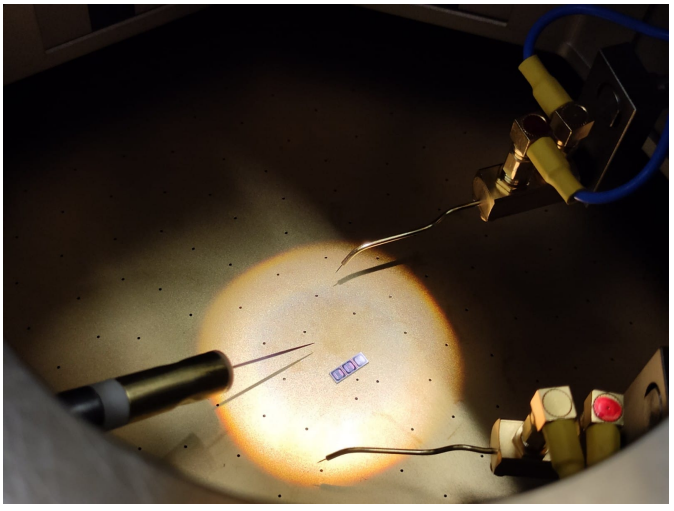

FIGURE 6.4: Needle probes are shown. Special needles are used for high voltages (left needle). With the DUT placed on the chuck, the chuck in the measuring position, and the microscope in the lowest position, probes can be brought into contact with the DUT.

surface contact will provoke it to slide on the surface as it scratches and spreads material to the sides of the needle ensuring a reliable electrical contact. Scratch lines varied in distance between $4\mu m$ and $8\mu m$. An example of such contact marks (scratches) is shown in Figure 6.6. The needle was also connected to the SMU instrument from *Keithley*. For the data taking, the voltage signal is applied with a reverse dual swipe voltage scan. Bias voltage starts from 0 and decreases in steps and at a constant rate until reaching the maximum negative amplitude, then it increases as well at a constant rate and in steps until reaching back to 0. Abrupt voltage changes should be avoided as they can result in device damage generated by induced high intensity electric currents or sparks. The potential difference applied is negative because the semiconductor structures studied

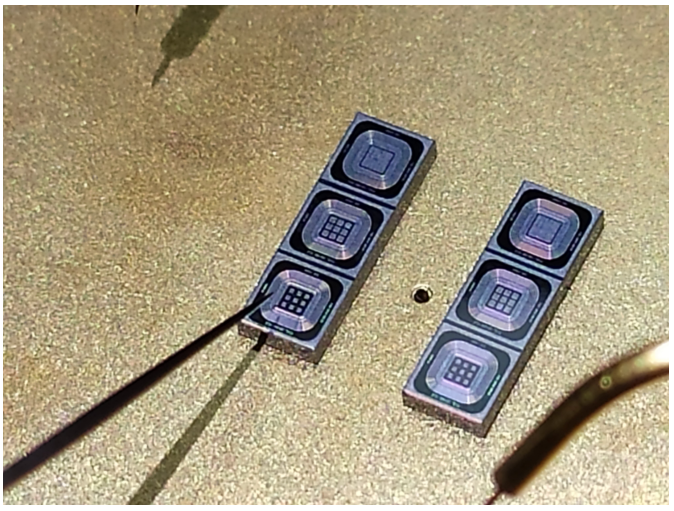

FIGURE 6.5: A pixel sensor is shown with a needle close to establishing contact.

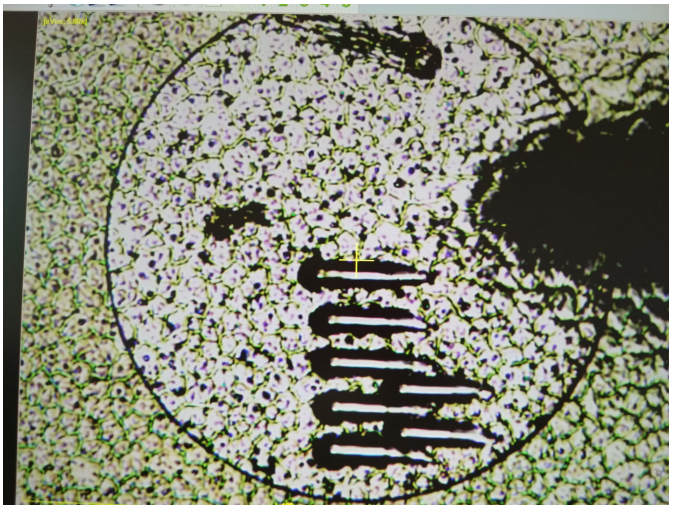

FIGURE 6.6: A sensor is shown depicting multiple contact marks (scratches). The needle (before establishing contact) can be seen as a blurry shadow on the right side of the image.

(Go back to Leakage current vs bias voltage measurements)

require reverse biasing for working appropriately, as a reverse biased diode. On the other hand, for the purpose of generating graphs, the absolute value of the potential difference was used.

6.2.2 Irradiation of sensors

Neutron irradiation of sensors was performed in the TRIGA Mark II (250 kW) research reactor at the Jožef Stefan Institute (JSI), in Ljubljana, in two subsequent steps, allowing measurements and annealing to be performed in between. On the first irradiation, $1MeV$ neutron equivalent fluences Φ_{eq} of $0.5 \cdot 10^{16}$ $\mathrm{n_{eq}} cm^{-2}$ and $1.0 \cdot 10^{16}$ $\mathrm{n_{eq}} cm^{-2}$ were applied to two groups of sensors, one to each group. On the second, all sensors were further

irradiated with a $1MeV$ neutron equivalent fluence Φ_{eq} of $1.0 \cdot 10^{16}$ $\mathrm{n_{eq}} cm^{-2}$, reaching a total fluence of $2.0 \cdot 10^{16}$ $\mathrm{n_{eq}} cm^{-2}$ for some of the structures. Sensors were kept in under 0 temperatures since irradiated until handed to the University of Zurich, where they were kept in a refrigerator in the UZH CMS laboratory at $-18°C$ to substantially slow the effects of annealing.

As mentioned in Requirements for the new tracker, the innermost regions of the CMS tracker are foreseen to be exposed to a total $1MeV$ neutron equivalent fluence Φ_{eq} of $1.8 \cdot 10^{16}$ $\mathrm{n_{eq}cm^{-2}}$ for an integrated luminosity of 4000 $\mathrm{fb^{-1}}$. That is why it comes natural to perform the experimental irradiation with the above mentioned fluences.

6.2.3 Temperature scaling of measurements

As seen previously in Temperature dependence and scaling, following the NIEL hypothesis allows to express ΔI_{leak} as a function of time and temperature, such that it can be scaled to other temperatures rather than the one of the original measurement, as expressed in 5.43:

$$I(T) = I(T_0)\left(\frac{T}{T_0}\right)^2 \exp\left[\frac{E_{eff}}{2k_B}\left(\frac{1}{T} - \frac{1}{T_0}\right)\right], \tag{6.1}$$

For this study, a value of $E_{eff} = 1.12eV$ from [59] was used for temperature scaling.

Comparing temperature scaled data measured at different temperatures also allows to verify the consistency of the temperature chuck as provided by the probe station.

Data from IV measurements performed up to a maximum bias voltage of $-900V$, with a voltage step of $5V$, with a current intensity compliance of $300\mu A$, and performed at $-25°C$ and $-40°C$ was used for scaling. Plots from measurements from 1 sensor irradiated with a $1MeV$ neutron equivalent fluence Φ_{eq} of $0.5 \cdot 10^{16}$ $\mathrm{n_{eq}}$ cm^{-2} and from 1 sensor irradiated with that of $1.0 \cdot 10^{16}$ $\mathrm{n_{eq}}$ cm^{-2} are shown in Figures 6.7 and 6.8, respectively. The description of the sensors will be treated later in Thin planar silicon sensors for the RD53A ROC.

It can be seen that the blue stripped curve, which is the data taken at $-40°C$ scaled to $-25°C$, fits precisely on top of the red curve, which is the data taken at $-25°C$. The parametrization used scales the data appropriately.

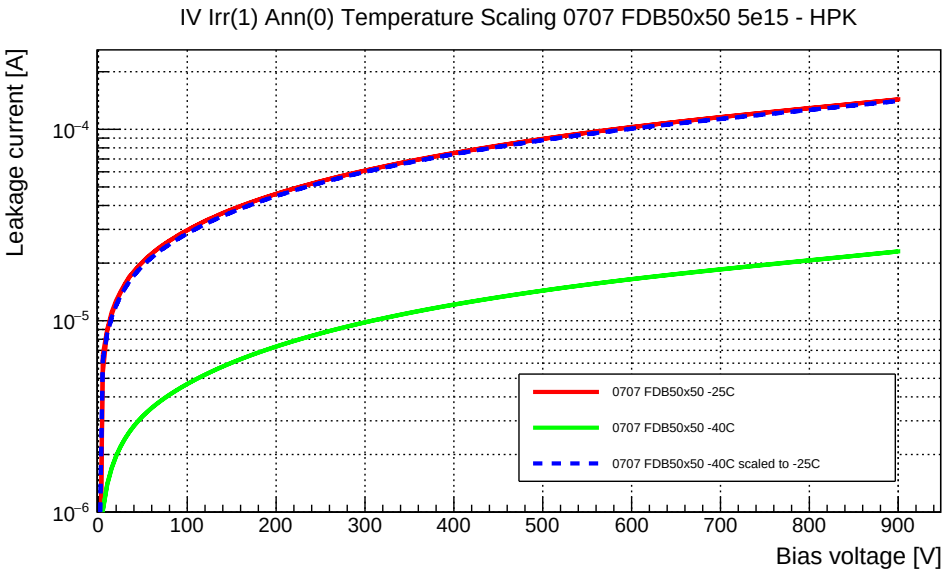

FIGURE 6.7: I_{leak} *vs.* V_{bias} plot showing measurements from a 0707 FDB 50×50 HPK RD53 silicon pixel sensors after neutron irradiated a $1MeV$ neutron equivalent fluence Φ_{eq} of $0.5 \cdot 10^{16} n_{\text{eq}}\ cm^{-2}$. The blue dashed curve shows the temperature scaled measurements. Measurements shown in logarithmic scale.

6.2.4 Annealing of sensors

The CMS detector systems are kept most of the time at low temperatures by the CO_2 evaporative cooling system (for example the pixel sensors in the Pixel Tracker operate in a range between $-10°C$ and $-20°C$ for a CO_2 temperature of $-33°C$), as mentioned in Subsystems. However, sometimes there are short stop periods, lasting hours or days, and long stop periods, lasting months, in which the effective cooling ceases and temperature rises. This effect can be seen in Figure 6.9, where the leakage current data stops from the end of 2017 until the first months of 2018, corresponding to a period of shutdown, after which the leakage current levels drop before starting to increase again.

As seen in Annealing - diffusion of defects, defects caused by displacement damage, as Interstitials I and vacancies V, can rearrange and form other structures. This processes are highly on temperature and can lead to important changes on the parameters of silicon sensors.

To study the annealing effects or irradiated sensors, samples were stored at $20°C$ in the CMS UZH laboratory. Higher temperatures greatly accelerate the annealing process and its effects on the structures.

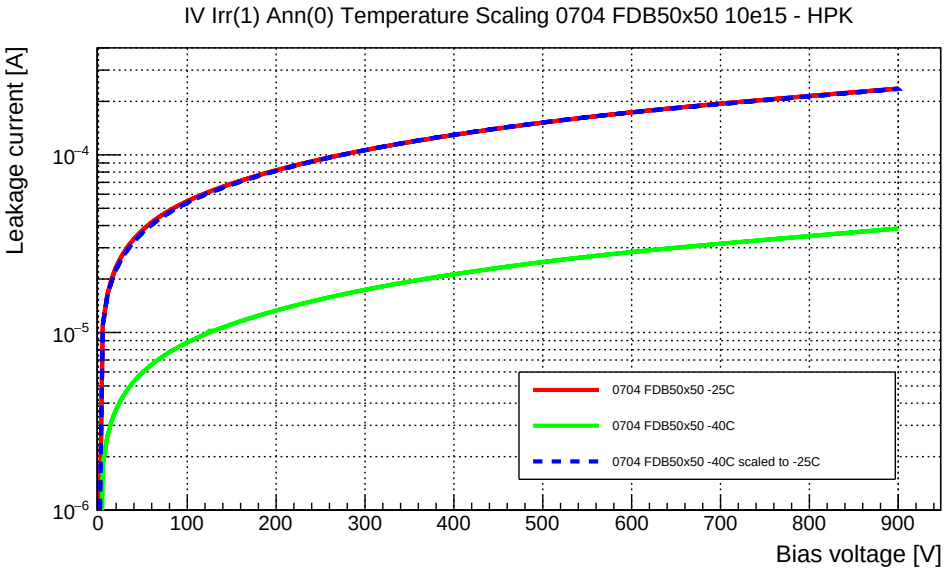

FIGURE 6.8: I_{leak} *vs.* V_{bias} plot showing measurements from a 0704 FDB 50×50 HPK RD53 silicon pixel sensor after neutron irradiation with a $1 MeV$ neutron equivalent fluence Φ_{eq} of $1.0 \cdot 10^{16}$ $\mathrm{n_{eq}}$ cm^{-2}. The blue dashed curve shows the temperature scaled measurements. Measurements shown in logarithmic scale.

6.3 Thin planar silicon sensors for the RD53A ROC

Thin planar silicon pixel sensors produced by Hamamatsu Photonics K.K. (HPK) were electrically characterised. The production of these sensors has been carried out in the framework of the CMS R&D campaign which aims towards developing silicon pixels sensors that will perform adequately in the CMS detector during the HL-LHC operations [65]. These sensors are designed to be compatible with the RD53A ROC.

6.3.1 Sensor description

Planar silicon pixel sensors were produced out of high-resistivity 150 μm p-type float zone wafers, with crystal orientation <100>. A 6" wafer with sensors for different ROCs is shown in Figure 6.10. The sensors charge profile technology is n^+ $-p$, as it is the planar technology of choice for Phase 2 IT, and is shown in the right side of Figure 6.11. Planar sensor technology allows for thinner sensors, smaller pixel cell sizes, and reduced inactive edges. In addition, n^+ $-p$ charge profile only requires lithographic treatment on one side, as contrary to n^+ $-n$, requiring less production steps and implying a lower cost. Though, additional processing is required to diminish the risk of sparks between the sensor edges and the ROC during high voltage operation. for the latter, a layer of benzocyclobutene (BCB) is deposited between the cut edge of the structure and the bias

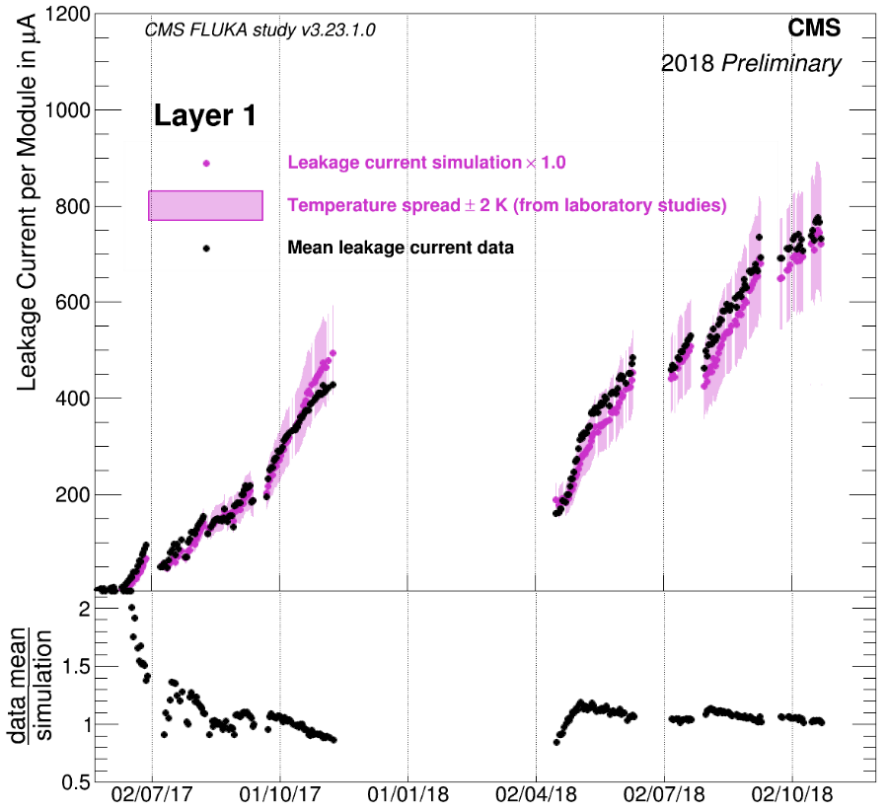

FIGURE 6.9: Leakage current as a function of time for the layer 1 (innermost) of the IT BPix [30].

ring, providing additional protection between sensor and chip. A diagram of such guard ring is shown in Figure 6.12.

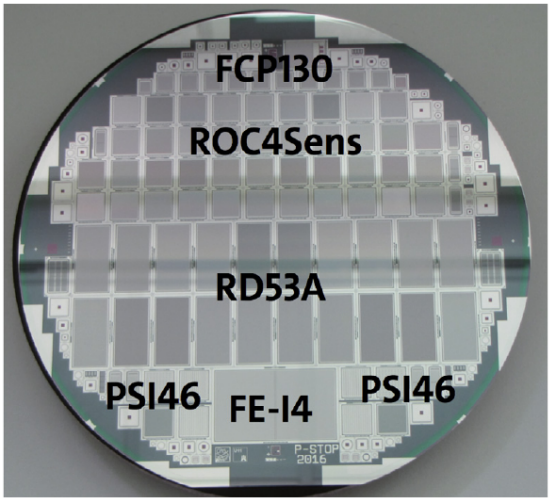

FIGURE 6.10: Layout of a 6" HPK sensor wafer with sensors for different ROCs [31].

The active thickness of the wafer for the sensors used in this study is 150 μm and 3 substrate options have been produced:

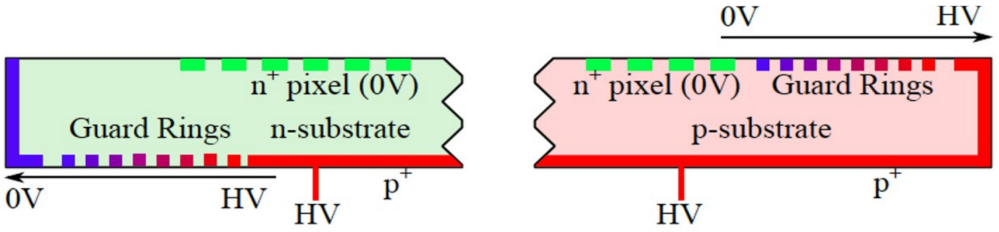

FIGURE 6.11: $n^+ - n$ (left) and $n^+ - p$ (right) charge profiles.

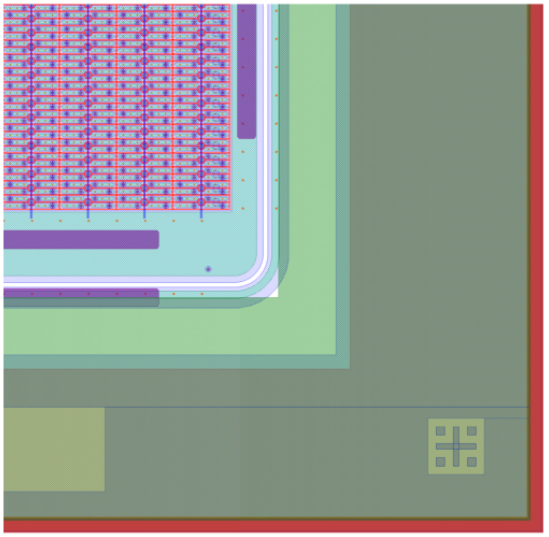

FIGURE 6.12: edge of a silicon pixel sensor including a BCB mask (green layer) aiming to prevent sparking.

1. Physically Thinned (FTH150)
2. Si-Si Direct Bonded (FDB150)
3. Deep-Diffused (FDD150)

For this work, only FTH150 and FDB150 sensors have been tested.

FTH150 sensors are mechanically thinned (float zone thinned) from the back side to the desired thickness. The back side implant is shallow making it sensitive to scratches which can lead to a high leakage current if the depletion region reaches the backside implant.

FDB150 sensors are obtained by bonding a high resistivity float zone wafer with a low resistivity handle wafer (float zone direct bonded). The float zone wafer is thinned down to an active thickness of 150 μm and has a deeper backside implant.

The total thickness results in 200 μm for FDB150 and 150 μm for FTH150. The bulk resistivity is specified to range between 3 to 5 $k\Omega$. The design of the sensors implements common bias/punch-through holes, polysilicon resistors, and open p-stop isolation.

For electrical characterisation, biasing structures are implemented which allow to measure the electrical properties of the sensor prior to interconnection (e.g. bump bonding). This structure is composed of a metal bias rail starting at the Bias Ring (BR), which is the innermost guard ring, and an implant dot (bias/punch-through dot) to which it is connected. The bias rail and the implant dot structures are shown in Figures 6.13 and 6.14, respectively. Generally, the nearest pixel cells are at a potential induced by the ground potential of the bias dot, as the implant follows the potential of the grounded one. This effect is known as punch-through and its mechanism allows the characterisation of the full sensor before interconnection. Thanks to the punch-through structures, all the pixels can be set to ground potential by establishing contact with a probe on a pad on the BR. The leakage current generated by the full active sensor area can be then collected by the probe needle. The previous should have a minimal impact on charge collection during high voltage operation after irradiation.

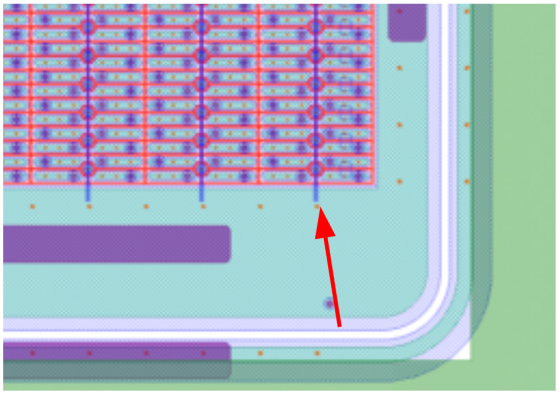

FIGURE 6.13: Bias rails are shown by the red arrow.

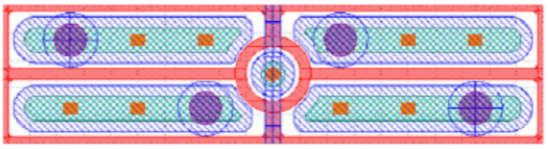

FIGURE 6.14: 100×25 μm^2 mask layout showing the bias punch-through structure as a red dot in the center of the diagram [31].

A diagram with designs for different sensor mask layouts is shown in Figure 6.15, and a diagram of the cross section of a thin planar sensor is shown in Figure 6.16.

8 different sensors were tested for this work. All were designed for the RD53A prototype chip featuring non-staggered bump bonding for pixel cell geometries of 50×50 μm^2 and 100×25 μm^2, with 192×400 cells. A list of all the structures used in this study is shown below:

1. FTH150 sensors (×4):

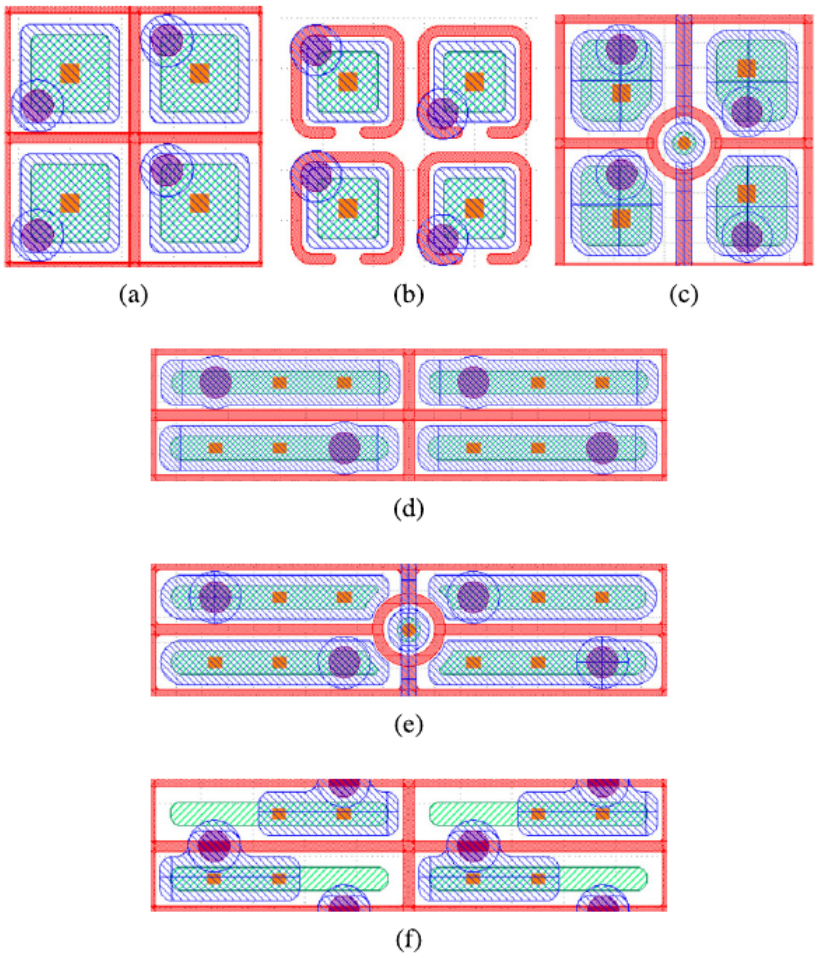

FIGURE 6.15: Different sensor mask layout designs for the RD53A ROC with p-stop isolation in 5×50 μm^2 and 100×25 μm^2. For this study, structures featuring punch-through dots have been measured, as shown in the top right (c) and bottom middle (e) designs [31].

- 100×25 μm^2 (×2):
  - 1317 FTH 100×25 μm^2
  - 1314 FTH 100×25 μm^2
- 50×50 μm^2 (×2):
  - 0507 FTH 50×50 μm^2
  - 0504 FTH 50×50 μm^2

2. FDB150 sensors (×4):

- 100×25 μm^2 (×2):
  - 0717 FDB 100×25 μm^2
  - 0714 FDB 100×25 μm^2
- 50×50 μm^2 (×2):

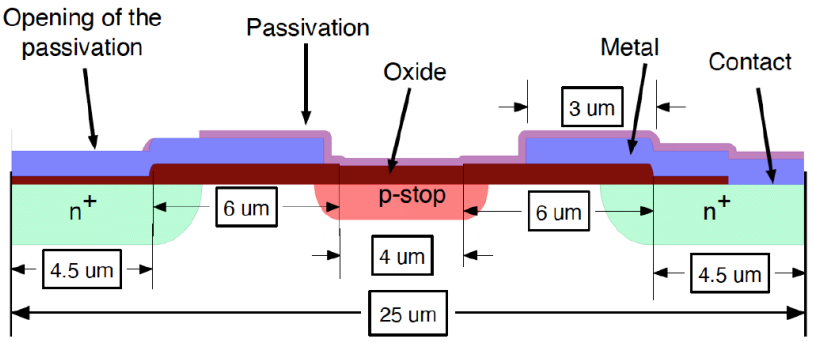

FIGURE 6.16: Inter-pixel region cross section for 100×25 μm^2 thin planar sensor without bias scheme [32].

- 0707 FDB 50×50 μm^2
- 0704 FDB 50×50 μm^2

6.3.2 Overview of irradiation, annealing, and measurement operations for the sensors tested

Sensors were first measured before going through a series of irradiation and annealing procedures. They were then remeasured after each of the following procedure steps, in order: 1^{st} irradiation → 1^{st} annealing → 2^{nd} irradiation → 2^{nd} annealing.

The irradiation and annealing procedures in order of execution with the corresponding fluences and annealing times for each sensor are shown in Table 6.3.

For simplicity, all procedures undergone by a sensor are not mentioned explicitly in plots, but only the last ones performed. Meaning, for example, that if sensor 1314 FTH 100×25 is shown in a plot after irradiation with a total $1MeV$ neutron equivalent fluence Φ_{eq} of $2.0 \cdot 10^{16}$ n_{eq} cm^{-2} and after 10 days of annealing, the real cumulative effects are: Φ_{eq} of $1.0 \cdot 10^{16}$ n_{eq} (1^{st} irradiation) + annealing 10 days (1^{st} annealing) + Φ_{eq} of $1.0 \cdot 10^{16}$ n_{eq} (2^{nd} irradiation) + annealing 10 days (2^{nd} annealing).

6.3.3 IV tests before irradiation and annealing

IV measurements were performed up to a maximum bias voltage of $-1500V$, with a voltage step of $10V$, with a current intensity compliance of $500\mu A$, and performed at $25°C$. Plots from measurements from 8 sensors before irradiation are shown in Figure 6.17.

Sensor ID	1^{st} **Irr.** Φ_{eq} [$n_{eq}cm^{-2}$]	1^{st} **Ann.** 20° time [days]	2^{nd} **Irr.** Φ_{eq} [$n_{eq}cm^{-2}$]	2^{nd} **Ann.** 20° time [days]
1317 FTH 100×25	$0.5 \cdot 10^{16}$	10	$1.0 \cdot 10^{16}$	10
0507 FTH 50×50	$0.5 \cdot 10^{16}$	10	$1.0 \cdot 10^{16}$	10
0717 FDB 100×25	$0.5 \cdot 10^{16}$	10	$1.0 \cdot 10^{16}$	10
0707 FDB 50×50	$0.5 \cdot 10^{16}$	10	$1.0 \cdot 10^{16}$	10
1314 FTH 100×25	$1.0 \cdot 10^{16}$	10	$1.0 \cdot 10^{16}$	10
0504 FTH 50×50	$1.0 \cdot 10^{16}$	10	$1.0 \cdot 10^{16}$	10
0714 FDB 100×25	$1.0 \cdot 10^{16}$	10	$1.0 \cdot 10^{16}$	10
0704 FDB 50×50	$1.0 \cdot 10^{16}$	10	$1.0 \cdot 10^{16}$	10

TABLE 6.3: Overview of irradiation and annealing procedures on sensors

A similar behaviour can be observed among all tested measured. The leakage current increased roughly at the same rate for all sensors until breakdown voltage was reached, ranging from $1000V$ to $1400V$. Break down behaviour is due to a high electric field being established by the bias voltage applied to the silicon sensors. Normally this happens along the implants of the pixel electrodes, at the p-stop structures, or between the edge pixels and the BR.

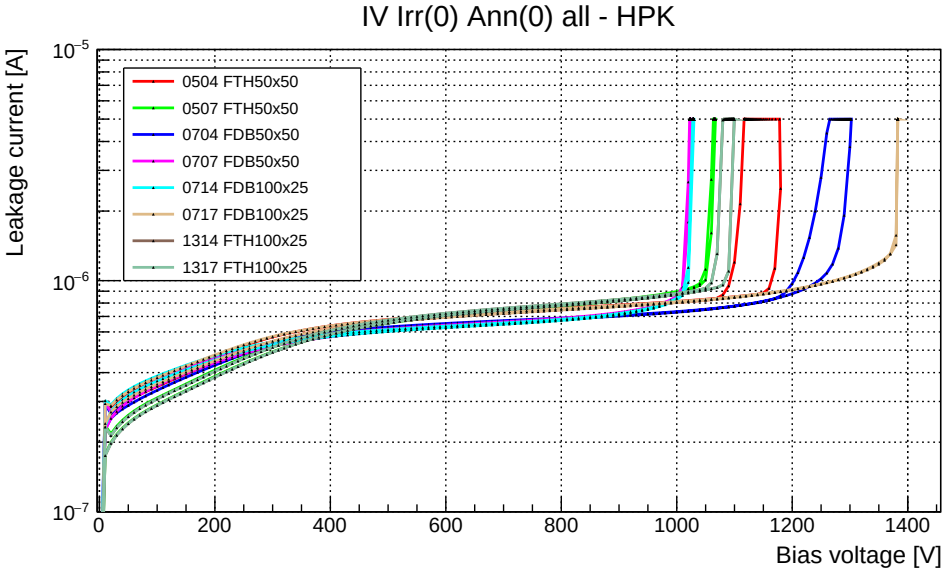

FIGURE 6.17: I_{leak} *vs.* V_{bias} plot showing measurements from 8 HPK RD53 silicon pixel sensors before irradiation. Measurements shown in logarithmic scale.

6.3.4 IV tests after 1st Irradiation

Four sensors were irradiated with a $1MeV$ neutron equivalent fluence Φ_{eq} of $0.5 \cdot 10^{16}$ $\mathrm{n_{eq}}$ cm^{-2} and 4 with that of $1.0 \cdot 10^{16}$ $\mathrm{n_{eq}}$ cm^{-2}, as shown in Table 6.4. All sensors were stored in a refrigerator in the UZH CMS laboratory at $-18°C$ after being irradiated to minimise unintentional annealing effects, except for when they were handled and prepared to be measured. We assume very small or no annealing effects at the time of measuring.

IV measurements were performed up to a maximum bias voltage of $-900V$, with a voltage step of $5V$, with a current intensity compliance of $300\mu A$, and performed at $-25C°$. Plots from measurements from 8 sensors after irradiation are shown in Figure 6.18. It can be seen that the leakage current increases with the irradiated fluence, this is consistent with what is expected as described in Radiation damage.

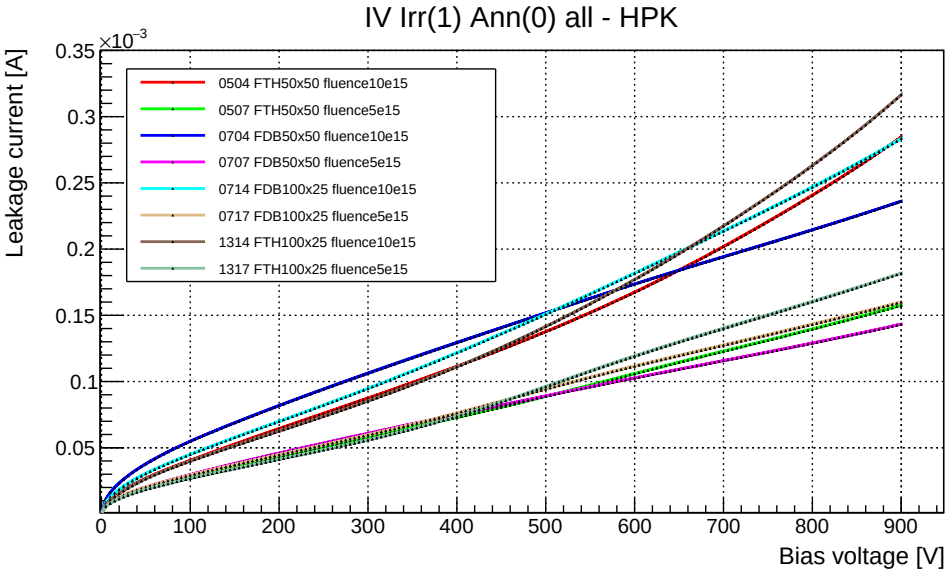

FIGURE 6.18: I_{leak} *vs.* V_{bias} plot showing measurements from 8 HPK RD53 silicon pixel sensors after irradiation. 4 of the sensors were exposed to a $1MeV$ neutron equivalent fluence Φ_{eq} of $0.5 \cdot 10^{16}$ $\mathrm{n_{eq}}$ cm^{-2}, and the other 4 to that of $1.0 \cdot 10^{16}$ $\mathrm{n_{eq}}$ cm^{-2}.

6.3.5 IV tests after 1st Irradiation and 1st Annealing

Sensors were annealed for 10 days at $20°C$. Measurements were performed after 0, 2, 5, and 10 days of annealing. Annealing took place in a shelf in the CMS UZH laboratory and otherwise they were stored in a refrigerator in the laboratory at $-18°C$ to minimise further unintentional annealing effects.

IV measurements were performed up to a maximum bias voltage of $-900V$, with a voltage step of $5V$, with a current intensity compliance of $300\mu A$, and performed at $-25°C$. Plots from measurements from 1 sensor after irradiation and annealing are shown in Figures 6.19 and 6.20. A decrease of the leakage current with annealing time can be seen, following the behaviour explained in Radiation damage.

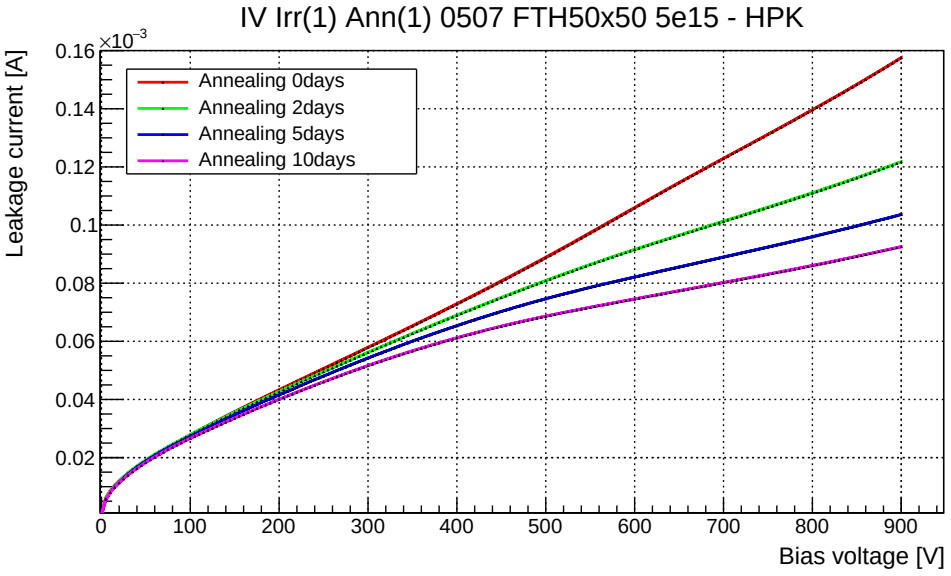

FIGURE 6.19: I_{leak} *vs.* V_{bias} plot showing measurements from a 0507 FTH 50×50 HPK RD53 silicon pixel sensor after irradiation and annealing. The sensor was exposed to a $1MeV$ neutron equivalent fluence Φ_{eq} of $0.5 \cdot 10^{16}$ $\mathrm{n_{eq}}$ cm^{-2} and was annealed for 10 days at $20°C$.

6.3.6 IV tests after 2nd Irradiation

All sensors were irradiated with an extra $1MeV$ neutron equivalent fluence Φ_{eq} of $1.0 \cdot 10^{16}$ $\mathrm{n_{eq}}$ cm^{-2} resulting in a total $1MeV$ neutron equivalent fluence Φ_{eq} of $1.5 \cdot 10^{16}$ $\mathrm{n_{eq}}$ cm^{-2} for 4 of them and a total fluence of $2.0 \cdot 10^{16}$ $\mathrm{n_{eq}}$ cm^{-2} for the other 4, as shown in Table 6.5.

All sensors were stored in a refrigerator in the UZH CMS laboratory at $-18°C$ after being irradiated to minimise unintentional annealing effects, except for when they were handled and prepared to be measured.

IV measurements were performed up to a maximum bias voltage of $-900V$, with a voltage step of $5V$, with a current intensity compliance of $300\mu A$ and $450\mu A$, and performed at $-25C°$. Plots from measurements from all 8 sensors irradiated with total $1MeV$ neutron equivalent fluences Φ_{eq} of $0.5 \cdot 10^{16}$, $1.0 \cdot 10^{16}$, $1.5 \cdot 10^{16}$, and $2.0 \cdot 10^{16}$ $\mathrm{n_{eq}}$ cm^{-2} are shown in Figure 6.21.

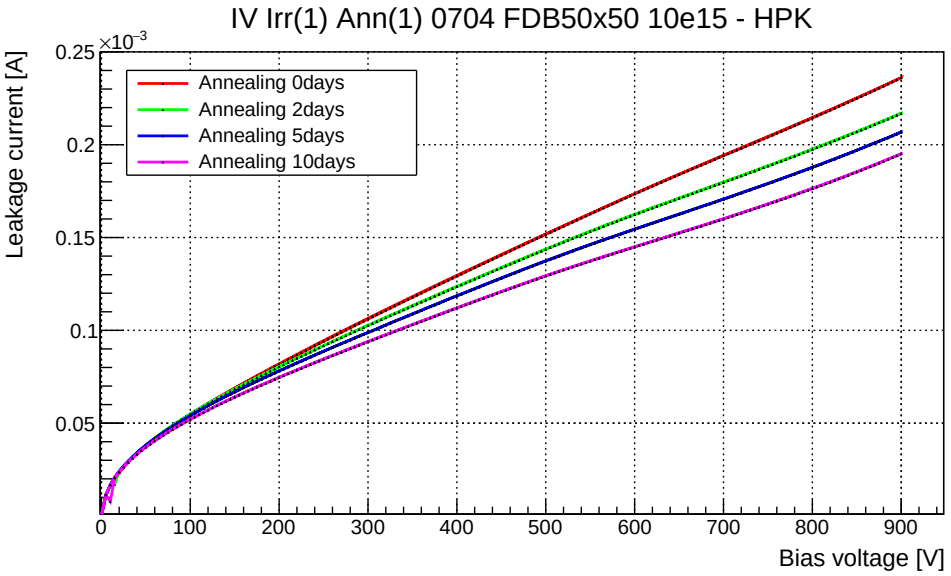

FIGURE 6.20: I_{leak} *vs.* V_{bias} plot showing measurements from a 0704 FDB 50×50 HPK RD53 silicon pixel sensor after irradiation and annealing. The sensor was exposed to a $1MeV$ neutron equivalent fluence Φ_{eq} of $0.5 \cdot 10^{16}$ $\mathrm{n_{eq}}$ cm^{-2} and was annealed for 10 days at $20°C$.

6.3.7 IV tests after 2nd Irradiation and 2nd annealing

After the second irradiation, sensors were annealed for 10 days at $20°C$. Measurements were performed after 0, 2, 5, and 10 days of annealing, which took place in a shelf in the CMS UZH laboratory, and otherwise they were stored in a refrigerator in the laboratory at $-18°C$ to minimise further unintentional annealing effects.

Sensors were measured several times after several days of annealing at in a shelf in the CMS UZH laboratory. IV measurements were performed up to a maximum bias voltage of $-900V$, with a voltage step of $5V$, with a current intensity compliance of $300\mu A$ and $600\mu A$, and performed at $-25°C$. Plots from measurements from 1 sensor after irradiation and annealing are shown in Figures 6.22 and 6.23.

It can be seen that the leakage current changes with annealing time at $20°C$, corresponding to lower current intensity for longer annealing times.

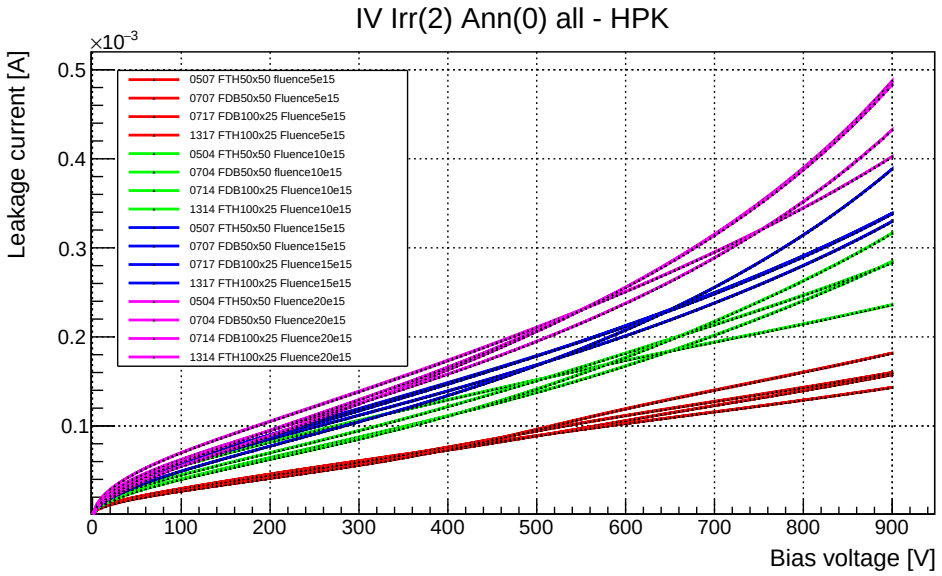

FIGURE 6.21: I_{leak} *vs.* V_{bias} plot showing measurements from 8 HPK RD53 silicon pixel sensors after irradiation and annealing. Total accumulated fluences are shown. On the first irradiation, 4 sensors were exposed to a $1MeV$ neutron equivalent fluence Φ_{eq} of $0.5 \cdot 10^{16}$ $\mathrm{n_{eq}}$ cm^{-2}, the other 4 to that of $1.0 \cdot 10^{16}$ $\mathrm{n_{eq}}$ cm^{-2}. After the first irradiation, sensors were annealed 10 days at $20°C$. On the second irradiation, all sensors were further exposed to a $1MeV$ neutron equivalent fluence Φ_{eq} of $1.0 \cdot 10^{16}$ $\mathrm{n_{eq}}$ cm^{-2}.

6.3.8 Power consumption on HPK RD53A bare sensors after irradiation and annealing

Power consumption of bare silicon pixel sensors after irradiation and annealing effects are calculated. As seen previously, irradiation and annealing effects have an impact on the electrical parameters of the sensors and this affects their power consumption during operation. Power consumption is a crucial parameter because it has direct implications on the sensor and module temperature, and electrical parameters are highly dependant on temperature.

In order to calculate the power consumption, information from test-beam data was used to determine the operational bias voltage, as shown in Figure 6.24 for reaching hit efficiency $> 99\%$ for each total $1MeV$ neutron equivalent fluence Φ_{eq}:

- $\Phi_{eq} = 0.5 \cdot 10^{16}$ $\mathrm{n_{eq}} cm^{-2}$: $600V$
- $\Phi_{eq} = 1.0 \cdot 10^{16}$ $\mathrm{n_{eq}} cm^{-2}$: $600V$ & $800V$
- $\Phi_{eq} = 1.5 \cdot 10^{16}$ $\mathrm{n_{eq}} cm^{-2}$: $600V$ & $800V$
- $\Phi_{eq} = 2.0 \cdot 10^{16}$ $\mathrm{n_{eq}} cm^{-2}$: $800V$

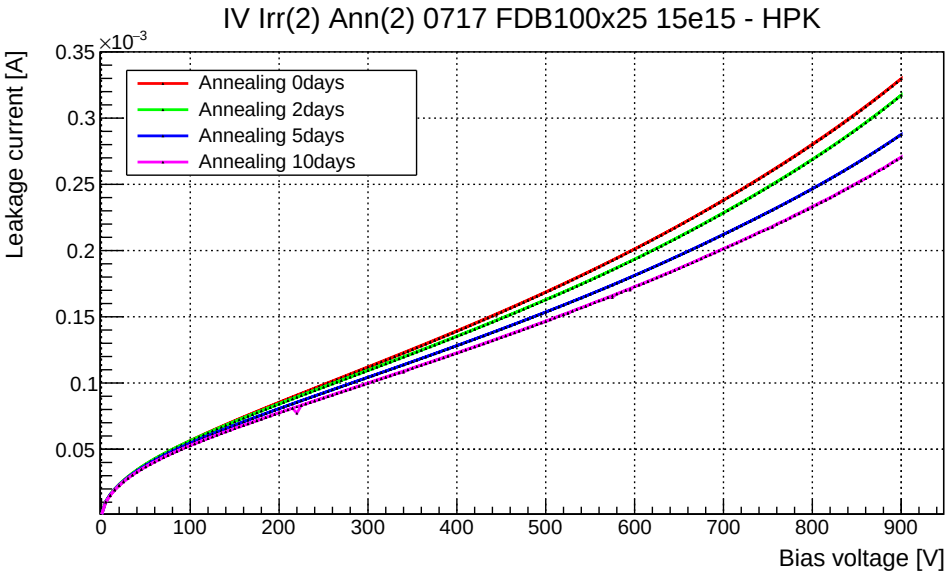

FIGURE 6.22: I_{leak} *vs.* V_{bias} plot showing measurements from a 0717 FDB 100×25 HPK RD53 silicon pixel sensor after irradiation and annealing. The sensor was exposed to a total $1MeV$ neutron equivalent fluence Φ_{eq} of $1.5 \cdot 10^{16}$ $\mathrm{n_{eq}}$ cm^{-2} and annealed for 10 days at $20°C$.

Referring to Equation 5.44:

$$\alpha(t) = \alpha_0 + \alpha_1 \cdot e^{-\frac{t}{\tau_1}} + \alpha_2 \cdot \ln(\frac{t}{t_0}), \tag{6.2}$$

which describes the evolution with time and temperature of the current related damage factor alpha, It can be seen that the exponential term $\exp(-t/\tau_1)$ has a quickly vanishing behaviour, contrary to the longer lasting logarithmic term $ln(t)$, which changes more slowly.

In Figure 5.30, a plot showing the annealing behaviour of the current-related factor $\alpha(t)$ as a function of time for irradiated sensors is shown. Following the curve for $T = 21°C$, the decrease of α since the first minutes until 10 days will be around 70% of the total decrease it will suffer since the first minutes until 1 year. In that way, 10 days is a representative amount of time to evaluate annealing effects for the tests performed

Power was calculated using the formula $P = V \cdot I$, and knowing the area of the sensors. The results of the calculations of the sensor power consumption per unit of area for the different total fluences and voltages are shown in Tables 6.4 and 6.5. The average power consumption per unit of area for each voltage and each fluence as a function of the annealing effects is shown in Table 6.6. It can be seen that the average power consumption for all irradiation fluences at both $600V$ and $800V$ decreases after annealing for 10 days at $20°C$, and in fact, it decreased monotonically from 0 to 10 days of annealing

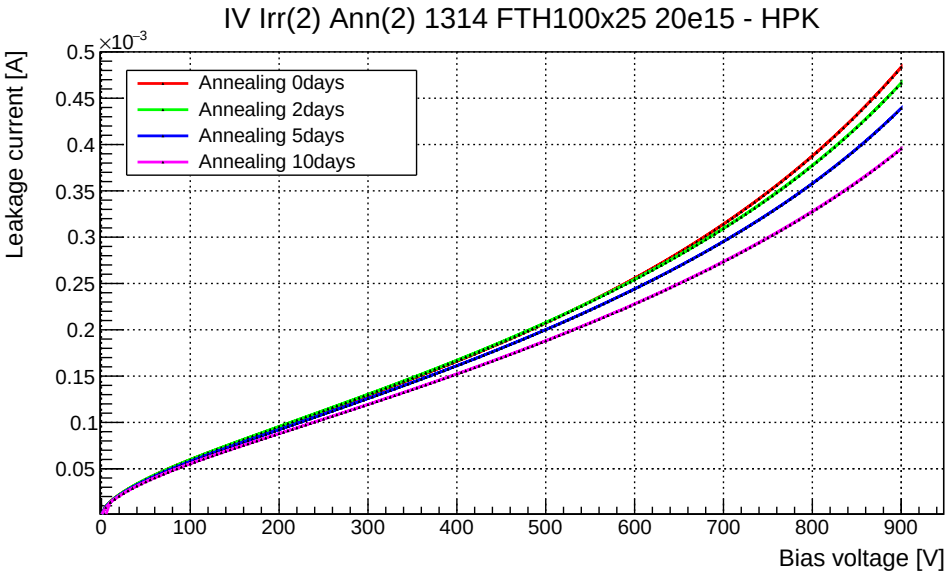

FIGURE 6.23: I_{leak} *vs.* V_{bias} plot showing measurements from a 1314 FTH 100×25 HPK RD53 silicon pixel sensor after irradiation and annealing. The sensor was exposed to a total $1MeV$ neutron equivalent fluence Φ_{eq} of $2.0 \cdot 10^{16}$ $\mathrm{n_{eq}}$ cm^{-2} and annealed for 10 days at $20°C$.

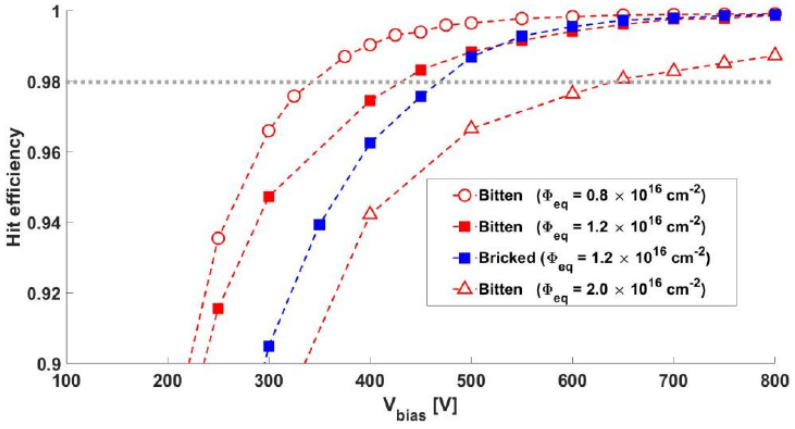

FIGURE 6.24: Hit efficiency as a function of bias voltage for irradiated structures [32].

for all the measurements performed. This is a direct consequence of the decrease of leakage current due to annealing.

Total Fluence $[\Phi_{eq}]$	Voltage $[V]$	1^{st} **Irr.** $[\Phi_{eq}]$	1^{st} **Ann.** time [days]	2^{nd} **Irr.** $[\Phi_{eq}]$	2^{nd} Ann. time [days]	Current $[\mu A]$	Current/area $[\mu A cm^{-2}]$	Power/area $[mW cm^{-2}]$
$0.5 \cdot 10^{16}$	600	$0.5 \cdot 10^{16}$	-	-	-	109.8	56.6	43.0
$0.5 \cdot 10^{16}$	600	$0.5 \cdot 10^{16}$	10	-	-	77.6	40.0	24.0
$0.5 \cdot 10^{16}$	800	$0.5 \cdot 10^{16}$	-	-	-	142.9	73.7	58.9
$0.5 \cdot 10^{16}$	800	$0.5 \cdot 10^{16}$	10	-	-	87.6	45.1	36.1
$1.0 \cdot 10^{16}$	600	$1.0 \cdot 10^{16}$	-	-	-	167.5	86.3	51.8
$1.0 \cdot 10^{16}$	600	$1.0 \cdot 10^{16}$	10	-	-	138.2	71.2	43.7
$1.0 \cdot 10^{16}$	800	$1.0 \cdot 10^{16}$	-	-	-	241.3	124.4	99.5
$1.0 \cdot 10^{16}$	800	$0.5 \cdot 10^{16}$	10	-	-	177.9	91.7	73.4

TABLE 6.4: Power consumption per unit area for irradiated and annealed sensors for total $1MeV$ neutron equivalent fluences Φ_{eq} of $0.5 \cdot 10^{16}$ $\mathrm{n_{eq}cm^{-2}}$ and $1.0 \cdot 10^{16}$ $\mathrm{n_{eq}cm^{-2}}$.

Total Fluence $[\Phi_{eq}]$	Voltage $[V]$	1^{st} **Irr.** $[\Phi_{eq}]$	1^{st} **Ann.** time [days]	2^{nd} **Irr.** $[\Phi_{eq}]$	2^{nd} Ann. time [days]	Current $[\mu A]$	Current/area $[\mu A cm^{-2}]$	Power/area $[mW cm^{-2}]$
$1.5 \cdot 10^{16}$	600	$0.5 \cdot 10^{16}$	26	$1.0 \cdot 10^{16}$	-	208.3	107.4	64.4
$1.5 \cdot 10^{16}$	600	$0.5 \cdot 10^{16}$	26	$1.0 \cdot 10^{16}$	10	180.3	93.0	55.8
$1.5 \cdot 10^{16}$	800	$0.5 \cdot 10^{16}$	26	$1.0 \cdot 10^{16}$	-	293.8	151.5	121.2
$1.5 \cdot 10^{16}$	800	$0.5 \cdot 10^{16}$	26	$1.0 \cdot 10^{16}$	10	245.2	126.4	101.1
$2.0 \cdot 10^{16}$	600	$1.0 \cdot 10^{16}$	26	$1.0 \cdot 10^{16}$	-	254.6	131.2	78.7
$2.0 \cdot 10^{16}$	600	$1.0 \cdot 10^{16}$	26	$1.0 \cdot 10^{16}$	10	219.4	113.1	67.9
$2.0 \cdot 10^{16}$	800	$1.0 \cdot 10^{16}$	26	$1.0 \cdot 10^{16}$	-	377.3	194.5	155.6
$2.0 \cdot 10^{16}$	800	$0.5 \cdot 10^{16}$	26	$1.0 \cdot 10^{16}$	10	312.2	161.0	128.8

TABLE 6.5: Power consumption per unit area for irradiated and annealed sensors for total $1MeV$ neutron equivalent fluences Φ_{eq} of $1.5 \cdot 10^{16}$ $\mathrm{n_{eq}cm^{-2}}$ and $2.0 \cdot 10^{16}$ $\mathrm{n_{eq}cm^{-2}}$.

6.3.9 Thermal run-away simulation

The results on the sensor power dissipation have been used to study the thermal performance of planar silicon sensors at the end of the lifetime of the detector. In particular, simulations have been performed assuming the measured leakage current and power dissipation to assess if the cooling system would be able to cope with the dissipated heat to avoid the pixel modules falling into thermal run-away. This is a "snow-ball" effect based on the fact that the leakage current scales with temperature, and as well, an increase of leakage current increases the power dissipated by the module, which in turn increases the temperature. In this way, a small difference between the amount of

		Power/area $[mW\ cm^{-2}]$		
Total fluence Φ_{eq} $[\mathrm{n_{eq}cm^{-2}}]$	Voltage [V]	No annealing	Annealing	Decrease [%]
$0.5 \cdot 10^{16}$	600	34.0	24.0	29
$1 \cdot 10^{16}$	600	51.8	42.7	18
$1.5 \cdot 10^{16}$	600	64.4	55.8	13
$1 \cdot 10^{16}$	800	99.5	73.4	26
$1.5 \cdot 10^{16}$	800	121.2	101.1	17
$2 \cdot 10^{16}$	800	155.6	128.8	17

TABLE 6.6: Power consumption per unit area for irradiated and annealed sensors for total $1MeV$ neutron equivalent fluences Φ_{eq} of $1.5 \cdot 10^{16}$ $\mathrm{n_{eq}cm^{-2}}$ and $2.0 \cdot 10^{16}$ $\mathrm{n_{eq}cm^{-2}}$..

heat dissipated by modules and the amount of heat carried away by the cooling system can lead to uncontrolled adverse results. As discussed previously, the leakage current rises with the irradiation fluence, leading to a consequent increase of the sensor power consumption. If the cooling system would fail to absorb the additional heat, temperature would rise inducing an increase of the leakage current having possible permanent damage of the sensors and modules. The results of a thermal run-away simulation at a $1MeV$ equivalent fluence Φ_{eq} of $2 \cdot 10^{16}$ $\mathrm{n_{eq}cm^{-2}}$ for the innermost Barrel Tracker layer is shown in Figure 6.25. It can be seen that planar sensors (black curve) fall in thermal runaway for temperatures higher than $-41°C$, which is below the expected working point of the CO_2 system, at $T = -33$C.

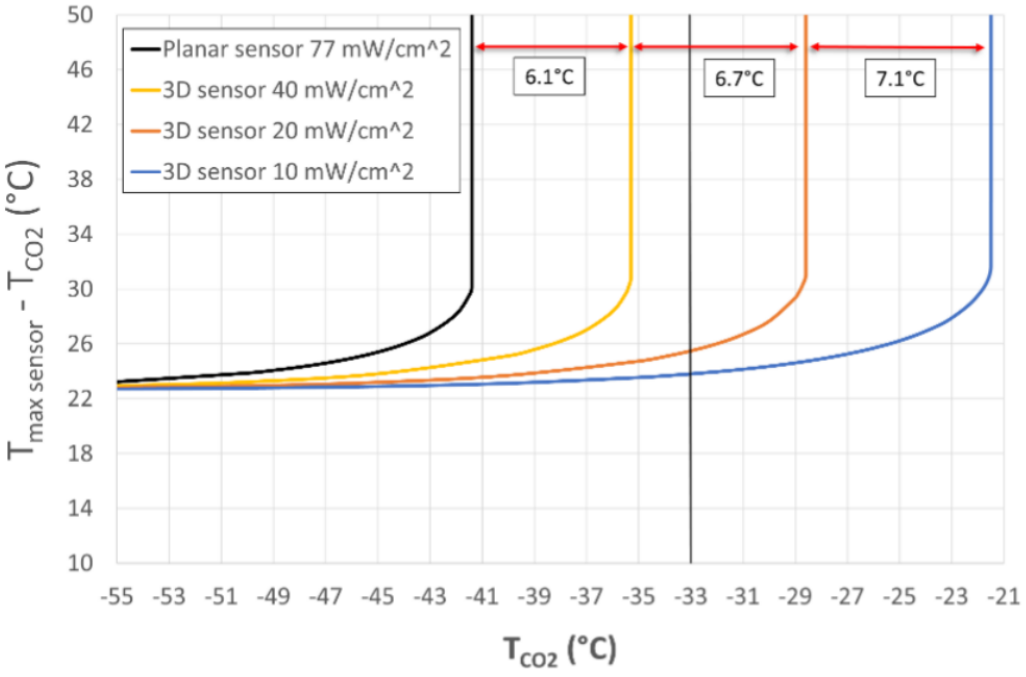

FIGURE 6.25: Thermal Run-away simulation for the innermost Barrel Tracker layer after a $1MeV$ equivalent fluence Φ_{eq} of $2 \cdot 10^{16}$ $n_{eq}cm^{-2}$ showing the temperature difference between the CO_2 cooling system and the sensors. Black curve corresponds to planar sensors, coloured curves to 3D sensors. Adapted from [33].

Chapter 7

Conclusions

Pixel sensor prototypes that were developed for the upgrade of the Phase-2 tracker, under the framework of CMS R&D, have been investigated after the effects of irradiation with fluences corresponding to the life span of the CMS Tracker.

For the previous, leakage current has been measured as a function of the bias voltage applied to the sensors, after being irradiated with different fluences and after different annealing times.

All sensors showed an increased of their leakage current after being irradiated, which is a clear signature of NIEL induced defects in the silicon bulk. Additionally, all sensors had a decrease of such currents with annealing time at $20°C$ for several days. As well, the speed of decrease slowed with time, as part of the annealing effects have a quick decaying behaviour, while others have a longer one.

The power dissipated by bare thin planar silicon sensors has been calculated for bias voltages guaranteeing high hit efficiencies. The power dissipation calculations have been used for the full thermal simulation of the CMS tracker system. As outcome, thin planar sensors appear to be the less favourable solution for the innermost layer of the Barrel Pixel detector. Though, the cooling performance is good enough for implementing thin planar sensors in all the other layers of the Tracker.

Appendix A

The Elevator Talk

A 22 storey trip, perhaps.

You: Hey man, how are you!

Me: Hey, ciao! I'm good, and you? Long time no see you.

You: Yeah, I'm fine, ty! And how's your thesis doing?

Me: Oh I'm actually still writing, hehe, but it's going..

You: That's nice. And what was it about?

Me: It's on experimental. I'm working with some silicon sensors for CMS.

You: Ahh, the project for the LHC, right? What was it exactly?

Me: It's actually very cool. So, first they accelerate bunches of protons going clockwise and anticlockwise along the LHC ring pipe at nearly the speed of light. Around 99.9999 percent of c, actually. Very fast, haha.

You: Damn!

Me: Yeah, haha. Then they make them collide where the detectors are, which are spread along the ring, and then they study the debris of the collisions that ideally go through the detector material. In the CMS there are some specific systems to detect and measure them. For example, energy and trajectories are measured with calorimeters and trackers, respectively.

The sensors I work with are part of the innermost tracking system, they are basically small silicon pixels arranged in some kind of cylindrical structure around, concentrical,

and very close to the the pipe so they can see things very "early". They get a lot of radiation, though.

The thing is that for easing our thirst for knowledge, the LHC will get a mayor improve on collision energy, frequency, amount, within others; the HL-LHC phase, namely. Which in turn requires improving some of the systems inside for being able to cope with all the new stats and actually profiting from them. For example, new sensors should be faster and able to withstand the much higher radiation without suffering too much damage. The ones inside right would probably fry.

So CERN researches and develop new sensors and some of them are sent to us to measure them and to simulate some of the working conditions. For example, we cool them, measure them, send them to be irradiated, measure them again, bake them, as some radiation damage can get annealed with random thermal motion, and like that.

At the end of the day, we would like to understand the behavior of these new sensors so they can continue improving them until they reach the sweet spot and then be installed when the machine goes into one of the large shut downs.

You: Wow, it actually sounds very fun!

Me: Indeed!

You: Hey, I go out in this floor see you soon, and thank you for the explanation.

Me: A pleasure. See you soon.

Bibliography

[1] Stefano Pozzorini. *Elementary Particle Theory*. University of Zurich, Zurich, Switzerland, 2021.

[2] "CMS Collaboration". Some LHC milestones.... Quelques dates clés du LHC... *journal*, page 1, Sep 2008. URL https://cds.cern.ch/record/1125888. Cover article.

[3] "Kein Einstein". "hydrogen bottle". *journal*, page 1, Oct 2008. URL https://commons.wikimedia.org/wiki/File:Protonenquelle_LINAC2.jpg.

[4] Esma Mobs. The CERN accelerator complex - 2019. Complexe des accélérateurs du CERN - 2019. *journal*, Jul 2019. URL https://cds.cern.ch/record/2684277. General Photo.

[5] Vladimir Shiltsev and Frank Zimmermann. Modern and Future Colliders. *Rev. Mod. Phys.*, 93:015006. 61 p, Mar 2019. doi: 10.1103/RevModPhys.93.015006. URL https://cds.cern.ch/record/2713605. Submitted to Rev.Mod.Phys.

[6] The ATLAS Collaboration et al. The ATLAS experiment at the CERN large hadron collider. *Journal of Instrumentation*, 3(08):S08003–S08003, aug 2008. doi: 10.1088/1748-0221/3/08/s08003. URL https://doi.org/10.1088/1748-0221/3/08/s08003.

[7] The CMS Collaboration et al. The CMS experiment at the CERN LHC. *Journal of Instrumentation*, 3(08):S08004–S08004, aug 2008. doi: 10.1088/1748-0221/3/08/s08004. URL https://doi.org/10.1088/1748-0221/3/08/s08004.

[8] The ALICE Collaboration et al. The ALICE experiment at the CERN LHC. *Journal of Instrumentation*, 3(08):S08002–S08002, aug 2008. doi: 10.1088/1748-0221/3/08/s08002. URL https://doi.org/10.1088/1748-0221/3/08/s08002.

[9] The LHCb Collaboration et al. The LHCb detector at the LHC. *Journal of Instrumentation*, 3(08):S08005–S08005, aug 2008. doi: 10.1088/1748-0221/3/08/s08005. URL https://doi.org/10.1088/1748-0221/3/08/s08005.

[10] CERN. High Luminosity LHC Project. *journal*, 2022. URL https://hilumilhc.web.cern.ch/sites/default/files/HL-LHC_Janvier2022.pdf.

[11] Tai Sakuma. Cutaway diagrams of CMS detector. *Journal*, May 2019. URL https://cds.cern.ch/record/2665537.

[12] David Barney. CMS Detector Slice. CMS Collection., Jan 2016. URL https://cds.cern.ch/record/2120661.

[13] Izaak Neutelings. Cms conventional coordinate system. *CMS Wiki Pager*, June 2017. URL https://wiki.physik.uzh.ch/cms/latex:example_spherical_coordinates.

[14] "CMS Collaboration". The Phase-2 Upgrade of the CMS Tracker. Technical report, CERN, Geneva, Jun 2017. URL https://cds.cern.ch/record/2272264.

[15] W. Adam et al. The CMS phase-1 pixel detector upgrade. *Journal of Instrumentation*, 16(02):P02027–P02027, feb 2021. doi: 10.1088/1748-0221/16/02/p02027. URL https://doi.org/10.1088/1748-0221/16/02/p02027.

[16] J Mans, J Anderson, B Dahmes, P de Barbaro, J Freeman, T Grassi, E Hazen, J Mans, R Ruchti, I Schimdt, T Shaw, C Tully, J Whitmore, and T Yetkin. CMS Technical Design Report for the Phase 1 Upgrade of the Hadron Calorimeter. Technical report, CERN, Sep 2012. URL https://cds.cern.ch/record/1481837. Additional contact persons: Jeffrey Spalding, Fermilab, spalding@cern.ch, Didier Contardo, Universite Claude Bernard-Lyon I, contardo@cern.ch.

[17] Manfred Jeitler. Upgrade of the trigger system of cms. *Nuclear Instruments and Methods in Physics Research Section A: Accelerators, Spectrometers, Detectors and Associated Equipment*, 718:11–15, 08 2013. doi: 10.1016/j.nima.2012.08.091.

[18] Stella Orfanelli. The Phase 2 upgrade of CMS Inner Tracker. Technical report, CERN, Geneva, Feb 2020. URL https://cds.cern.ch/record/2780125.

[19] M. K. Lee S. M. Sze. *Semiconductor Devices Physics and Technology-Wiley*. Wiley, New York, 2012. URL https://www.wiley.com/en-us/Semiconductor+Devices%3A+Physics+and+Technology%2C+3rd+Edition-p-9780470914076.

[20] Gerhard Lutz. *Semiconductor Radiation Detectors Device Physics*. Springer, Berlin, 2007. URL https://link.springer.com/book/10.1007/978-3-540-71679-2?noAccess=true.

[21] Alan Owens. *Semiconductor radiation detectors*. CRC Press, Taylor amp; Francis Group, 2019. ISBN 9781315114934. doi: https://doi.org/10.1201/

b22251. URL https://www.taylorfrancis.com/books/mono/10.1201/b22251/semiconductor-radiation-detectors-alan-owens.

[22] Frank Hartmann. *Evolution of Silicon Sensor Technology in Particle Physics*. Springer, 01 2017. ISBN 978-3-319-64434-9. doi: 10.1007/978-3-319-64436-3. URL https://link.springer.com/book/10.1007/978-3-319-64436-3.

[23] M. Huhtinen. Simulation of non-ionising energy loss and defect formation in silicon. *Nuclear Instruments and Methods in Physics Research Section A: Accelerators, Spectrometers, Detectors and Associated Equipment*, 491(1):194–215, 2002. ISSN 0168-9002. doi: https://doi.org/10.1016/S0168-9002(02)01227-5. URL https://www.sciencedirect.com/science/article/pii/S0168900202012275.

[24] A. Vasilescu (INPE Bucharest) and G. Lindstroem (University of Hamburg). Displacement damage in silicon, on-line compilation. *journal*, August 2000. URL https://rd50.web.cern.ch/NIEL/default.html.

[25] M Moll. Radiation damage in silicon particle detectors. microscopic defects and macroscopic properties, Dec 1999.

[26] Michael Moll, Eckhart Fretwurst, M. Kuhnke, and G. Lindström. Relation between microscopic defects and macroscopic changes in silicon detector properties after hadron irradiation. *Nuclear Instruments & Methods in Physics Research Section B-beam Interactions With Materials and Atoms*, 186:100–110, 2002.

[27] Renate Wunstorf. *Systematische Untersuchungen zur Strahlenresistenz von Silizium-Detektoren für die Verwendung in Hochenergiephysik-Experimenten*. Dr., University of Hamburg, Hamburg, 1992. URL https://bib-pubdb1.desy.de/record/153817. Notional starting date. The scanned file is too big to be uploaded; University of Hamburg, Diss., 1992.

[28] Michael Moll. Displacement damage in silicon detectors for high energy physics. *IEEE Transactions on Nuclear Science*, PP:1–1, 04 2018. doi: 10.1109/TNS.2018.2819506.

[29] Olaf Krasel. *Charge collection in irradiated silicon detectors*. PhD thesis, Dortmund University, Aug 2004. URL https://cds.cern.ch/record/2630423. Presented on 2004-07-29.

[30] *Radiation effects in the cms phase-1 pixel detector*, volume 15 of *Workshop on Advanced Silicon Radiation Detectors*, Wien, Austria, 2020. Institute of High Energy Physics (HEPHY) of the Austrian Academy of Sciences (ÖAW). URL https://indico.cern.ch/event/813597/contributions/3727825/.

[31] J. Schwandt. Cms pixel detector development for the hl-lhc. *Nuclear Instruments and Methods in Physics Research Section A: Accelerators, Spectrometers, Detectors and Associated Equipment*, 924:59–63, 2019. ISSN 0168-9002. doi: https://doi.org/10.1016/j.nima.2018.08.121. URL https://www.sciencedirect.com/science/article/pii/S0168900218310805. 11th International Hiroshima Symposium on Development and Application of Semiconductor Tracking Detectors.

[32] Andrea Garcia Alonso Mohammadtaghi Hajheidari. Characterization of planar and 3d pixel sensors for the inner tracker of the cms experiment. In Mohammadtaghi Hajheidari, editor, *title*, volume 12, page 20. University of Birmingham, PSD12: The 12th International Conference on Position Sensitive Detectors, September 2021.

[33] *Characterization of planar and 3d silicon pixel sensors for the high luminosity upgrade of the cms experiment at lhc*, volume 16 of *Viena Conference of Instrumentation*, Wien, Austria, 2022. Vienna University of Technology. URL https://indico.cern.ch/event/1044975/contributions/4663658/.

[34] CERN. The lhc sees its first circulating beam. *journal*, Sept 2008. URL https://cerncourier.com/a/the-lhc-sees-its-first-circulating-beam/.

[35] CERN. The large hadron collider. *journal*, 2000. URL https://home.cern/science/accelerators/large-hadron-collider.

[36] CERN. CERN home. *journal*, 2000. URL https://home.cern/.

[37] Xavier Vidal and Ramon Manzano. High vacuum. *journal*, 2000. URL https://www.lhc-closer.es/taking_a_closer_look_at_lhc/0.high_vacuum.

[38] CERN. Cern accelerator complex. *journal*, 2000. URL https://home.cern/science/accelerators/accelerator-complex.

[39] Oliver Sim Brüning, Paul Collier, P Lebrun, Stephen Myers, Ranko Ostojic, John Poole, and Paul Proudlock. *LHC Design Report*. CERN Yellow Reports: Monographs. CERN, Geneva, 2004. doi: 10.5170/CERN-2004-003-V-1. URL https://cds.cern.ch/record/782076.

[40] Werner Herr and B Muratori. Concept of luminosity. *journal*, 2006. doi: 10.5170/CERN-2006-002.361. URL https://cds.cern.ch/record/941318.

[41] CERN. Higgs boson. *journal*, 2000. URL https://home.cern/science/physics/higgs-boson.

[42] CERN. CERN CMS. *journal*, 2000. URL https://home.cern/science/experiments/cms.

[43] CERN. CERN ALICE. *journal*, 2000. URL https://home.cern/science/experiments/alice.

[44] CERN. CERN LHCb. *journal*, 2000. URL https://home.cern/science/experiments/lhcb.

[45] Lucio Rossi and Oliver Brüning. *The High Luminosity Large Hadron Collider: the new machine for illuminating the mysteries of Universe*. Advanced series on directions in high energy physics. World Scientific, Hackensack, NJ, 2015. doi: 10.1142/9581. URL https://cds.cern.ch/record/1995532.

[46] Apollinari G., Béjar Alonso I., Brüning O., Fessia P., Lamont M., Rossi L., and Tavian L. *High-Luminosity Large Hadron Collider (HL-LHC): Technical Design Report V. 0.1*. CERN Yellow Reports: Monographs. CERN, Geneva, 2017. doi: 10.23731/CYRM-2017-004. URL https://cds.cern.ch/record/2284929.

[47] Corinne Pralavorio. LHC performance reaches new highs. *journal*, 2000. URL https://home.cern/news/news/accelerators/lhc-performance-reaches-new-highs.

[48] CERN. High-Luminosity LHC. *journal*, 2000. URL https://home.cern/resources/faqs/high-luminosity-lhc.

[49] CERN. About cms. *journal*, 2000. URL https://cms.cern/detector.

[50] The CMS Collaboration et al. The cms experiment at the cern lhc. *Journal of Instrumentation*, 3(08):S08004–S08004, aug 2008. doi: 10.1088/1748-0221/3/08/s08004. URL https://doi.org/10.1088/1748-0221/3/08/s08004.

[51] A Dominguez, D Abbaneo, K Arndt, N Bacchetta, A Ball, E Bartz, W Bertl, G M Bilei, G Bolla, H W K Cheung, M Chertok, S Costa, N Demaria, Daniel Dominguez Vazquez, K Ecklund, W Erdmann, K Gill, G Hall, K Harder, F Hartmann, R Horisberger, W Johns, H C Kaestli, K Klein, D Kotlinski, S Kwan, M Pesaresi, H Postema, T Rohe, C Schäfer, A Starodumov, S Streuli, A Tricomi, P Tropea, J Troska, F Vasey, and W Zeuner. CMS Technical Design Report for the Pixel Detector Upgrade. Technical report, CERN, Sep 2012. URL https://cds.cern.ch/record/1481838. Additional contacts: Jeffrey Spalding, Fermilab, Jeffrey.Spalding@cern.ch Didier Contardo, Universite Claude Bernard-Lyon I, didier.claude.contardo@cern.ch.

[52] Ernesto Migliore. The CMS Tracker Upgrade for the High-Luminosity LHC. Technical report, CERN, Geneva, Apr 2019. URL https://cds.cern.ch/record/2703520.

[53] Fluka. Fluka simulations. *journal*, Jan 2022. URL http://www.fluka.org/fluka.php.

[54] Kendall Russell Depriest. Historical examination of the astm standard e722 1-mev silicon equivalent fluence metric. *journal*, 12 2019. doi: 10.2172/1592863. URL https://www.osti.gov/biblio/1592863.

[55] G et al Bayatian. *CMS Physics: Technical Design Report Volume 1: Detector Performance and Software*. Technical design report. CMS. CERN, Geneva, 2006. URL https://cds.cern.ch/record/922757. There is an error on cover due to a technical problem for some items.

[56] Maurice Garcia-Sciveres. The RD53A Integrated Circuit. Technical report, CERN, Geneva, Oct 2017. URL https://cds.cern.ch/record/2287593.

[57] Aleksandra Dimitrievska and Andreas Stiller. RD53A: A large-scale prototype chip for the phase II upgrade in the serially powered HL-LHC pixel detectors. *Nucl. Instrum. Methods Phys. Res., A*, 958:162091. 4 p, 2020. doi: 10.1016/j.nima.2019.04.045. URL https://cds.cern.ch/record/2713276.

[58] I Dawson. *Radiation effects in the LHC experiments: Impact on detector performance and operation*. CERN Yellow Reports: Monographs. CERN, Geneva, 2021. doi: 10.23731/CYRM-2021-001. URL https://cds.cern.ch/record/2764325.

[59] M.Sze. *Physics and Properties of Semiconductors—A Review*, chapter 1, pages 5–75. John Wiley & Sons, Ltd, 2006. ISBN 9780470068328. doi: https://doi.org/10.1002/9780470068328.ch1. URL https://onlinelibrary.wiley.com/doi/abs/10.1002/9780470068328.ch1.

[60] M. Moll, E. Fretwurst, and G. Lindström. Leakage current of hadron irradiated silicon detectors – material dependence. *Nuclear Instruments and Methods in Physics Research Section A: Accelerators, Spectrometers, Detectors and Associated Equipment*, 426(1):87–93, 1999. ISSN 0168-9002. doi: https://doi.org/10.1016/S0168-9002(98)01475-2. URL https://www.sciencedirect.com/science/article/pii/S0168900298014752.

[61] A Chilingarov. Temperature dependence of the current generated in si bulk. *Journal of Instrumentation*, 8(10):P10003–P10003, oct 2013. doi: 10.1088/1748-0221/8/10/p10003. URL https://doi.org/10.1088/1748-0221/8/10/p10003.

[62] Form Factor. Summit12000. *journal*, Jan 2022. URL https://www.formfactor.com/.

[63] Keithly. 4200a-scs. *journal*, Jan 2022. URL https://www.tek.com/en/keithley-4200a-scs-parameter-analyzer.

[64] Keithly. 2657a. *journal*, Jan 2022. URL https://www.tek.com/en/products/keithley/source-measure-units/2650-series-high-power-sourcemeter.

[65] Mauricio Garcia-Sciveres. RD53A Integrated Circuit Specifications. Technical report, CERN, Geneva, Dec 2015. URL https://cds.cern.ch/record/2113263.